INFORMATION TO USERS

THE ELECTROCHEMICAL BEHAVIOR OF COPPER AND COPPER NICKEL ALLOYS IN SYNTHETIC SEA WATER

By

PAUL THOMAS WOJCIK

A DISSERTATION PRESENTED TO THE GRADUATE SCHOOL OF
THE UNIVERSITY OF FLORIDA IN PARTIAL FULFILLMENT OF THE
REQUIREMENTS FOR THE DEGREE OF DOCTOR OF PHILOSOPHY

UNIVERSITY OF FLORIDA

1997

UMI Number: 9802397

UMI

300 North Zeeb Road
Ann Arbor, MI 48103

ACKNOWLEDGMENTS

TABLE OF CONTENTS

APPENDICES

LIST OF TABLES

LIST OF FIGURES

LIST OF SYMBOLS

a	hydrodynamic constant, s^{-1}
A	electrode area, cm^2
c_i	concentration of species I, mol/cm^3
C	capacitance, μF
d	diameter, cm
D	diffusivity, cm^2/s
E	potential, V
E_B	electron's original binding energy, eV
f	frequency, Hz
F	Faraday's constant, 96,487 C/equiv
H	height, cm
i	current density, mA/cm^2
I	current, mA
K_{eq}	equilibrium constant
q	double layer charge, C/cm^2
R	resistance, Ω
R_p	polarization resistance, Ω
R	universal gas constant 8.314 J/mol/K
T	temperature, K
v	velocity, m/s
Z_r	real impedance, Ω
Z_j	imaginary impedance, Ω
α_a	apparent transfer coefficient, anodic
α_c	apparent transfer coefficient, cathodic

ρ	density, g/cm^3
μ	viscosity, cP
ν	kinematic viscosity, cm^2/s
ω	frequency, rad/s
Φ	potential, V
ϕ	stream function
η	dimensionless axial position
τ	shear stress, N/m^2
$h\nu$	X-ray energy

Abstract of Dissertation Presented to the Graduate School
of the University of Florida in Partial Fulfillment of the
Requirements for the Degree of Doctor of Philosophy

THE ELECTROCHEMICAL BEHAVIOR OF
COPPER AND COPPER NICKEL ALLOYS
IN SYNTHETIC SEA WATER

By

Paul Thomas Wojcik

August, 1997

Chairman: Mark E. Orazem
Major Department: Chemical Engineering

The goal of this work was to investigate the mechanism(s) of erosion-corrosion of

copper and copper alloys in high velocity synthetic sea water environments. An

impinging jet cell was designed to provide a platform where specific modes of enhanced

corrosion could be isolated. A novel galvanostatic impedance technique was developed to

collect impedance spectra without disrupting the temporal evolution of the system. A

measurement model technique was applied to the impedance spectra to predict the

polarization impedance and filter inconsistent data. The effect of velocity, pH, aeration,

and applied potentials on the corrosion behavior of copper and copper alloys was

investigated using electrochemical impedance spectroscopy, corrosion potential

monitoring, and analysis of digital image captures.

A video microscope was used to provide a visual record of the electrode surface

which could be used to determine shear-induced enhance corrosion. Results were

compared with reported values and mechanisms for enhanced corrosion of previously

reported work were proposed.

CHAPTER 1
INTRODUCTION

The object of this work was to investigate the phenomenon of enhanced corrosion of copper and copper nickel alloys in high-velocity sea water environments. This work was motivated by conflicting reports in the literature describing the mechanisms of enhanced corrosion in high velocity environments and the conditions necessary for enhanced corrosion to occur.

In 1977, K.D. Efird investigated copper and copper based alloys in high velocity sea water environments. Efird conducted experiments in a channel flow apparatus where samples were exposed to fresh sea water procured from the Atlantic Ocean off the coast of the Francis L. LaQue Corrosion Laboratory, Wrightsville Beach, North Carolina. The samples were exposed for thirty days at different velocities after which the samples were analyzed. Efird observed enhanced corrosion in the form of pits and waves on the coupon surface for velocities above a certain value. A shear stress corresponding with the empirically determined velocity was mathematically calculated and was referred to as the critical shear for the material tested. Efird concluded that copper (or copper alloys) subjected to shear values above the critical shear would exhibit enhanced corrosion. Efird also concluded that the mechanism responsible for the enhanced corrosion was the mechanical removal of a protective oxide film on the surface of the sample.

C.B. Diem (1990) conducted work on copper electrodes in aerated 0.62 M sodium chloride solutions with pH values of 8.5 and 9.5 to investigate the effect of shear stress on the anodic dissolution of copper. An axisymmetric impinging jet apparatus was utilized in conjunction with a scanning ellipsometer. The impinging jet configuration was chosen to ensure uniform mass transfer to the electrode surface and shear stress proportional to radial position. Experiments were conducted at velocities above values corresponding to the critical shear value for copper reported by Efird and no enhanced corrosion was observed. Diem concluded that erosion-corrosion of copper in alkaline chloride solutions is not caused by a shear-induced removal of protective films. Diem suggested non-uniform mass transfer and particle impingement as possible contributors to the enhanced corrosion observed by Efird. A direct comparison between the work of Diem and Efird was not possible due to differences in the aqueous environments studied. The work conducted by Diem involved short term experiments on the order of hours, whereas, Efird's experiments were conducted over a period of thirty days.

For this work an impinging jet cell was designed and built with several improvements to better investigate the free corrosion of copper and copper nickel alloys in high-velocity synthetic sea water environments. The goals of this work were to

- determine the mechanism for enhanced corrosion of copper and copper nickel alloys in high velocity environments

- determine if hydrodynamic shear can remove protective films.

The importance of this work lies in the fact that copper is a popular material for use in marine environments. Key features contributing to the widespread use of copper are

desirable material characteristics and cost effectiveness. The approach to this problem involved design of an experimental system to investigate specific causes of enhanced corrosion in high velocity environments. Electrochemical techniques were applied to monitor the reactivity and state of the electrode surface (Syrett & Macdonald 1979). Corrosion potential measurements and impedance spectroscopy were used to monitor electrochemical properties of the electrode surface, and video microscopy was used to observe the surface and to record events as a function of time.

Copper and copper alloys are well suited for marine applications. Copper has a high thermodynamic stability and forms a protective oxide film, which can decrease or eliminate corrosion. The world's oceans are teaming with living organisms which can adhere to exposed surfaces and alter the chemical reactions occurring on the surface, in turn, affecting the rate of corrosion. Copper is toxic to many organisms and, this, reduces the risk of microbiologically influenced corrosion (Gilbert 1982).

Unexpectedly high corrosion rates have been reported in high velocity environments which are common in marine heat exchangers and in regions of turbulence around the periphery of marine screws (LaQue 1975, Efird 1977). There are many methods available for inhibiting corrosion in copper systems although in the vicinity of marine screws or heat exchangers, these methods may not be effective or practical (Goodman 1987). Increased mass transfer of corrosive species to the surface and corrosion products away from the surface (Diem & Orazem 1994), shear induced removal of a protective film, cavitation causing disruption of the film and surface damage (Wood et al. 1990a), as well as impingement of particles onto the surface resulting in protective film removal, have all been suggested as possible causes of the increased corrosion rate

(Copson 1960, Dawson et al. 1990, Heitz 1991, Sethi & Wright 1991, Somerscales & Sanatgar 1991). In many cases the effects of erosion of the film and corrosion act synergistically, i.e., the total effect is greater than the sum of the individual effects.

A novel approach to conducting galvanostatically controlled impedance experiments was developed during this work (Wojcik et al. 1996, Wojcik & Orazem 1997a, Wojcik & Orazem 1997c). The utility of this modified galvanostatic technique was to non-invasively investigate actively corroding systems where the baseline corrosion potential changes with time. The development of the variable amplitude galvanostatic (VAG) technique addressed problems inherent with both potentiostatic and conventional galvanostatic regulation. The VAG technique utilizes previously acquired impedance data to predict the impedance value for the next frequency. The predicted impedance value is used to determine an optimum value for the current perturbation and current measuring resistor for the next measurement. This predictive technique ensures acceptable signal to noise ratio as well as a linear signal response.

Background information including electrochemical processes, thermodynamics of copper, film formation and enhanced corrosion in high velocity environments are discussed in Chapter 2. The theory behind electrochemical impedance spectroscopy, different methods of conducting impedance experiments, and examples of applications are presented in Chapter 3. The cell design and instrumentation used to conduct experiments and collect data is described in Chapter 4. The reason the impinging jet configuration was chosen over other cell designs is also explained in this chapter. A description of the procedures used to conduct experiments is given in Chapter 4 as well as the preparation techniques used for samples and solutions. The technique described in Chapter 5

incorporates the positive aspects of both potentiostatic and conventional galvanostatic regulation. Comparisons are made between the variable amplitude galvanostatic technique and other commonly applied techniques for a variety of test systems.

Discussion and results are the topics of Chapter 6 where a brief explanation of the measurement model technique is given. Corrosion potential analysis, impedance spectra analysis, x-ray photoelectron spectroscopy, scanning electron microscopy, linear sweep voltammetry and image analysis are covered in this chapter. Comparisons of the results obtained in this work and results previously reported are presented in Chapter 7. Conclusions drawn from this work are discussed in Chapter 8 and recommendations for future work are discussed in Chapter 9.

CHAPTER 2
BACKGROUND

The utility of copper for use in sea water environments and the limitations of models are discussed in Chapter 2. Issues of the thermodynamics of copper are presented, and the corrosion of copper in alkaline chloride solutions, sea water, and environments with flow is discussed in this chapter.

2.1 Copper Utility in Sea Water Environments

Copper and copper alloys have a long history of use in marine applications and other corrosive environments. Recent developments of high performance materials which equal or exceed the desired characteristics of copper have not reduced the wide use of copper and copper alloys in industrial applications. The longevity of copper and copper alloys can be attributed to economics and a combination of desirable material characteristics.

Copper is relatively inexpensive when compared to materials with comparable corrosion resistant properties e.g. titanium. Copper is found in a natural state and is also present in a number of ores including cuprite, malachite, azurite, chalcopyrite, and bornite. Copper ores are currently the primary source for refined copper. Copper is extracted from the ore by means of smelting, leaching, and electrolysis. The thermal conductivity of pure

copper at 473 K is 389 W/m•K compared to iron, 304 stainless steal, pure nickel, and titanium with values of 66, 18, 74, and 20 W/m•K respectively (White 1984). Copper is second only to silver in electrical conductivity (Weast 1984). The machinability of copper and copper alloys combined with other physical properties make these metals excellent materials for a wide variety of applications including use in heat exchangers and other complicated parts.

2.2 Model Limitations

Discrepancies can exist between results predicted by an equilibrium model and empirically determined real system parameters. The goal of modeling is to closely approximate the real system of interest. There are several reasons for discrepancies between model approximations and real system. Models usually require approximations and/or dismissal of certain parameters that are not well understood or are believed to be negligible. This can lead to errors in the model's predictive capabilities. One hopes to be able to describe a real system in terms of a first approximation with an equilibrium model. A brief description of sources of errors in equilibrium models is given as follows.

2.2.1 Limitations of thermodynamic information

The lack of consideration of important species in solution or solid phases is an example of a source of error. The Pourbaix diagrams, while valuable, may not consider all possible species. The thermodynamic data for the species considered may be incorrect or

inadequate. Temperature and pressure corrections may not be accurate and can vary dramatically in natural sea waters.

2.2.2 Real system chemical characterization inadequacies

Analytical data for species may not be adequate to determine the physical or chemical forms (i.e. oxidized/reduced, suspended/dissolved) of chemical elements in complex real systems where interactions with other species are present.

2.2.3 Under-predicted reaction rates

An equilibrium state in a real system may be achieved slowly due to rates of some chemical reactions.

2.2.4 Chemical reaction times

For irreversible reactions, no equilibrium state is reached and the reaction proceeds until the species which is stoichiometrically limited is exhausted. Irreversible reactions that are slow in sea water environments can include metal-ion oxidation, oxidation of sulfides, aging of hydroxides and oxide precipitants, and precipitation of metal-ion carbonates.

2.3 Thermodynamics

In neutral solutions free of oxidizing agents, copper is thermodynamically stable at open circuit. Copper can passivate in thoroughly de-aerated solutions which virtually eliminate corrosion. In oxygen-free systems, there is no oxide film formation. Reactions which lead to corrosion and mass loss of copper in sea water are given as

$$Cu \leftrightarrow Cu^- + e^- \qquad (1)$$

$$Cu \leftrightarrow Cu^{--} + 2e^- \tag{2}$$

$$Cu^- \leftrightarrow Cu^{--} + e^- \tag{3}$$
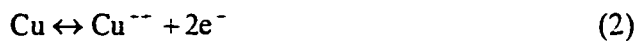
The corresponding standard electrode potentials for these reactions can be found in Table 2.1 (Bard & Faulkner 1980).

Table 2.1: Selected standard electrode potentials in aqueous solutions at 25°C referenced to a normal hydrogen electrode (Bard & Faulkner 1980).

Reaction	Potential, V
$Pt^{2-} + 2e = Pt$	≈ 1.2
$Cu^- + e = Cu$	0.522
$Cu^{2-} + e = Cu^-$	0.158
$Cu^{2-} + 2e = Cu$	0.3402
$Cu^{2-} + 2e = Cu(Hg)$	0.345
$Na^- + e = Na$	-2.7109
$Ni^{2-} + 2e = Ni$	-0.23
$Ni(OH)_2 + 2e = Ni +$	-0.66
$Mn^{2-} + 2e = Mn$	-1.029
$Mg^{2-} + 2e = Mg$	-2.375

In a particular system, these reactions can manifest themselves in a number of different forms. The ions can oxidize, diffuse into solution to later complex with other ions, or react with a non-metallic ion to form a salt. Both oxides and salts can form films on the surface of the electrode which in many cases can decrease the rate of corrosion. Oxide layers tend to be more stable than salt films.

A strong dependence exists between film stability, pH, and applied potential in systems with copper corrosion present. Potential-pH equilibrium diagrams, or Pourbaix diagrams, for copper in a variety of different media are available in the literature. Pourbaix diagrams are constructed utilizing the Nernst equation and take into consideration the solid phases likely to be present. Pourbaix diagrams give a reference point to assist in the determination of possible reactions and possible film compositions on the surface of the electrode. The diagrams are utilized only as a guide, because of the condition of equilibrium under which the plots were constructed. Factors which can effect the final state of a system include mass transport phenomena, kinetics of dissolution, pH profile versus time, and electrode history. Electrode history can involve treatment of the electrode before immersion (e.g. annealing, mechanical processing) which can affect metal grain size, structure, orientation and boundaries as well as surface roughness. Electrode history can also include electrode preparation after immersion, typically an applied potential. Copper corroding at open circuit can be greatly affected by electrode history because the corrosion mechanism involves the formation of local anodes and cathodes.

Pourbaix diagrams for a copper-water system are displayed in Figures 2.1 and 2.2 (Pourbaix 1974) and a copper-sea water system in Figures 2.3 through 2.6 water (Bianchi & Longhi 1973). Other environments for which potential-pH diagrams have been constructed include chlorinated water of different concentrations and solutions in which bicarbonate ions were present. To give an indication of what films may be present in a copper-sea water system, Bianchi and Longhi (1973) constructed potential-pH equilibrium diagrams which are presented in Figures 2.3 through 2.6. Efird (1975) constructed potential-pH equilibrium diagrams for 70-30 and 90-10 copper-nickel alloys in sea water.

Stability domains of metal species in sea water relative to pH and potential allow for the prediction of reactions that may take place in a system. One can see from the diagrams that there is a large region of passivity at moderately alkaline pH values in which CuO and Cu$_2$O layers protect the surface.

The local pH can be substantially different from that of the bulk which can affect what films form on the surface of the electrode. The total reaction for corrosion of copper in alkaline chloride solutions indicates an alkalization at the electrode interface

$$2Cu + \frac{1}{2}O_2 + H_2O + xCl^- \rightarrow 2CuCl_x^{(x-1)-} + 2OH^- \ . \tag{4}$$
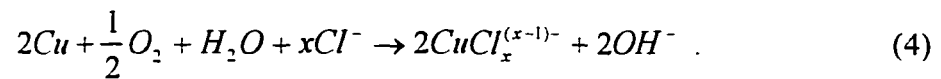
Fiori et al. (1977) calculated that the local pH at the electrode surface was 8.9 where as the bulk pH of the 0.5M NaCl solution was 8.3. Chang and Prentice (1986) and Moghissi (1993) developed models to calculate the concentration distribution of reactive species in a porous film on an electrode surface, and the concentration of species can be utilized to determine pH near the electrode surface. Deslouis et al. (paper in progress) developed a pH sensor grid assembly in conjunction with an impinging jet cell to determine local pH empirically. Their results showed good agreement with published theoretical results.
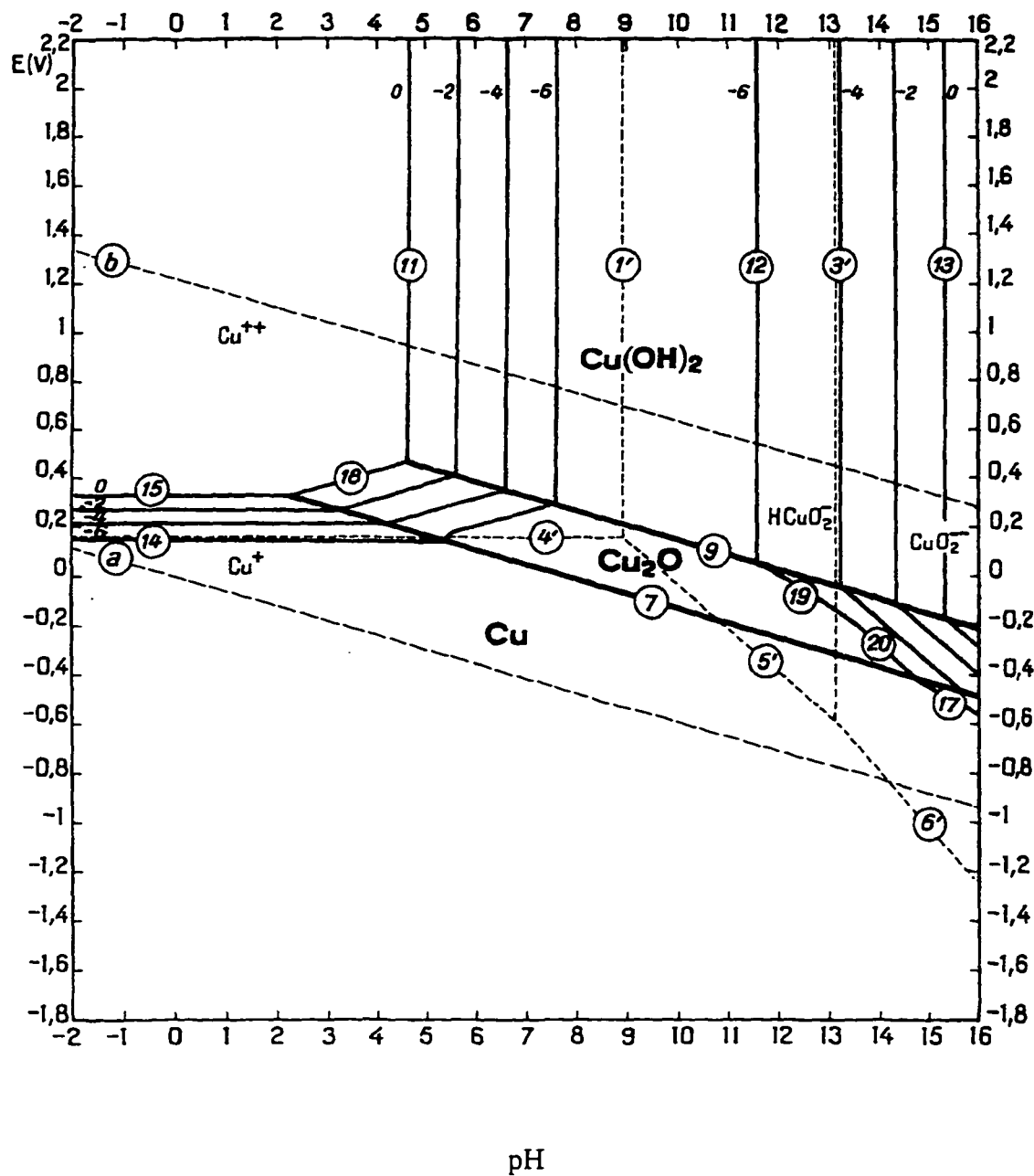
Figure 2.1: Potential-pH equilibrium diagram for a copper / water system at 25°C. Solid substances under consideration are Cu, Cu₂O, and CuO. The numbers in this figure correspond to reactions given in the *Atlas of Electrochemical Equilibria in Aqueous Solutions*. A more detailed description of this figure is given in the reference (Pourbaix 1974).
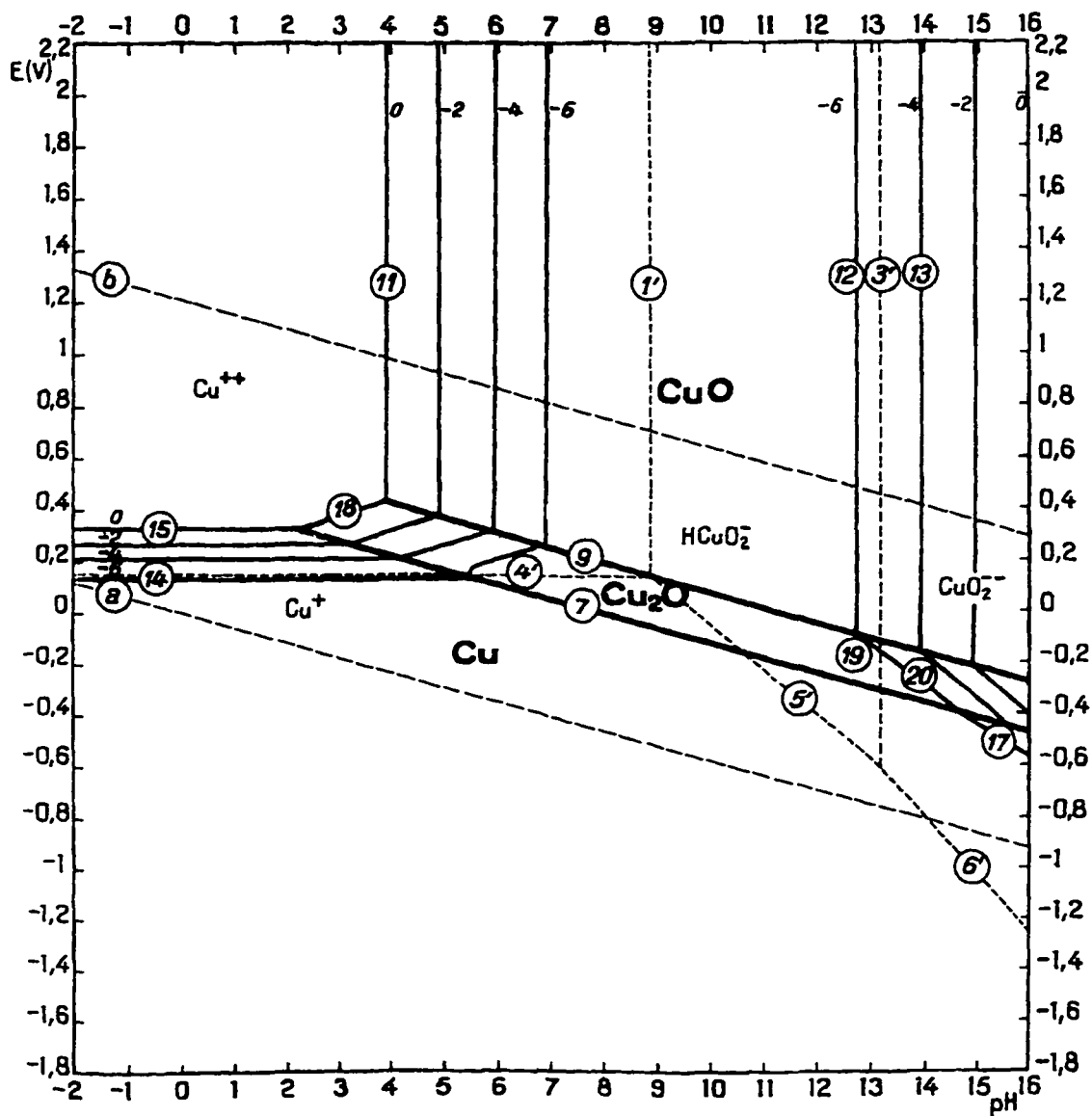
Figure 2.2: Potential-pH equilibrium diagram for a copper / water system at 25°C. Solid substances under consideration are Cu, Cu₂O, and Cu(OH)₂ (Pourbaix 1974). The numbers in this figure correspond to reactions given in the *Atlas of Electrochemical Equilibria in Aqueous Solutions*. A more detailed description of this figure is given in the reference (Pourbaix 1974).
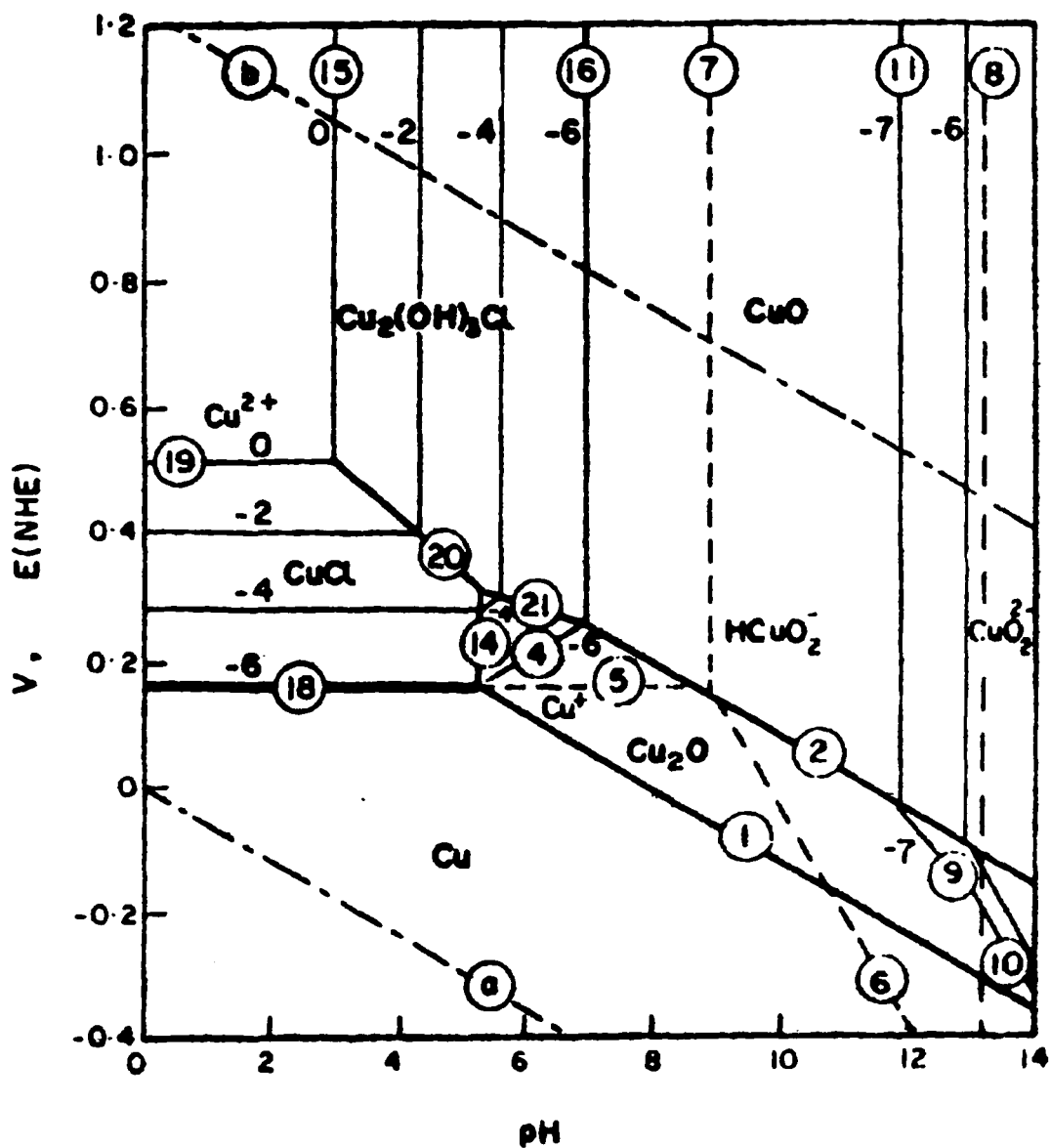
Figure 2.3: Potential-pH equilibrium diagram for a copper / sea water system at 25°C. Solid substances under consideration are Cu, Cu₂O, CuCl, CuO, and Cu₂(OH)₃Cl. The numbers in this figure correspond to reactions given in the reference which gives a detailed description of this figure (Bianchi & Longhi 1973).
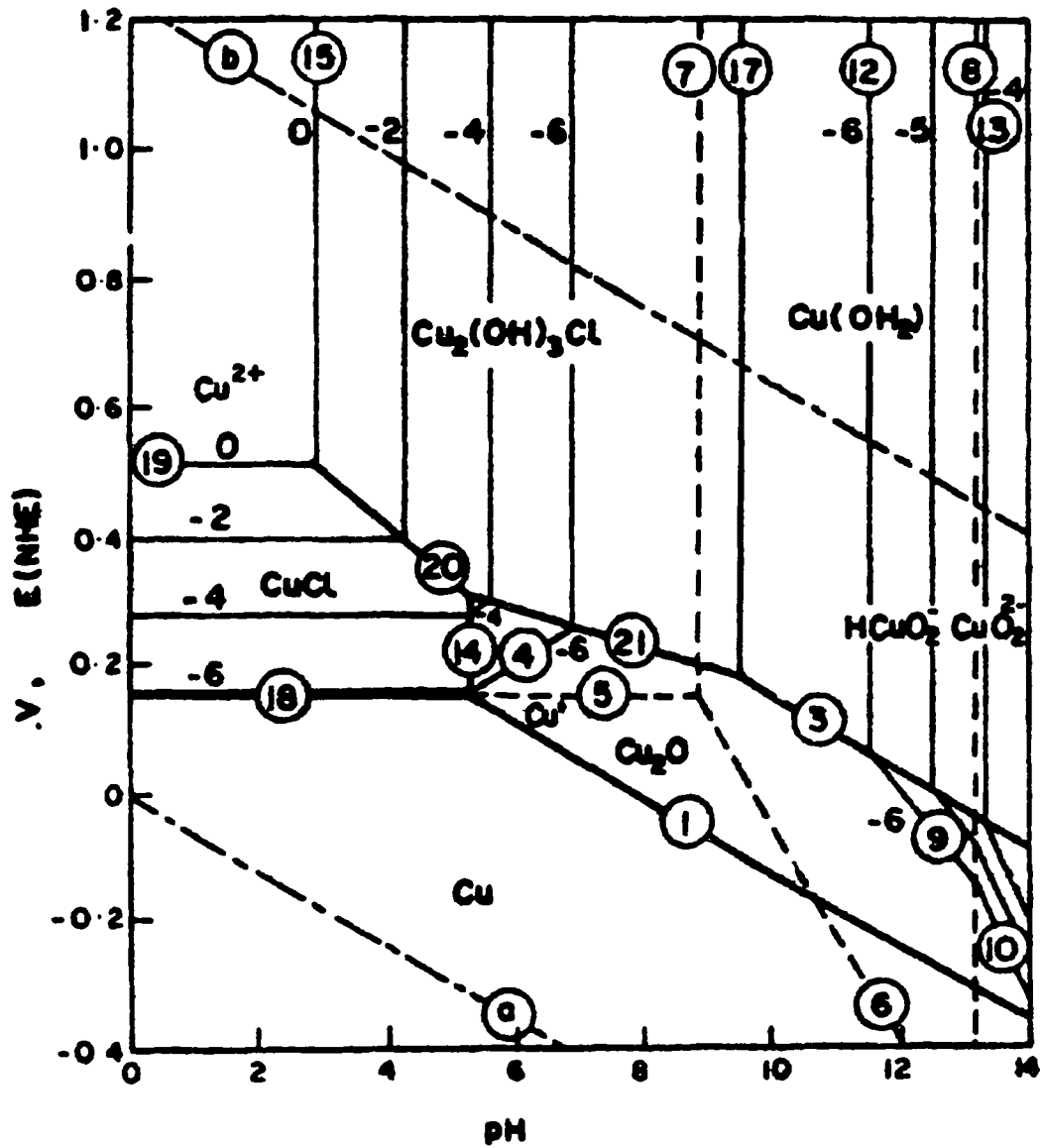
Figure 2.4: Potential-pH equilibrium diagram for a copper / sea water system at 25°C.
Solid substances under consideration are Cu, Cu_2O, CuCl, $Cu(OH)_2$, and
$Cu_2(OH)_3Cl$. The numbers in this figure correspond to reactions given in the
reference which gives a detailed description of this figure (Bianchi & Longhi
1973).
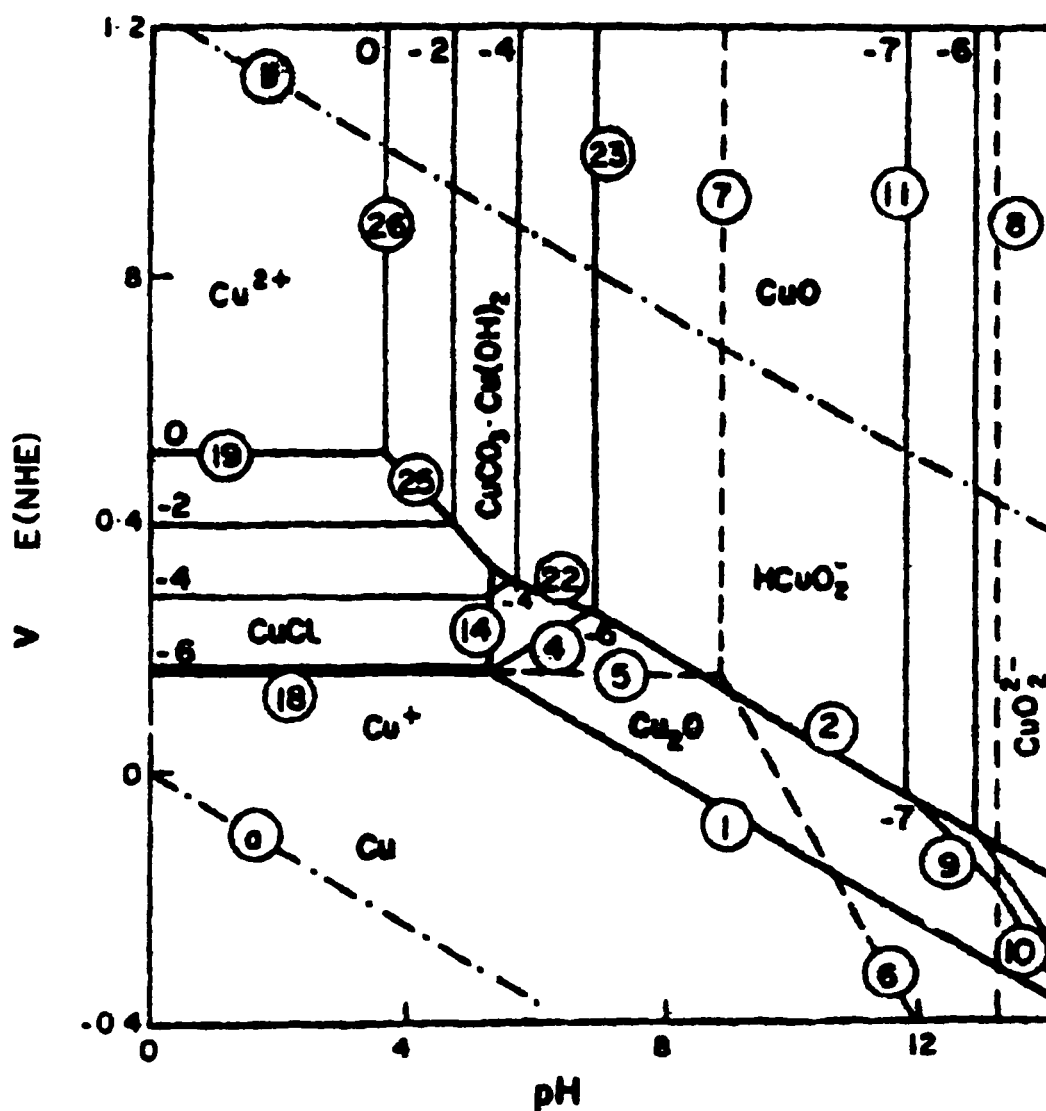
Figure 2.5: Potential-pH equilibrium diagram for a copper / sea water system at 25°C. Solid substances under consideration are Cu, Cu₂O, CuO, CuCl, and CuCO₃•Cu(OH)₂. The numbers in this figure correspond to reactions given in the reference which gives a detailed description of this figure (Bianchi & Longhi 1973).
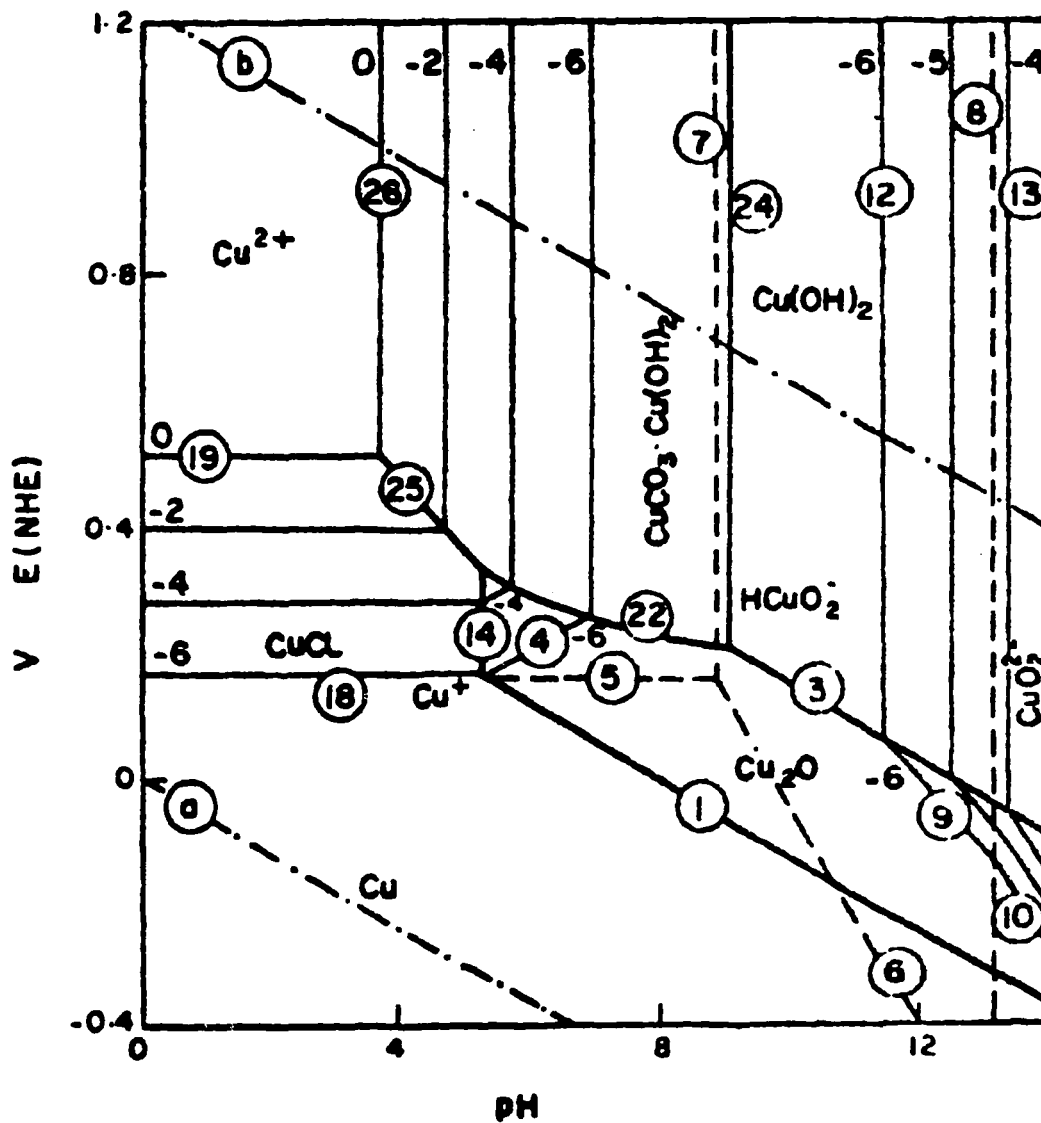
Figure 2.6: Potential-pH equilibrium diagram for a copper / sea water system at 25°C. Solid substances under consideration are Cu, Cu_2O, CuCl, $Cu(OH)_2$, and $CuCO_3 \bullet Cu(OH)_2$. The numbers in this figure correspond to reactions given in the reference which gives a detailed description of this figure (Bianchi & Longhi 1973).

2.4 Corrosion in Alkaline Chloride Solutions

The presence of chloride ions in solution greatly affects the corrosion behavior of copper. Ives and Rawson (1962) reported that chloride concentrations as low as 50 ppm caused accelerated dissolution of a cuprous oxide film. However, the presence of chloride ions can also stimulate the formation of chloride film which protects the electrode surface.

The majority of fundamental studies of copper in chloride solution published in the literature were conducted in acidic environments. The processes involved in the corrosion of copper in alkaline environments are more complex than those in acid environments but the driving force of end use applications promotes study in this area. Studies have been conducted on the electrochemical behavior of metals such as copper and copper-based alloys in neutral, alkaline, and sea water solutions (Deslouis et al. 1988a, Deslouis et al. 1988b, Lal & Thirsk 1953, Dhar et al. 1985, Hack & Scully 1986). Literature reviews concerning corrosion in sea water have been compiled by Gilbert and LaQue (1954), Tuthill (1987), and Gehring (1987) and a review of studies to determine erosion-corrosion on copper alloys in sea water was written by Syrett (1976).

For a freely corroding metal, both a cathodic reduction reaction and an anodic dissolution reaction are present. When the corrosion potential reaches a constant value, the rates of the anodic and cathodic reactions are considered to be equal. Table 2.2 lists the cathodic reactions for copper in an alkaline aqueous system (Moghissi 1993). In a well-aerated chloride solution, the usual dissolution reaction for copper is given as

Table 2.2: Cathodic reactions for copper in an alkaline aqueous solution.

Cathodic Reaction	E°, V
$2H_2O + 2e^- \leftrightarrow H_2 + 2OH^-$	-0.828
$O_2 + 2H_2O + 4e^- \leftrightarrow 4OH^-$	0.401
$O_2 + 2H_2O + 2e^- \leftrightarrow H_2O_2 + 2OH^-$	-0.146
$H_2O_2 + 2e^- \leftrightarrow OH^-$	0.948

$$Cu + 2Cl^- \leftrightarrow CuCl_2^- + e^- \tag{5}$$
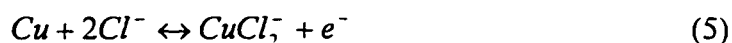
which was modeled by Bacarella and Griess (1973). This reaction was broken down into two parts by Lee and Nobe (1986) and (Barcia et al. 1993).

$$Cu + Cl^- \leftrightarrow CuCl + e^- \tag{6}$$

$$CuCl + Cl^- \leftrightarrow CuCl^- \tag{7}$$

Faita et al. (1975) described the reaction mechanism to be

$$Cu + 2Cl^- \leftrightarrow CuCl_2^- + e^- \tag{8}$$

$$Cu + 3Cl- \leftrightarrow CuCl_3^{2-} \tag{9}$$
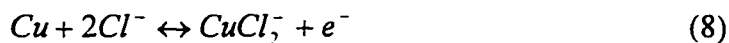
and concluded that $CuCl^{2-}_3$ was the prominent soluble dissolution product in 0.5M NaCl solution. These findings were based on calculations based on activity coefficients and solubility constants of species present. The corrosion of copper directly to Cu_2O is also possible by the reaction

$$2Cu + OH^- \leftrightarrow Cu_2O + H^+ \tag{10}$$

or

$$2Cu + H_2O \leftrightarrow Cu_2O + 2H^+ + 2e^- \tag{11}$$
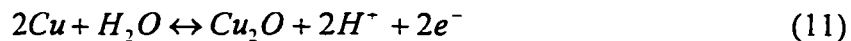
as described by Efird (1975) who confirmed the presence of the corrosion product through X-ray analysis. At more anodic potentials CuO will form by

$$Cu_2O + 2OH^- \leftrightarrow 2CuO + H_2O + 2e^- \tag{12}$$
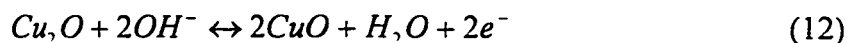
Either Cu_2O or CuO can protect the surface of the electrode but both are sensitive to pH and potential. Another commonly found film, $CuCl_2$, is present at more anodic potentials and also provides corrosion protection.

2.5 Copper in Sea Water Environments

Presence of the additional species found in sea water provides mechanisms for a wide variety of other reactions. Other factors that can effect the corrosion resistance of copper in sea water are the presence of suspended particles and the presence of living organisms. An investigation of the structure and properties of calcareous deposits on metal surfaces and the influential variables in deposit formation was conducted by Hartt et al. (1984). Mansfield and Little (1992) investigated microbiologically influenced corrosion of copper-based materials in natural sea water comparing their results to that of synthetic sea water. Sulfate reduction and metal-ion oxidation reactions can be greatly accelerated by microbiological catalysts. A study on the effect of chlorination on the corrosion of materials in sea water cooling systems was conducted by Goodman (1987). This work included steps to minimize both the presence of suspended particles and the level of microbiological activity.

The American Society for Testing and Materials (ASTM) standard for sea water, which is an accepted standard for the formulation of synthetic sea water, is presented in Table 2.3. The ASTM D-1141-52A provides the composition for sea water in terms of weight percentages of each species present for the purpose of corrosion studies, chemical processing, ocean instrument testing, and biological studies. The presence of these additional species in natural sea water provides a path for a vast number of reactions, complexes, and films which affect the rate of corrosion (Dar et al. 1985).

Table 2.3: Elemental composition of ASTM D-1141-52 formula A synthetic sea water.

Material	Weight Percent
NaCl	58.490
$MgCl_26H_2O$	26.460
Na_2SO_4	9.750
$CaCl_2$	2.765
KCl	1.645
$NaHCO_3$	0.477
KBr	0.238
H_3BO_3	0.071
$SrCl_2 \bullet 6H_2O$	0.095
NaF	0.007

Table 2.4: Copper compounds possible in a copper/synthetic sea water system. The color and solubility in water are given for each compound (Weast 1984).

Name	Compound	Color	Solubility g /100cc water
copper	Cu (element)	reddish	insoluble
cuprous chloride	CuCl	white	0.0062
cupric chloride	$CuCl_2$	brown-yellow	70.6
cuprous chloride dihydrate	$CuCl_2 \bullet 2(H_2O)$	blue-green	110.4
cupric chloride, basic	$CuCl_2 \bullet Cu(OH)_2$	yellow-green	decomposes
cupric hydroxide	$Cu(OH)_2$	blue	insoluble
cuprous oxide	Cu_2O	red	insoluble
cupric oxide	CuO	black	insoluble
copper oxide, per-	$CuO_2 \bullet H_2O$	brown brown-black	insoluble
copper oxide, sub-	Cu_4O	olive green	insoluble
cupric oxychloride	$Cu_2(OH)_3Cl$	green	n.a.
calcium carbonate, aragonite	$CaCO_3$	colorless	0.00153
calcium carbonate, calcite	$CaCO_3$	colorless	0.0014
calcium hydroxide	$Ca(OH)_2$	colorless	0.185
calcium sulfate	$CaSO_4$	colorless	n.a.
magnesium sulfate	$MgSO_4$	colorless	26.0

Table 2.5: Heterogeneous equilibria involving oxides, hydroxides, carbonates, and hydroxide carbonates (Stumm & Morgan 1981).

Reaction	Log K^a
$CuO(s) + 2H^+ = Cu^{2+} + H_2O$	7.65
$Cu_2(OH)_2CO_3(s) + 4H^+ = 2Cu^{2+} + 3H_2O + CO_2(g)$	14.16
$Cu_3(OH)_2(CO_3)_2(s) + 6H^- = 3Cu^2 + 4H_2O + 2CO_2(g)$	21.24
$Cu_2 + +H_2O = CuOH^+ + H^-$	-8.0
$2Cu^{2+} + 2H_2O = Cu_2(OH)_2^{2+} + 2H^+$	-10.95
$Cu^{2+} + CO_3^{2-} = CuCO_3(aq)$	6.77
$Cu^{2+} + 2CO_3^{2-} = Cu(CO_3)_2^{2-}(aq)$	10.01
$CO_2(g) + H_2O = HCO_3^- + H^+$	-7.82
$Cu^{2+} + 3H_2O = Cu(OH)_3^- + 3H^+$	-26.3
$Cu^{2+} + 4H_2O = Cu(OH)_4^{2-} + 4H^-$	-39.4

Table 2.4 lists compounds which can be present in a copper/sea water system with the associated color and equilibrium constant. The color of the compound can assist in the identification of films present on the surface of the electrode. It should be noted that film color is affected by film thickness. Table 2.5 presents heterogeneous equilibrium reactions involving copper and sea water and the resulting oxides, hydroxides, carbonates, and hydroxide carbonates.

The dissolution of copper can occur at high rates at locally active anode sites. It has already been stated that these sites exist on a copper electrode at the corrosion potential. The metal salts that form can precipitate and adhere to the surface of the electrode forming a protective film. This film, however, is very susceptible to fluid motion and potential. Salt films can be removed at much lower velocities than are oxide films, and flow induced removal of oxide films could initiate of enhanced corrosion.

2.6 Electrochemical Behavior of Copper in Aqueous Environments with Flow

Copper and copper alloys are widely used in marine environments because they are resistant to corrosion in sea water. This resistance is associated with formation of protective layers on the metal surface. However, copper and its alloys are known to be susceptible to enhanced corrosion in sea water when there is sufficient relative motion between the metal and the fluid (LaQue 1975, Efird 1977, Wood & Fry 1990). In naval ships, copper alloys are used in heat exchanger tubes, and, in these applications, the metal is also subjected to high flow conditions where erosion-corrosion may be a problem. It is possible to overestimate the corrosion resistance of a metal if the testing is done under static conditions when service is under non-static conditions.

2.6.1 Erosion corrosion

Under conditions of flow the naturally formed protective films on the copper surface, can be prevented from forming, can be removed, or can be modified. Formation of passive films has been found to be more difficult with increasing Reynolds number (Ives & Rawson 1962, Fiori et al. 1977). The removal of a protective film can be referred

to as erosion-corrosion which is defined as the attack on a metal surface resulting from the combined effects of erosion and corrosion (Parker 1994) or accelerated corrosion resulting from removal of protective films by shear stress, cavitation, or impingement (LaQue 1975, Perry 1963).

2.6.2 Causes and indications

There are several possible mechanisms for velocity-enhanced corrosion of metals in flowing solutions (Wood et al. 1990, Copson 1960, Dawson et al. 1990, Heitz 1991, Sethi & Wright 1991, Somerscales & Sanatgar 1991, Diem & Orazem 1994).

1. Corrosion enhancement by increased convective mass transfer is commonly observed and can be predicted through semi-empirical correlations for Sherwood number as a function of Reynolds and Schmidt number (Bird et al. 1960). Mass transfer can influence reactants or products of corrosion (Alkire 1985, Gan & Orazem 1986, Gilbert 1982). While film formation sufficient to reduce corrosion rates can be evident on the order of days, some work suggests that steady-state films on copper alloys may require 30 days or more to develop (Hack & Gudas 1979, Hack & Pickering 1991, Hack & Scully 1986, Scully et al. 1986).

2. Localized corrosion can be driven by formation of differential mass transfer cells. In aerated corrosion systems, differential oxygenation cells can be seen when mass transfer is not uniform and galvanic coupling causes high rates of local corrosion. Even in a simple geometry, such as a rotating disk, this can occur if laminar and turbulent flow regimes exist together on the metal surface (LaQue 1957, Vahdat &

Newman 1973, Law & Newman 1986). It is possible for the pitting potential to be reached locally, causing enhanced corrosion.

3. Erosion-corrosion can be caused by disruption or removal of protective layers by particle impingement (Heitz 1991, Sethi & Wright 1991). It has been found that the two phenomena act synergistically, *i.e.*, the total effect is greater than the sum of the individual effects. Microorganisms, sand, and debris can be present in natural sea water and can damage protective films if the particles impinge on the surface with sufficient energy.

4. Enhanced corrosion can be caused by disruption or removal of protective layers by cavitation. Cavitation occurs when the local pressure of the fluid is less than the vapor pressure of the fluid. Alkire and Perusich found that ultrasonically produced cavitation prevented the passivation of stainless steel (Alkire 1983). It is well known that cavitation can be a problem in pump impellers, in marine screws (propellers), and in high velocity flow systems (Wood & Fry 1990).

5. Erosion-corrosion is often considered to be associated with disruption or removal of protective layers by hydrodynamic shear (Efird 1977, Silverman 1984). In this mechanism, the protective layers are removed when the shear force is greater than the binding force between the film and the substrate. While the removal of protective layers by hydrodynamic shear has been proposed by Efird (1977) to be the cause of erosion-corrosion of copper in sea water, Copson (1960) suggested that the adhesion forces for oxide films are too large to be overcome by hydrodynamic forces. Efird (1977) has reported critical values of shear stress for the erosion-corrosion of copper and some copper-based alloys in sea water. The system used in previous work (Diem

& Orazem 1994) was designed to exceed the values of critical shear stress reported by Efird (1977) by more than 10-fold. No shear-induced corrosion on unaged copper was reported. Direct observation of shear-induced removal of films has been reported for some systems. Giralt and Trass (1975) showed that removal of solid naphthalene and trans-cinnamic acid by a submerged impinging jet of saturated solution is proportional to the wall shear stress above a critical or threshold value. Steele and Geankoplis (1959) reported removal of material by an apparent shear erosion mechanism. Esteban et al. (1990) used an impinging jet system to identify shear-induced removal of poorly adhered film-forming inhibitors on steel in chloride solutions.

In complicated geometries several mechanisms can be present simultaneously, which makes it difficult to determine the relative importance of each effect. It is necessary to know the mechanism of attack in order to control corrosion. In this work, the corrosion of copper and copper alloys was studied in a system for which the possible mechanisms for erosion-corrosion could be isolated.

CHAPTER 3
ELECTROCHEMICAL TECHNIQUES

The use of impedance spectroscopy to investigate and characterize systems of interest is gaining popularity largely due to the large amount of information that can be extracted from this non-invasive technique. Impedance spectroscopy is being utilized to investigate corrosion behavior, battery performance and life expectancy, coating and inhibitor effectiveness, and semiconductor characterization (Wojcik 1992). Systems which are difficult to analyze using other techniques, for example, low conductivity media and high impedance surfaces, are also being addressed. Impedance techniques have the advantage of high accuracy, non-invasiveness, as well as the ability to measure in-situ with relatively short measurement times. This chapter will discuss electrochemical techniques along with advantages and disadvantages of each.

Electrochemical systems, such as the systems described in Chapter 2, can be investigated by electrochemical impedance spectroscopy (EIS). In an electrochemical system, a series of events take place leading to a charge transfer at the surface of the electrode as described in Chapter 2. Transport of reactive species from the bulk solution to the surface of the electrode is governed by the diffusivity of the species and the hydrodynamic characteristics of the system. Adsorption of the reactive species onto the electrode surface takes place on the electrode resulting in electrochemical reactions and

the flow of a Faradaic current. The subsequent dissolution rate of the reaction product back to the bulk solution also plays an important role on the system characteristics.

3.1 Large Signal Amplitude Measurement Techniques

There are a vast variety of electrochemical techniques that can be utilized to study systems of interest. Sweep, sine wave, step, and pulse techniques of both current and potential are popular. With these techniques one parameter is controlled, usually current or potential, and the other variable is monitored. These types of techniques, with the exception of sine wave, are typically large amplitude signal analysis procedures due to the large range of potential or current that is used to perturb the system. The advantages of these techniques are the ease of conducting the experiment, the short time required to complete an experiment, and the straightforward methods of analysis. Disadvantages include a limited amount of information available from the data and the high probability of irreversible changes on the system due to the measurement itself. Because of the disruptive nature of these procedures, in-line testing for quality control or process monitoring is not appropriate.

3.2 Small Signal Amplitude Measurement Techniques

Small-amplitude signal analysis is utilized when a linear signal response is desired. Linear relaxation techniques such as EIS are based on the principle that the perturbing signal is of an amplitude sufficiently small as to allow for the linearization of the process about a dc polarization point.

3.3 Electrochemical Impedance Spectroscopy

Electrochemical impedance techniques are utilized in this work to investigate and evaluate the electrical behavior of electrodes in order to determine material performance. The fundamental approach of all EIS techniques is to apply a small amplitude sinusoidal perturbation, typically current or potential, and measure the system's response. The two most common methods for applying the excitation signal are the single-sine and multi-sine techniques. The multi-sine technique involves applying a pseudo-random white noise signal to the system. The waveform consists of superimposed sine waves of different frequencies, and the response is analyzed using a fast Fourier transform algorithm to calculate the impedance at each of the discrete frequencies. The advantage of this method is speed. Single measurements of this type can be taken rapidly, however, due to the inherent noise encountered in the signal measurement, several measurements may have to be taken to reduce the effect of noise to an acceptable level (Gabrielli 1985). The need for repeated measurements can completely eliminate the advantage of speed. Therefore this technique is typically reserved for investigating systems that are rapidly changing and where the demand for high data quality is not a priority.

The single-sine technique has the advantage of high quality data which results from the optimization of the instrumentation for a single frequency measurement e.g. proper selection of the current measuring resistor on the potentiostat. The instrumentation required to generate a single sine wave is less complicated than that of multi-sine which requires a computer or other device to calculate the waveforms to applied. High frequency measurements are possible and can be completed in very short times. The one

disadvantage of the single-sine technique is that at low frequencies, measurement time is long which could result in inconsistent data with systems that are time dependent. Although the electrochemical systems studied with this work do have a changing baseline, the time constant for that change is large enough compared to the measurement time to allow for the collection of consistent data over the entire frequency range of interest (Bard 1980).

In a linear system a perturbation x(t) yields a response y(t) which can be determined by the following n^{th} order differential equation (Gabrielli 1980,1990).

$$b_0 \frac{d^n y(t)}{dt^n} - b_1 \frac{d^{n-1} y(t)}{dt^{n-1}} - \ .... \ - b_n y(t) = a_0 \frac{d^m x(t)}{dt^m} - a_1 \frac{d^{m-1} x(t)}{dt^{m-1}} - \ .... \ - a_m x \quad (13)$$

Therefore, if x(t) is a sinusoidal input signal

$$x(t) = A \sin \omega t \quad (14)$$

then the resulting response is also a sinusoidal signal,

$$y(t) = B \sin(\omega t - \phi). \quad (15)$$

where ω is the frequency and ϕ is the phase angle. The impedance spectroscopy technique utilizes the fact that for a linear system, the response to a sinusoidal perturbation is also a sinusoid, but can be shifted in phase.

The impedance response of an electrochemical system is in the form of a complex number. This complex number con be represented either by a pair of polar coordinates or by a pair of Cartesian coordinates. In polar coordinates the total impedance at a given frequency is

$$Z(\omega) = Z e^{j\phi} \quad (16)$$

where $Z(\omega)$ is the impedance as a function of the angular frequency, ω, $|Z|$ is the magnitude of the impedance, j is the imaginary number Ö-1 and f is the phase angle.

The polar form of the impedance may be converted to rectangular or Cartesian coordinates by means of the Euler relation

$$e^{j\phi} = \cos\phi - j\sin\phi \qquad (17)$$

The total impedance now becomes

$$Z(\omega) = Z(\cos\phi - j\sin\phi) \qquad (18)$$

or by the sum of the real and imaginary parts

$$Z(\omega) = Z_r - jZ_j \qquad (19)$$

where Z_r is the real component of the impedance and Z_j is the imaginary component of the impedance.

$$Z_r = Z\cos\phi$$

$$Z_j = Z\sin\phi \qquad (20)$$

$$|Z| = ((Z_r)^2 + (Z_j)^2)^{\frac{1}{2}}$$

The phase angle, ϕ, is given in terms of Z_r and Z_j by

$$\phi = \arctan\frac{Z_j}{Z_r} \qquad (21)$$

A typical way to display data is in the complex plane where the negative imaginary component is plotted on the positive y axis versus the real component plotted along the x axis. The Bode plots consist of the magnitude of the impedance and the phase

angle plotted against the log of frequency. The complex plane plot can be further dissected into individual plots of real and imaginary components of impedance versus log of frequency.

In order to model impedance spectra with a linear model, one must be careful to use a small amplitude perturbation to ensure a linear response. Potential perturbation dictates linearity in corrosion systems and typical values for potential amplitude fall between 3.0 and 15.0 mV. The 'linear range' in which the amplitude must lie is determined by the polarization point. The high limit of the linear range is the point where non linear distortion begins and the low limit is determined by the signal to noise ratio. The maximum permissible amplitude decreases with frequency, however, for convenience, a constant perturbation amplitude is used for the entire frequency range for a given experiment. For this reason, a thorough investigation of the low frequency response is needed in order to properly set experimental parameters.

For this work numerical determination of linearity is conducted using a measurement model approach developed by Agarwal et al.(1993b). This technique utilizes a Voight equivalent circuit model which is consistent with the Kramers-Kronig relations to determine whether complex quantities for a system satisfy the conditions of causality, linearity and stability.

The basis for the typical EIS measurements is the application of either a potential or current perturbation and the measurement of the resulting signal, current or potential respectively. However, non-conventional techniques are being developed and are being proven to be useful tools in the analysis of a vast variety of systems. In an electrochemical

cell the flow rate of electrolyte to the surface of the electrode can be perturbed sinusoidally, and the resulting changes in current or potential measured. This is known as electrohydrodynamic impedance spectroscopy. Work to develop particle characterization techniques where electric fields are applied to a suspension of particles and the effective transmittance of light through the suspension is measured as the resulting signal is currently in progress. Modulation of the wavelength of light can also be used to perturb a system, a good example being that of a semi-conducting material which responds to light of different energies.
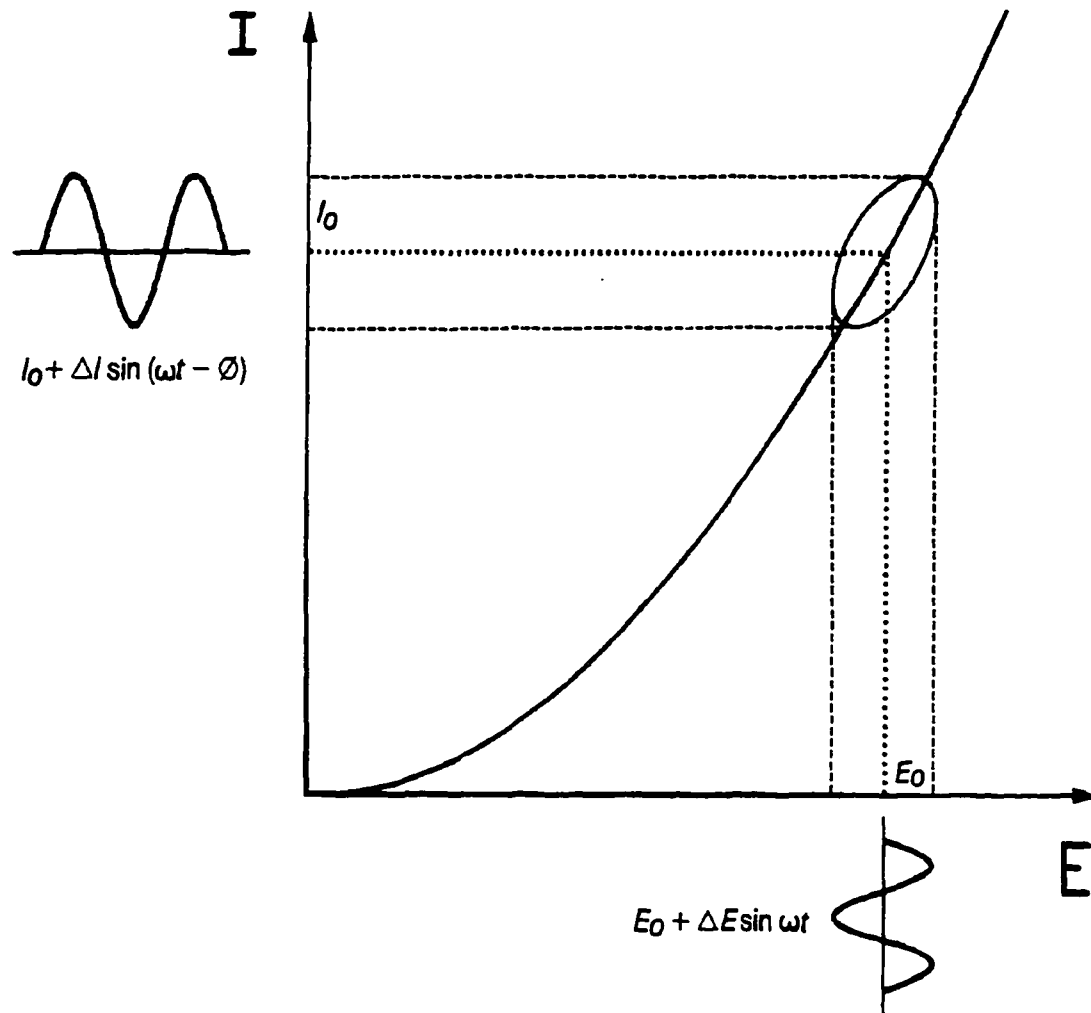
Figure 3.1: Current/Potential curves to demonstrate linear response from small signal perturbation (Gabrielli, 1980).

CHAPTER 4
EXPERIMENTAL METHOD

4.1 Impinging Jet System

The experimental design of this system was conceived in an effort to eliminate problems with existing designs and incorporate new techniques. A submerged axisymmetric impinging jet geometry was chosen for this study. The fluid mechanics within the region of the electrode are well-defined and has been studied extensively (Gilbert & LaQue 1954, Chin & Tsang 1978, Scholtz & Trass 1970a, 1970b). This geometry can be made to give uniform mass transfer rates across a disk electrode within the stagnation region. The stagnation region is defined to be the region surrounding the stagnation point in which the axial velocity is given by

$$v_z = -2\sqrt{a\upsilon}\,\phi(\eta) \tag{22}$$

and is independent of radial position, and the radial velocity is given by

$$v_r = ar\frac{d\phi(\eta)}{d\eta} \tag{23}$$

where a is the hydrodynamic constant which is a function only of geometry and fluid velocity, r and z are the radial and axial positions, respectively, v is the kinematic

viscosity, and ϕ is the stream function which is given in terms of dimensionless axial

position $\eta = z\sqrt{a/v}$ as (Chin & Tsang 1978)

$$\phi(\eta) = 0.656\eta^2 - 0.16667\eta^3 + 3.6444 \times 10^{-3}\eta^6 - 3.9682 \times 10^{-4}\eta^7 + ... \qquad (24)$$

Esteban et al. (1990) used ring electrodes to find that the stagnation region extends to a

radial distance roughly equal to the inside radius of the nozzle.

Within the stagnation region, the surface shear stress τ_{rz} is given by

$$\tau_{rz} = -1.312r(\mu\rho)^{\frac{1}{2}}a^{\frac{3}{2}} \qquad (25)$$

where μ and ρ are the viscosity and density of the fluid, respectively. The hydrodynamic

constant can be determined experimentally using ring or disk electrodes at the mass

transfer limited condition. Shear stress on the electrode surface as a function of jet

velocity for the range of velocities used in this work is presented in Figure 4.1. A desired

value of shear can be reached at an exact radial position by adjusting the jet velocity. This

positioning of a specific shear stress is valuable when observing dramatic phenomena

which only occur above a specified shear. The shear stress values reported in Figure 4.1

can be compared to the critical shear stress values reported by Efird (1977) for copper

(9.6 N/m^2) and 70/30 copper nickel (47.9 N/m^2).[2]

Mass transfer rate is uniform within the stagnation region; therefore, no

differential mass transfer cells can form near an electrode that lies entirely within the

stagnation region. The impinging jet system can therefore be used in the absence of

suspended particles to isolate the influence of the hydrodynamic shear stress. If the

removal of protective layers by hydrodynamic shear is the primary cause of erosion-

corrosion and the shear stress outside a certain critical radius is large enough to cause that removal, then the metal outside the critical radius will corrode at a significantly higher rate than the metal inside the critical radius. Since shear stress is a function of both radial position and jet velocity, the critical radius corresponding to the critical shear stress would be a function of jet velocity for fixed geometry.
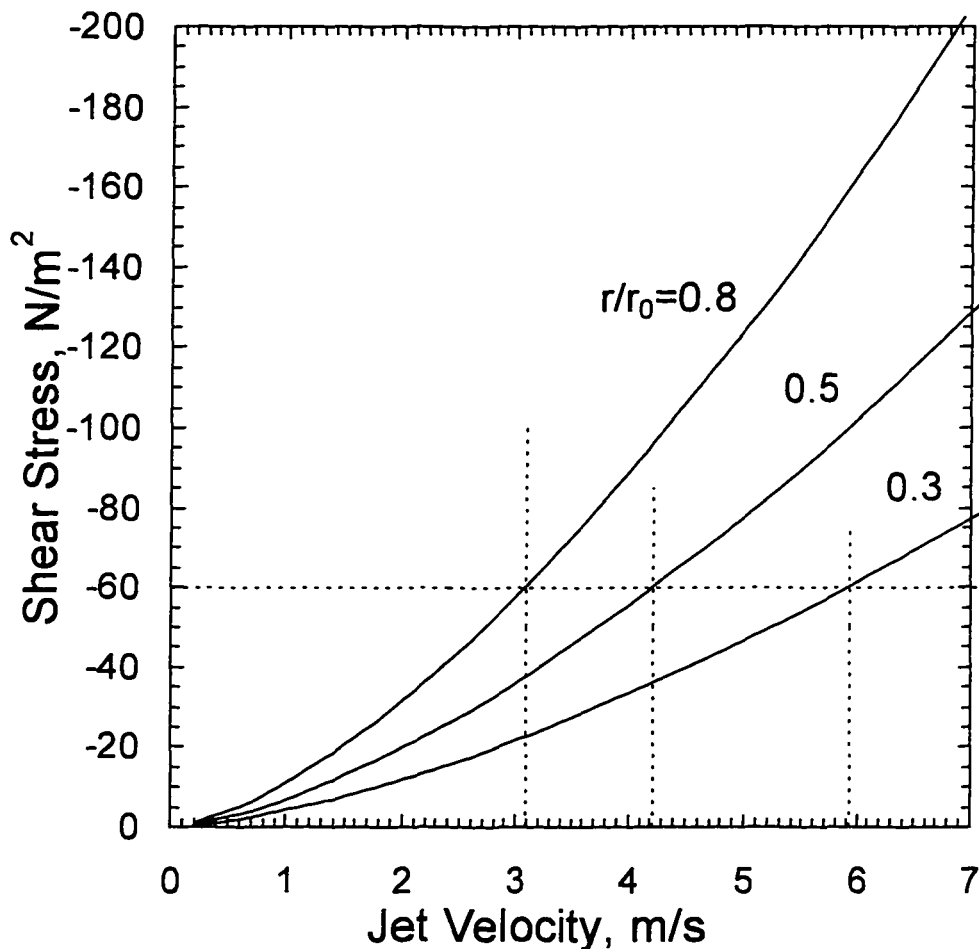
Figure 4.1: Shear stress as a function of jet velocity for the experimental work conducted here. The dimensionless quantity r/r_0 represents the ratio of the radial position/electrode radius.

The ability to use optical techniques *in situ* with the impinging jet system allows for the detection of radial variations on the electrode surface. In the current work, impedance spectroscopy and computer-interfaced and enhanced optical microscopy are used to provide information *in-situ* which can be coupled with potential measurements and *ex-situ* analysis. Variable-amplitude galvanostatically modulated impedance spectroscopy (Wojcik et al. 1996, 1997a,b,c) is an attractive technique because it can be used in a non-invasive manner.

An electrically isolated, magnetic-drive centrifugal pump was utilized to produce high flow rates without introduction of foreign species into solution. The impinging jet cell was outfitted with two access ports, one at 45° and the other at 60° from vertical. The primary objective of these ports was to allow in situ monitoring of the electrode surface with a video microscope. The port not occupied by the video microscope was designed to house probes to monitor cell conditions near the electrode surface. The electrochemical impedance instrumentation consisted of a EG&G PAR 273 potentiostat and a Solartron 1260 Impedance/Gain-Phase Analyzer. The instrumentation was controlled by a PC using Labview© and all interfacing code was written in-house.

A schematic of the experimental setup used in this work is shown in Figure 4.2. The system consisted of the impinging jet electrochemical cell, main solution reservoir, piping, pump, valves, connections, temperature controller and peripherals. The piping, connections and reservoir were constructed of polypropylene. Cooling coils submerged in the main reservoir to maintain the desired temperature were constructed of glass to obtain better heat transfer than polypropylene and eliminate any sources of contamination,

present with more conductive metal materials. The coil temperatures were controlled by a Fisher Scientific Isotemp Refrigerated Circulator model 910 and the pH of the solution was measured and controlled in the main reservoir by means of a Cole-Parmer model 5652-10 pH/ORP controller. A saturated calomel reference electrode for the system was also located in the main reservoir. The oxygen content of the solution was measured with a Cole-Parmer oxygen meter model 5946-50 and the solution conductivity was measured using a YSI Scientific model 35 conductance meter. The flow system pumped solution, via a centrifugal pump powered by a VARIAC power supply, from the bottom of the reservoir through a rotameter into the cell via the impinging jet and back to the main reservoir. The jet velocity was adjustable from 1.0 m/s to 6.75 m/s by modifying the VARIAC output and/or the bypass line throttle valve position.

The experimental cell, displayed in Figure 4.3 consisted of a submerged, axisymmetric impinging jet, a counter electrode, a working electrode with holder, an exit port, and two windows for viewing the sample *in-situ*. Early experiments showed a need for a large capacity cooling system to combat the warming effect of viscous dissipation at high velocities. To ensure accurate temperature control at the electrode surface, one of the window ports was outfitted with a thermometer to monitor cell temperature for comparison with reservoir temperature. The cell was constructed of acrylic sheet, 12.7mm thick and the base plate (bottom) of the cell was removable for access to the interior of the cell. The counter electrode was located on the top of the cell, parallel to the working electrode surface and was constructed of platinum foil of dimension 38.1mm x 50.8mm. The impinging jet was a 6.35mm I.D., 12.7mm O.D. acrylic tube approximately 1.0 meter long that was adjustable laterally and vertically to ensure the jet was centered

over the sample (if desired) and to allow for different h/D ratios. The sample under study was secured in the base plate of the cell by an adjustable sample holder which fixed the sample flush with the bottom plate. Two observation ports, 19.0mm in diameter were located in the two top-side plates of the cell. One of the observation ports was at a 45° angle from the base plate and the other was at a 60° angle from the base plate. The 60° angled port was retrofitted with the thermometer previously mentioned. These two angles were determined in the design of the cell to be the optimum and most adaptable to different electrode diameters respectively. The port windows were sapphire disks 4.5 mm thick held in place with an aluminum retaining ring on the outside of the cell and sealed on the interior with an o-ring. Chemical resistance to the synthetic sea water and optical properties were key in selecting sapphire for the observation windows. Sapphire has the optical property of high light transmission rates in the wavelengths of interest and scratch resistance.

The experimental system was controlled and data was collected by a Gateway 2000 4DX2-66V personal computer. The software used to run the various experiments was written in-house utilizing the graphical interfacing software Labview'. An EG&G Princeton Applied Research (PAR) Model 273 potentiostat/galvanostat and a Schlumberger SI 1260 impedance/gain-phase analyzer were connected to the PC via a GPIB connection. The PAR 273 controlled and measured the potential of the working electrode and the SI 1260 superimposed a sinusoidal potential wave and calculated the resulting impedance response.

The experimental cell was outfitted with a Hitachi color video camera model VK-C370 with a digital signal processor and a Navitar Zoom 6000 microscope lens system. Digital images from the camera were captured by a Coreco Oculus-TCX True Color Frame Grabber on the PC. These images were then viewed, processed, and stored. A Dolan-Jenner high intensity illuminator series 180 equipped with fiber optic multi-directional wands was used to supply the necessary light to collect video images.

4.2 Sample and Solution Preparation

The working electrodes for this work were constructed of 6.35mm diameter pure copper and copper nickel alloy rods mounted with epoxy in a 41.3mm diameter acrylic sample holder referred to here as a puck. Before construction of the puck the copper was annealed in a tube furnace at 750°C for 3.75 hours in an Argon atmosphere. A more reliable annealing procedure was adopted during the course of this work. The new technique involved annealing the rods in a vacuum furnace for 1 hour at 815°C. Initial annealing procedures were subject to oxygen contamination. Discoloration in the surface along the lines of flow of the argon gas were present after cooling of the sample. The new technique did not cause non uniform discoloration of the surface after annealing .

After casting the electrodes in the puck using a two part epoxy purchased from Buehler (part No. 20-8130-128, epoxide resin, No. 20-8132-032, epoxide hardener), rough wet polishing was performed on the electrode starting with 180 grit paper and working progressively down to 600 grit paper. The final stages of polishing were conducted using 1.0, 0.3, and 0.05 µm alumina powder, respectively, suspended on a

polishing cloth with de-ionized water. The sample was then cleaned with ethanol in an ultrasonic bath for approximately 1 minute and inserted into the experimental cell. The system was systematically flushed to remove any trapped air in the cell and tubing. The electrolyte solution for the experiments was ASTM-D-1141 synthetic sea water which was maintained at a pH between 8.05 and 8.3. To ensure constant light exposure to the system, fluorescent lab lights were kept on and exterior light was eliminated for the duration of each experiment. For capturing video images, additional lighting from an external light source was temporarily employed.

The synthetic sea water solution was prepared with ASTM-D-1141 sea salts which were combined with 2 MΩ deionized water. The solution was agitated and aerated with CO_2 scrubbed air for no less than 2 days to allow the salt to dissolve completely and to equilibrate the amount of dissolved O_2. Early experiments were not aerated with a pump, however, the large solution air interface in the reservoir and agitation from solution circulation provided some aeration. The difference in solution O_2 content between the pump aerated and partially aerates solutions was 1.0ppm, 7 and 6 ppm respectively. The solution was transferred to the experimental apparatus after the preparation period and circulated, which quickly brought the electrolyte to the desired temperature, 25°C.

4.3 Experimental Procedure

The series of experiments conducted for this work consisted of the monitoring of open circuit potential over time, periodic impedance experiments, and periodic recording

of video images. Each of these procedures provides vital information in the analysis of the corrosion mechanisms for the system.

The open circuit potential of the working electrode versus a saturated calomel reference electrode was measured as a function of time by a PAR 273 potentiostat. Periodically this measurement was suspended in order to conduct impedance experiments and record video images of the surface, after which the open circuit potential was again monitored. The open circuit potential value provides insight into the rate of corrosion and the state of the system, and can be used to identify systems that are changing rapidly or approaching a pseudo steady-state condition. All the electrodes tested for this work changed rapidly at first and then reached a pseudo steady-state condition. Flow rates were adjusted during the course of the experiments and the velocity effects on the impedance, corrosion potential, and visual appearance of the electrode surface were investigated.

Impedance scans were performed in the variable-amplitude galvanostatically modulated mode to prevent the introduction of a DC current driven by a shift in the corrosion potential. Three or more impedance scans were generated at each point of interest to verify reproducibility. For exploration of system with an unknown solution resistance, an initial, limited potentiostatic scan was performed over a few points at high frequency to determine the solution resistance, which was in turned supplied to the galvanostatic program as the initial impedance guess.

Ambient lighting supplied by fluorescent lab lights proved to be insufficient to illuminate the electrode to obtain a clear image capture. Therefore an external light source was used to momentarily illuminate the electrode for the purpose of obtaining an image

grab. As predicted, this introduction of additional light caused slight disturbances to the system due to the semi-conducting properties of the copper oxide films. Typically this disturbance resulted in a slight reduction in the impedance. Through experimentally monitoring the corrosion potential and impedance, it was determined that these minor disturbances were reversible over a short period of time and had no effect on the long term results.

Video images were utilized to learn about changes in the system over time, to detect polishing flaws before an experiment, and to investigate a small area of the electrode where an activity of interest may be taking place. Visual observation of the images yielded information about how and if the surface was evolving as a function of time. A key use of video images for this project was to determine if a radial dependence of the reaction rate existed. This was accomplished by examining the images for rings or halos which would suggest the presence of velocity-enhanced corrosion phenomena. The video images captured for this work were acquired using the minimum magnification, approximately 25X. The Hitachi camera and Navitar lens system used for this work both have the ability to zoom in on the sample. Immediately after all air had been removed from the system which took approximately three minutes, a video image was captured. This image provided valuable information even before any electrochemical experiments were conducted by exposing pre-existing flaws present on the surface of the electrode which were not otherwise visible either without magnification or without submersion in solution. Submersion made many flaws such as scratches more visible.

Temperature pH controller

Temperature/pH probe

counter electrode

rotometer

reference electrode

temperature control coils

sample holder

throttle valve

centrifugal pump

PAR 6310 personal computer

EG&G PARC model 273 potentiostat galvanostat
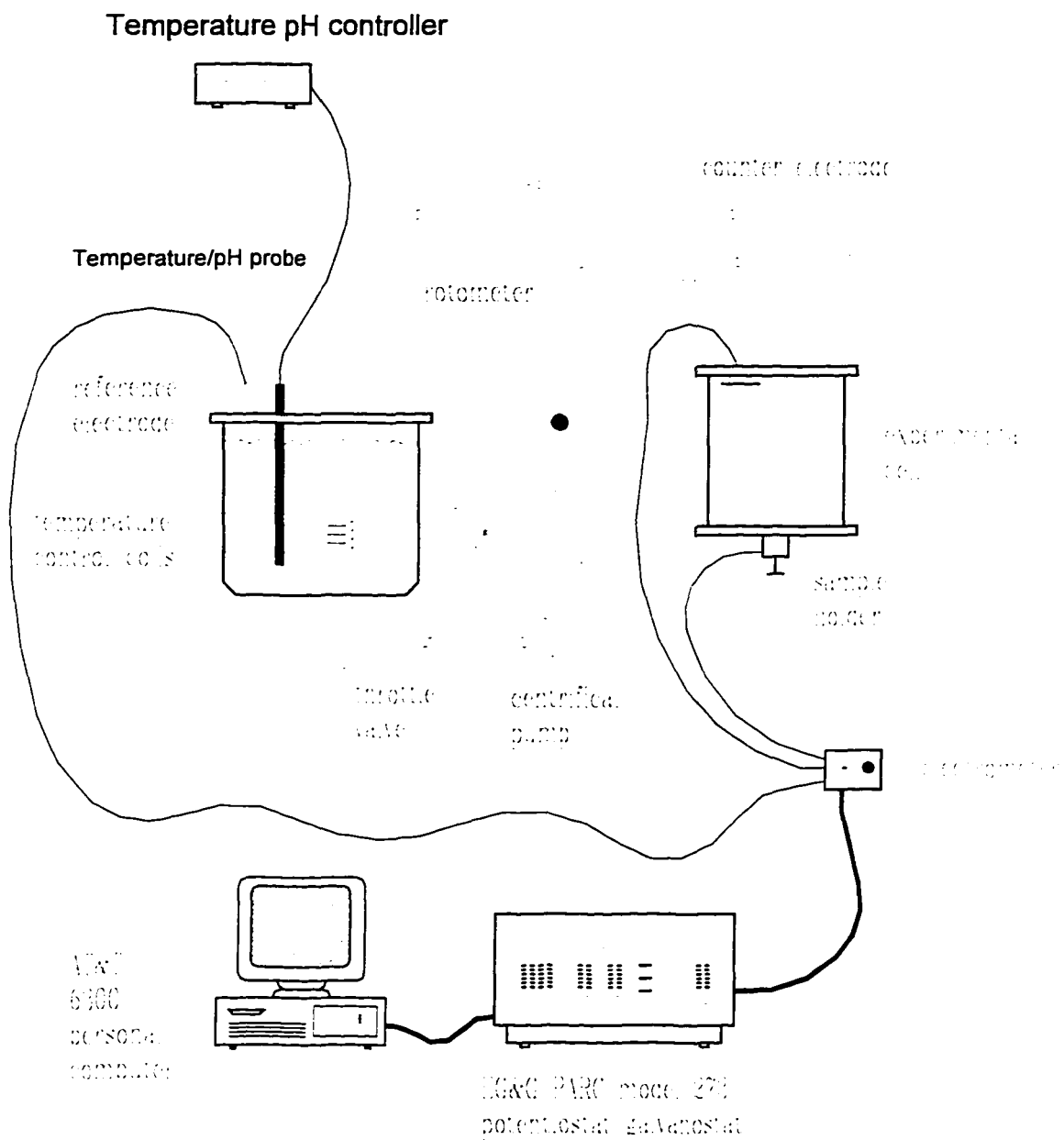
Figure 4.2: Experimental configuration used for investigating the influence of jet velocity on the corrosion of copper and copper alloys in synthetic sea water.
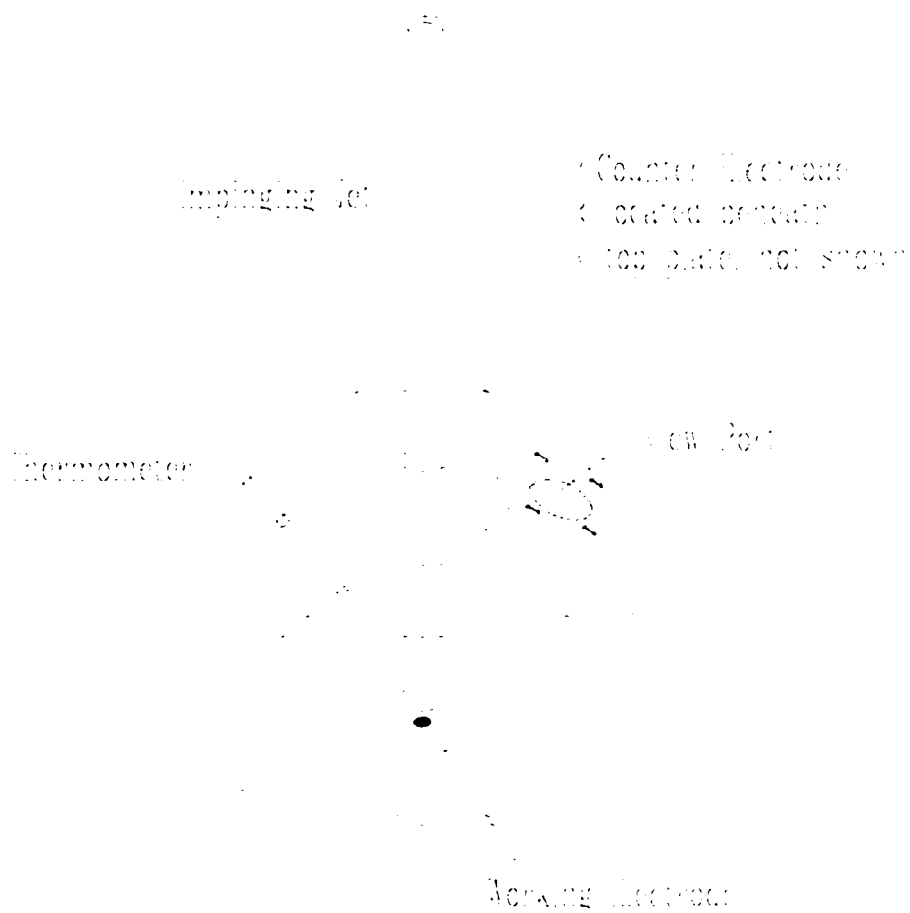
Figure 4.3: Schematic illustration of the impinging jet cell and important cell components.

CHAPTER 5
VARIABLE AMPLITUDE GALVANOSTATICALLY MODULATED IMPEDANCE SPECTROSCOPY

The variable amplitude galvanostatically modulated impedance technique was developed out of a necessity to conduct impedance scans on systems with changing baselines. A good example of such a system is a corrosion system where the corrosion potential is a function of time. Many factors can effect the characteristics of an electrochemical system and some of these factors can cause rapid changes in the corrosion potential. The potentiostatic as well as conventional galvanostatic methods of conducting electrochemical impedance experiments both have inadequacies investigating systems with a changing baseline.

Electrochemical impedance measurements are usually performed under potentiostatic regulation. In these measurements the potential is a fixed value with a superimposed (often sinusoidal) perturbation of fixed amplitude. This approach is attractive because linearity in electrochemical systems is controlled by potential. For example, a Taylor series expansion for current density at the open-circuit condition using the Butler Volmer equation (Butler 1924)

$$i = i_o \left\{ e^{\alpha_a F \eta_s / RT} - e^{-\alpha_c F \eta_s / RT} \right\} \tag{26}$$

yields

$$i = i_o \left\{ (\alpha_a + \alpha_c) \frac{F\eta_s}{RT} + \frac{(\alpha_a^2 - \alpha_c^2)}{2} \left(\frac{F\eta_s}{RT} \right)^2 + \frac{(\alpha_a^3 + \alpha_c^3)}{6} \left(\frac{F\eta_s}{RT} \right)^3 + O\left(\eta_s^4 \right) \right\} \quad (27)$$

where α_a and α_c are the apparent transfer coefficients for the anodic and cathodic reactions, respectively, η_s is the surface overpotential, F is Faraday's constant, R is the gas constant, and T is absolute temperature. For typical parameter values for a symmetric reaction ($\alpha_a = \alpha_c = 0.5$) and for T=298 K, the second term is equal to zero, and the third term is equal one percent of the first (linear) term for surface overpotentials of roughly 13.0 mV. Potential perturbations of 5 to 20 mV are often used. Potentiostatic regulation is usually used even for measurement of the impedance at the corrosion potential, a measurement which should, in principle, be conducted galvanostatically (with a time-averaged current density set equal to zero). The potential is set to the value of the corrosion potential at the beginning of the measurement and the potential is perturbed by a value sufficiently small to ensure linearity (EG&G 1985, Schlumberger 1993).

The need for a small amplitude potential perturbation is even greater for typical corrosion studies using impedance measurements conducted at the corrosion potential. Close to the corrosion potential for steel, hydrogen evolution is unimportant, and the oxidation of the metal can be assumed to be balanced by the mass transfer limited reduction of oxygen. Thus, the total current density normal to the pipe surface is given by

$$i_n = i_{0,Fe} \exp\left(\frac{\alpha_{Fe}F}{RT}(V - V_{Fe}) \right) - i_{O_2} \quad (28)$$

where α_{Fe} is the apparent transfer coefficient for the oxidation of iron (or steel), $i_{0,Fe}$ is the exchange current density for the oxidation of iron, V_{Fe} is the equilibrium potential for the

oxidation of iron, V is the applied potential, and i_{O_2} is the mass transfer limited current density associated with reduction of oxygen. Note that a cathodic current is assumed to be negative following the conventions used in electrochemical literature. At the corrosion potential $V = V_{corr}$, the net current i_n is equal to zero, and

$$V_{corr} = V_{Fe} + \frac{RT}{\alpha_{Fe} F} \ln\left(\frac{i_{O_2}}{i_{0,Fe}} \right)$$

(29)

An increase in the mass transfer limited current for oxygen reduction will shift the corrosion potential to more positive values, and will, thereby, increase the rate of corrosion. Equation (29) can be rewritten in terms of the corrosion potential as

$$i_n = i_{O_2} \left\{ \exp\left(\frac{\alpha_{Fe} F}{RT} (V - V_{corr}) \right) - 1 \right\}$$

(30)

At low current densities, linearization of the exponential term about the corrosion potential yields

$$i_n = i_{O_2} \left\{ \left(\frac{\alpha_{Fe} F}{RT} (V - V_{corr}) \right) + \frac{1}{2} \left(\frac{\alpha_{Fe} F}{RT} (V - V_{corr}) \right)^2 + \ldots \right\}$$

(31)

In contrast to the expansion for the Butler-Volmer reaction, the second term contributes to the expansion and is equal to one percent of the first (linear) term for potentials as small as 1.0 mV if $\alpha_{Fe} = 0.5$.

Potentiostatic regulation is satisfactory for measurement of the impedance at the corrosion potential if the corrosion potential does not change during the course of the measurement. Under conditions where the corrosion potential is changing with time, the potentiostatically-controlled impedance scan alters the behavior of the system under study

by forcing the potential to be constant during the period of the measurement. A schematic representation of the influence of potentiostatically controlled impedance spectroscopy on a system with a changing corrosion potential is given as Figure 5.1. The potential decay represented in Figure 5.2 could be the result of growth of surface films associated with corrosion products or calcareous deposits. The impedance measurement in this case is invasive because the decay in potential is arrested during the measurement. As illustrated in Figure 5.1, one consequence of the applying a fixed potential for a system in which the corrosion potential would otherwise be changing is that the dc component of the current becomes non-zero. For corrosion measurements, the resulting anodic or cathodic current can disrupt the growth of surface films and can lead to current overloads.

Galvanostatic modulation of impedance experiments eliminates application of a potential that is anodic or cathodic to the true open-circuit potential. Under galvanostatic control, the desired zero-current baseline condition is maintained throughout the impedance measurement, even when the corrosion potential drifts during the course of the measurement of a impedance spectrum. The difficulty with galvanostatic measurements with a fixed amplitude for the current perturbation is that such measurements can result in severe swings in potential, especially at low frequencies where the impedance is large. The amplitude of the potential variation $\Delta \tilde{V}$ associated with a perturbation amplitude of current $\Delta \tilde{I}$ is given by

$$\Delta \tilde{V} = \Delta \tilde{I} |Z(\omega)| \tag{32}$$

A current perturbation as small as 5 μA can result in potential swings of 500 mV for systems with a polarization resistance of 10^5 Ohms, a value typical of many membranes and some slowly corroding systems, *e.g.*, systems with well developed, dense films.

The potential swing associated with galvanostatically modulated impedance measurements with a fixed perturbation amplitude can be significant even for systems with a small polarization impedance. The potential perturbations resulting from three fixed amplitude current perturbations on an RC circuit are shown in Figure 5.3. The magnitude of the impedance for this system changed only one order of magnitude over the entire frequency range. Yet, if a sufficiently large current amplitude is used to ensure an acceptable signal-to-noise ratio at high frequency (e.g., 10 mV), the potential perturbation at low frequency can be dangerously high and results here in a potential swing of 100 mV (see triangles). For many systems a 100 mV perturbation is well above the threshold defining linearity. Conversely, if care is taken to choose a current perturbation which will ensure that the low frequency potential perturbation is within the limits of linearity, the high frequency potential response can fall below the resolution limits of the potentiostat.

An algorithm was developed in which galvanostatic regulation is conducted with an amplitude of current perturbation that is adjusted at each frequency to yield a desired variation in potential (Wojcik et al. 1996). This approach retains the advantage of

galvanostatic modulation that the experiment does not disturb the transients that would otherwise exist in the system while ensuring the maximum signal-to-noise ratio for perturbations that stay within the linear regime. The objective of this work is to present recent improvements to the variable-amplitude galvanostatic modulation algorithm and to demonstrate its utility for monitoring transient corrosion processes.
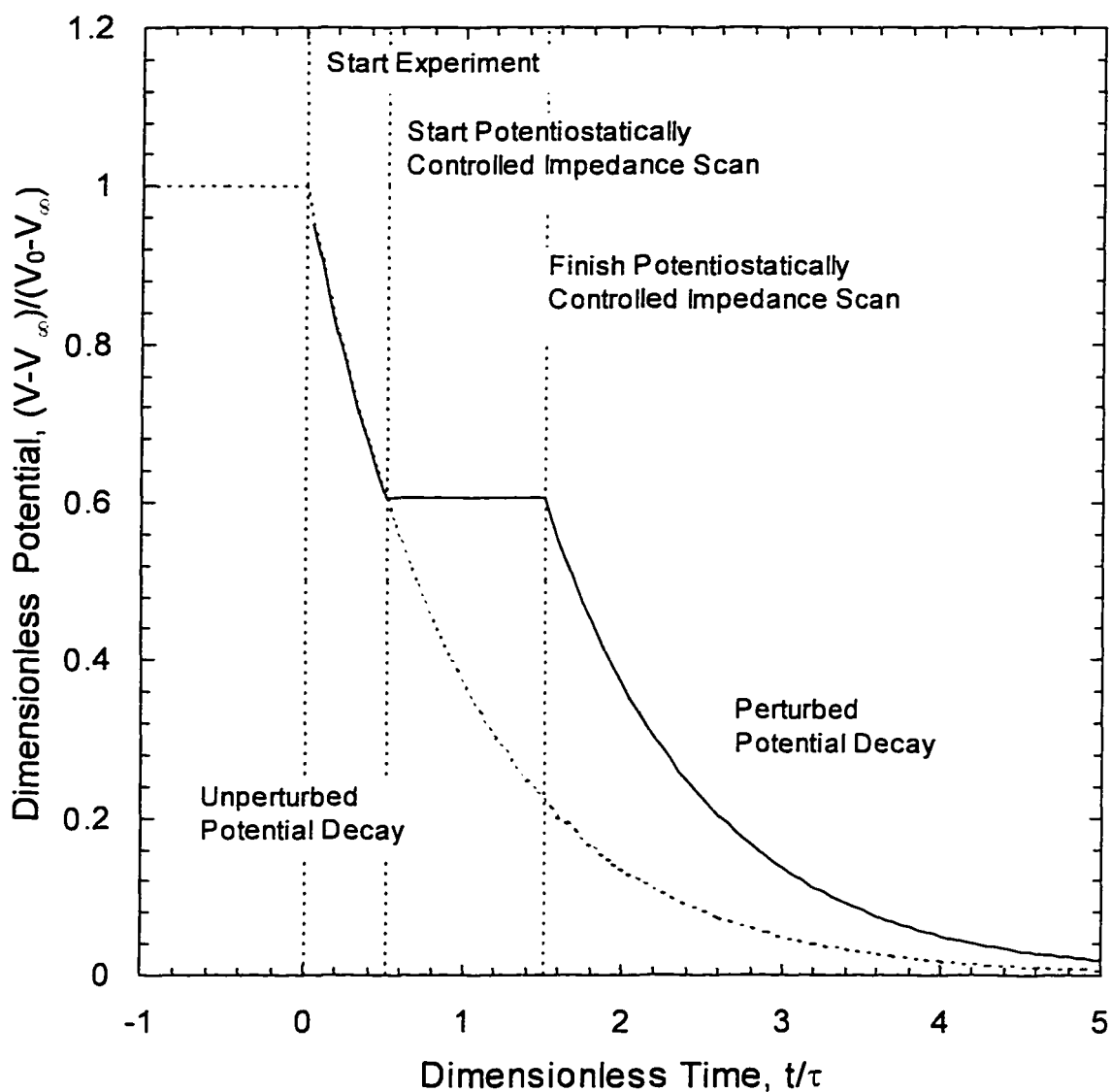
Figure 5.1: Schematic illustration of the influence of a potentiostatic impedance experiment on the corrosion potential of a system with a changing baseline.
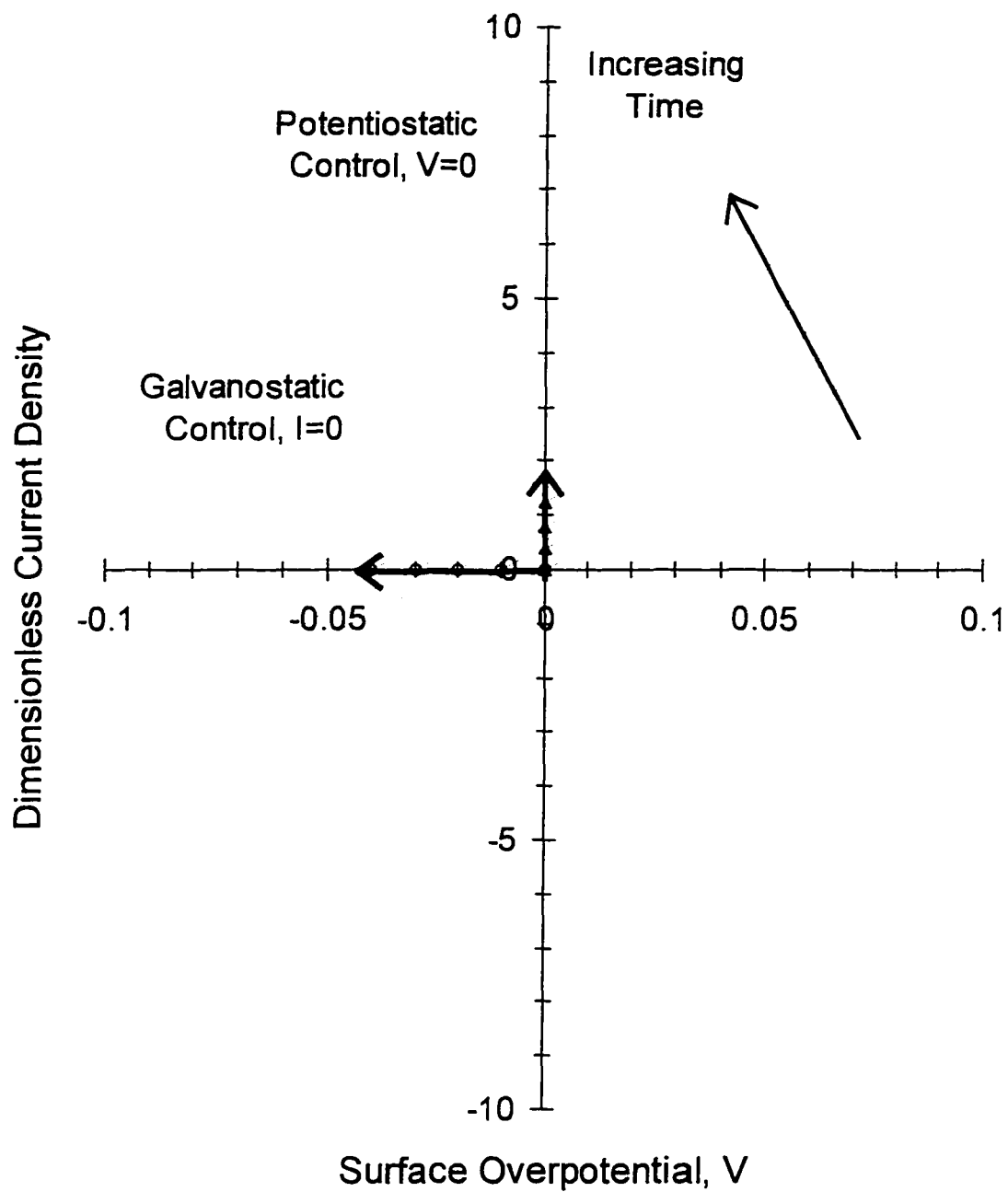
Figure 5.2: Sequential current potential curves for a system with a transient corrosion potential.
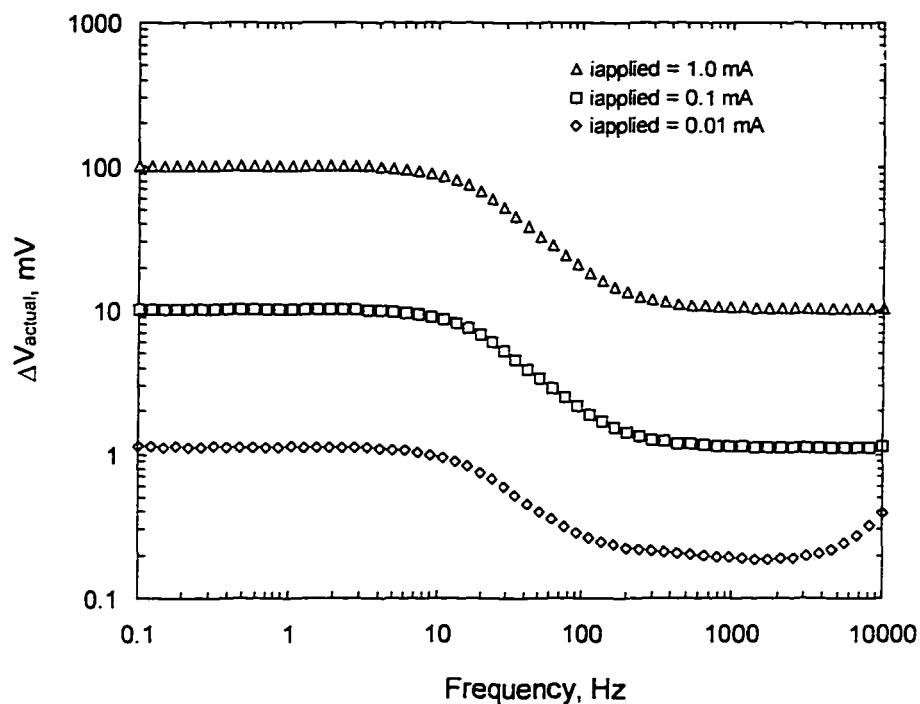
Figure 5.3: Potential perturbation for test circuit, Circuit 1, resulting from traditional galvanostatic impedance measurements using fixed amplitude current perturbations.

5.1 Variable-Amplitude Galvanostatic Modulation Algorithm

The variable-amplitude galvanostatic algorithm consists of a method to select an appropriate amplitude for the current perturbation and for the current measuring resistor. The algorithm was implemented using LabView for Windows[s] on an IBM-compatible computer.

5.2 Prediction of the Amplitude of the Current Perturbation

Measurements at previous frequencies are used to estimate the value of the impedance at the target frequency. The current perturbation to be used is given by

$$\Delta \tilde{I}(\omega) = \frac{\Delta \tilde{V}_{\text{target}}}{|Z(\omega)|_{\text{estimated}}}$$ (33)

where $\Delta \tilde{I}(\omega)$ is the current perturbation at a given frequency, $\Delta \tilde{V}_{\text{target}}$ is the desired potential perturbation at the surface of the electrode, and $|Z(\omega)|_{\text{estimated}}$ is the magnitude of the impedance taken from the preceding measurement. In this approach, the magnitude of the impedance at the frequency to be measured is predicted from values obtained at previously measured frequencies. This prediction is therefore done without additional probing of the system. A sequential collection of data in logarithmic increments of decreasing frequency is assumed.

In early work (Wojcik et al. 1996), a one-point prediction algorithm was employed which was defined by

$$Z(\omega_k) = Z(\omega_{k-1}) + O\left(\log\left(\frac{\omega_k}{\omega_{k-1}}\right)\right)$$ (34)

where the impedance at frequency ω_k is assumed to be equal to the impedance at ω_{k-1}. The error in equation (34) is of the order of the inverse number of points per decade. In the present work (Wojcik & Orazem 1997a) equation (34) was replaced by

$$Z(\omega_k) = 3Z(\omega_{k-1}) - 3Z(\omega_{k-2}) + Z(\omega_{k-3}) + O\left(\log\left(\frac{\omega_k}{\omega_{k-1}}\right)\right)^2$$ (35)

The error in equation (35) is of the order of the square of the inverse number of points per decade. For 10 points per decade, an order of magnitude improvement can be expected when equation (35) is employed as compared to equation (34).

At the first measured frequency, the initial guess for the impedance is used. The estimated solution resistance provides a good initial guess for impedance scans made from high frequency to low. At the second measured frequency, equation (34) is used. At the third measured frequency, the estimated impedance is obtained from a two-point formula

$$Z(\omega_k) = 2Z(\omega_{k-1}) - Z(\omega_{k-2}) + O\left(\log\left(\frac{\omega_k}{\omega_{k-1}}\right)\right)^2 \tag{36}$$

which has an accuracy of the order of the square of the inverse number of points per decade. The 3-point algorithm given as equation (35) provides a refinement to the 2-point algorithm by including an estimate for the second derivative of impedance with the log of frequency.

A comparison of the one-point and three-point algorithms is presented in Figure 5.4 for an RC test cell. The largest errors in the prediction algorithm appear at frequencies where the impedance is a strong function of frequency. For a 10 mV target perturbation, the one-point technique, displayed by triangles, results in a maximum perturbation of 11.7 mV. The maximum error in the three-point variable amplitude prediction is 0.2 mV for the one-point method as compared to 1.7 mV for the one-point algorithm. The largest error for the three-point algorithm is at the first measured frequency where an initial guess is used to predict the appropriate current perturbation.
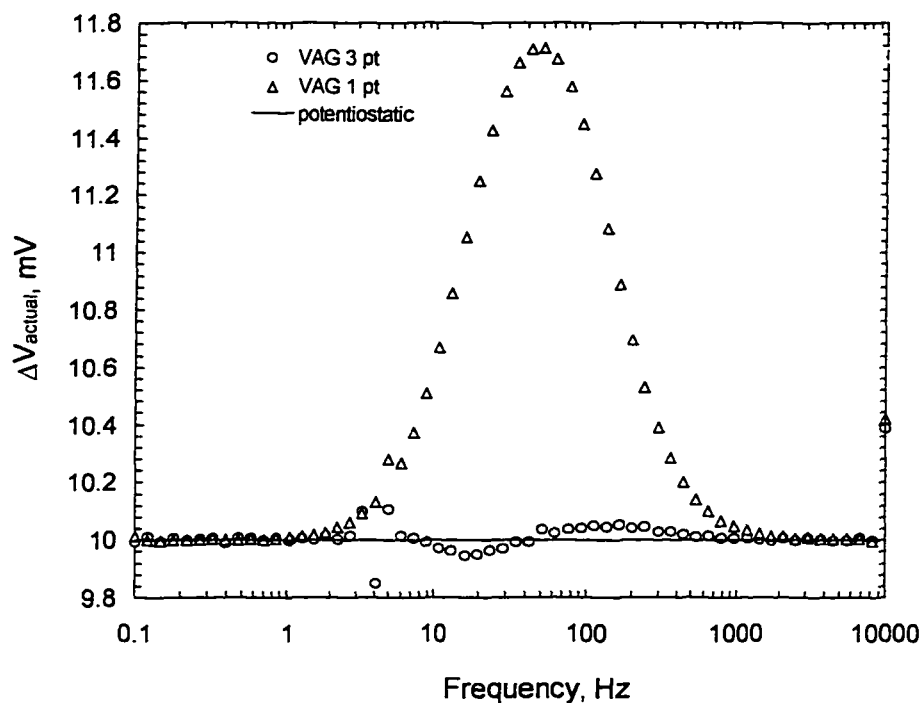
Figure 5.4: Comparison between the one point and three point prediction methods for the variable amplitude algorithm with a 10 mV target potential perturbation.

The value of the current perturbation obtained from the algorithm is used to guide automated selection of the current measuring resistor. Automated selection of current measuring resistors is not new (Kendig et al. 1984), but its implementation is an essential feature of the algorithm. Several changes of the current measuring resistor are often needed because the current perturbation may vary over several orders of magnitude during a scan.

5.3 Prediction of the Value for the Current Measuring Resistor

When operating in the galvanostatic mode proper selection of R_m is of the utmost importance. The computer code for controlling the potentiostat was designed to

automatically select the proper R_m for the current to be applied (refer to Table 5.1). To compliment the algorithm used to predict the current perturbation at the next frequency, an algorithm to determine the optimum current measuring resistor to be used was also developed. The current measuring resistors available for the EG&G PAR Potentiostat/Galvanostat Model 273 are presented in Table 5.1 along with the nominal current ranges for each selection. Each of the current measuring resistors can measure currents from 15 to 190% of the posted current magnitude with the exception of the 1Ω resistor which can measure up to 200% of the posted current magnitude. Selection of the proper current measuring resistor is crucial to ensure reliable data collection. Selection of too large a current measuring resistor will result in a current overload in the potentiostat while too small a current measuring resistor will introduce noise into the measurement resulting in a poor signal to noise ratio.

One can observe from Table 5.1 that there is an overlap of adjacent resistor values. As a rule of thumb, measurements that are conducted to the side of full range measurements tend to be more sensitive than those taken at the lower limits of the allowable range i.e. a current value of 17 mA would be more accurately measured using the 100Ω rather than the 10Ω current measuring resistor. There are, however, situations where the expected current from and electrochemical experiment is augmented by an additional current present due to noise, external perturbation, or change in the system under study. These unpredicted sources of current can cause difficulties if not handled properly by the potentiostat. When the selection of the optimum current measuring resistor is based solely on the perturbation being applied, the additional currents will in

many instances cause a current overload condition. With the new current measuring

resistor selection algorithm, a more conservative approach can be taken in situations

where overloads are common. The algorithm for selecting the proper current measuring

resistor was based on calculation of

$$\log\left|\frac{i_{predict}}{i_{min}}\right| = x.y \tag{37}$$

where x and y are the characteristic and mantissa of the logarithm, respectively, $i_{predict}$ is

the predicted value for the current, and i_{min} is the nominal minimum measurable current

for which the instrument, given in Table 5.1 to be 100 nA. A switch-over factor y_c can be

defined, which has a value between 1.5 and 1.9. If $y \leq y_c$, the current measuring resistor

index is obtained from $k_R = 7 - x$. If $y > y_c$, $k_R = 6 - x$. This algorithm has the feature

that it does not depend on past history, and increases or decreases in current measuring

resistor values are possible based on the predicted current value.

defined, which has a value between 1.5 and 1.9. If $y \leq y_c$, the current measuring resistor

index is obtained from $k_R = 7 - x$. If $y > y_c$, $k_R = 6 - x$. This algorithm has the feature

that it does not depend on past history, and increases or decreases in current measuring

resistor values are possible based on the predicted current value.

Another important issue involving controlling current is maintaining a zero

current condition before the initiation of an applied current. Instrumental limitations led

to control problems with this work before impedance scans were initiated. For example,

the PAR 273 potentiostat has a current measuring accuracy of 0.2% in the range 10μA to

1A which correspond to the 1000 and 1 Ω resistors respectively. If in the galvanostatic mode a 1 Ω resistor is chosen and a zero current condition is desired, the best control achievable is ± 2.0 mA. This level of control is unacceptable in this work due to the sensitivity of the copper / sea water system to applied currents. If on the other hand, a 10 MΩ resistor is chosen, the instrument is operating in the current range 100 nA to 1 μA which has an accuracy of 0.5%. The limit of control under galvanostatic regulation of zero current is now 0.5 nA which correlates to a 4×10^8 % improvement in the ability of the instrument to maintain zero current.

Table 5.1: Current measuring resistor ranges for a PAR 273 potentiostat.

Current Measuring Resistor Index, k_R	Measuring Resistor Value	Nominal Current Value	Nominal Current Range
0	1Ω	1 A	150 mA - 2 A
1	10Ω	100 mA	15 mA - 190 mA
2	100Ω	10 mA	1.5 mA - 19 mA
3	1000Ω	1 mA	150 μA - 1.9 mA
4	10000Ω	100 μA	15 μA - 190 μA
5	100000Ω	10 μA	1.5 μA - 19 μA
6	1MΩ	1 μA	150 nA - 1.9 μA
7	100MΩ	100 nA	15 nA - 190 nA

The value for $i_{predict}$ is calculated differently depending on which mode of operation, galvanostatic or potentiostatic, is used. For galvanostatic regulation, $i_{predict}$ is calculated by

$$i_{predict} = \frac{V_{target}}{Z_{predict}} + i_{bias} \tag{38}$$

and by

$$i_{predict} = \frac{V_{perturb}}{Z_{predict}} + i_{pol} \tag{39}$$

under potentiostatic regulation. In the above equations V_{target} is the desired potential perturbation at the electrode surface, $Z_{predict}$ is the value predicted for the impedance whether an initial guess or a value calculated by the prediction algorithm, i_{bias} is a current bias applied by the potentiostat, and i_{pol} is any dc current present after a potential bias is set.

5.4 Application to Corrosion Measurements

The copper/synthetic sea-water system chosen to illustrate the benefits of the variable amplitude potentiostatic algorithm is strongly affected by the formation of salt and oxide films. The corrosion potential of a freshly polished copper electrode submerged in electrolyte changes rapidly at first due to the formation of films then reaches a pseudo steady-state condition after a period of several days. Impedance spectroscopy can be used as a non-invasive tool for assessing the reactivity of the copper electrode during a long-

term measurement of the corrosion potential if the amplitude of the perturbation is sufficiently small and if the measurement does not perturb the baseline condition of the electrode.

Potentiostatic experiments, due to their nature, do not maintain a zero current condition throughout an experiment in which the corrosion potential changes with time. For a potentiostatic experiment, the corrosion potential is manually or automatically read and a potential bias of that value is applied. The sinusoidal perturbation of an impedance scan is then superimposed over this potential bias. If the open-circuit potential is stable, the set bias will yield a zero or near zero current. If, however, the open-circuit potential changes during the course of the experiment, in the latter stages of the measurement, the bias potential will drive a anodic or cathodic current.

It is clear that potentiostatically regulated impedance measurements are invasive for systems that have a changing corrosion or open-circuit potential. For such systems, the zero-current condition can be assured only through use of galvanostatic control. For conventional galvanic experiments, however, a fixed current amplitude is used which can lead to poor signal-to-noise ratios, non-linearity, or both. Use of a single fixed value for the current perturbation is inappropriate for the typical electrochemical systems characterized by a magnitude of the impedance which varies over several orders of magnitude with frequency. For the copper system used in this work the magnitude of the impedance changed almost three orders of magnitude over the measured frequency range.

Data presented in Chapter 6 show a protective film on the surface of a copper electrode disturbed by applied potentials as low as 50 mV. Higher impedance indicates a

more protective film which can be removed or modified by sufficiently high applied potentials.

5.5 Comparison With Other Techniques

A direct comparison between the variable amplitude galvanostatic, conventional galvanostatic, and potentiostatic techniques was performed to determine the most appropriate technique to conduct electrochemical impedance experiments. Data were collected for solid state systems as well as copper / synthetic sea water systems as a means of comparison. The first system investigated was an electrical circuit with two different sets of parameter values. The configuration of the circuit is displayed in Figure 5.5 and the parameter values for each component in the test cells used for this work are given in Table 5.2. The configuration and electrode connections of this circuit remained constant and only the element values were changed for different experiments.
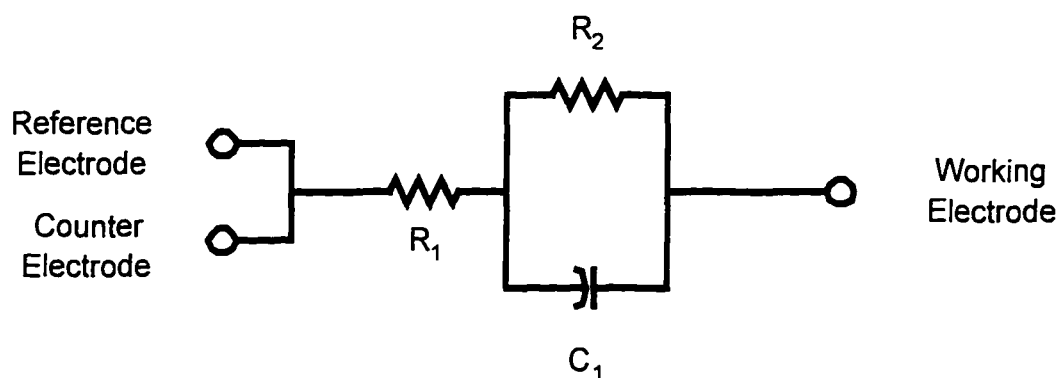
Figure 5.5: Test circuit and connections.

Table 5.2: Parameter values for electrical circuits 1 and 2. Circuits 1 and 2 can be visualized by insertion of R and C values into Figure 5.5.

Circuit	R1, Ω	R2, Ω	C1, μF
1	10	100	100
2	10	10000	1000

Results from impedance scans conducted on circuit 1 reveal problems with the fixed galvanostatic mode of operation. Figure 5.7 presents data collected in the conventional and variable galvanostatic as well as the potentiostatic mode. As one might expect, no problems were attributed to the potentiostatic method on the solid state system because a low amplitude potential perturbation of, 10mV was applied and the baseline potential equals zero due to the absence of any chemical reactions. Conventional galvanostatic operation does lead to problems even with the electrical circuit when low current perturbation amplitudes are attempted. Figures 5.8 and 5.9 display data revealing a serious problem when a current perturbation of 0.01mA is attempted. This current amplitude would yield an 11 mV potential perturbation at low frequency which is well within the measuring capability of the potentiostat, however the problem is initiated at high frequency where the potential response is on the order of 1 mV which borders on the measurable limit of the potentiostat. The shaded circles in Figures 5.7 - 5.9 show a +10 ohm discrepancy in the 0.01 mA spectra from what the model predicts and other experimentally determined values. It can also be observed that the high frequency imaginary component of the impedance is positive. Although one might expect signal to

noise problems at high frequency, a 10 mV potential response is present at low frequencies which is well within the measuring capabilities of the PAR 273. The imaginary component of the 0.1 mA current perturbation exhibits abnormal behavior at high frequency which can be seen from Figure 5.9 where the imaginary impedance is plotted versus the log of frequency.

To eliminate the possibility of a defective 100 kΩ current measuring resistor, a new circuit of higher impedance was constructed to utilize the same current perturbation of 0.01 mA with a different resulting potential. Figures 5.10 and 5.11 shows that the positive shift in the real component of the impedance is independent of the current measuring resistor used, in this case the 1MΩ resistor. The above test were repeated with a FRA 1250 and a different PAR 273 without computer control and yielded the same results indicating that the problem was not due to defective equipment but to inadequate ability of the instrumentation to measure potentials at or near 1 mV. This work revealed that for situations where the PAR 273 is required to measure potentials close to the instrument's minimum limit, an internal gain is set causing the discrepancy in real component of the impedance. Apparently this gain is implemented for the duration of the scan causing a bias error of approximately ten ohms in the value of the real component. The high frequency data for the 0.01 mA current amplitude also shows inconsistent behavior which is not attributed to the internal instrument gains.
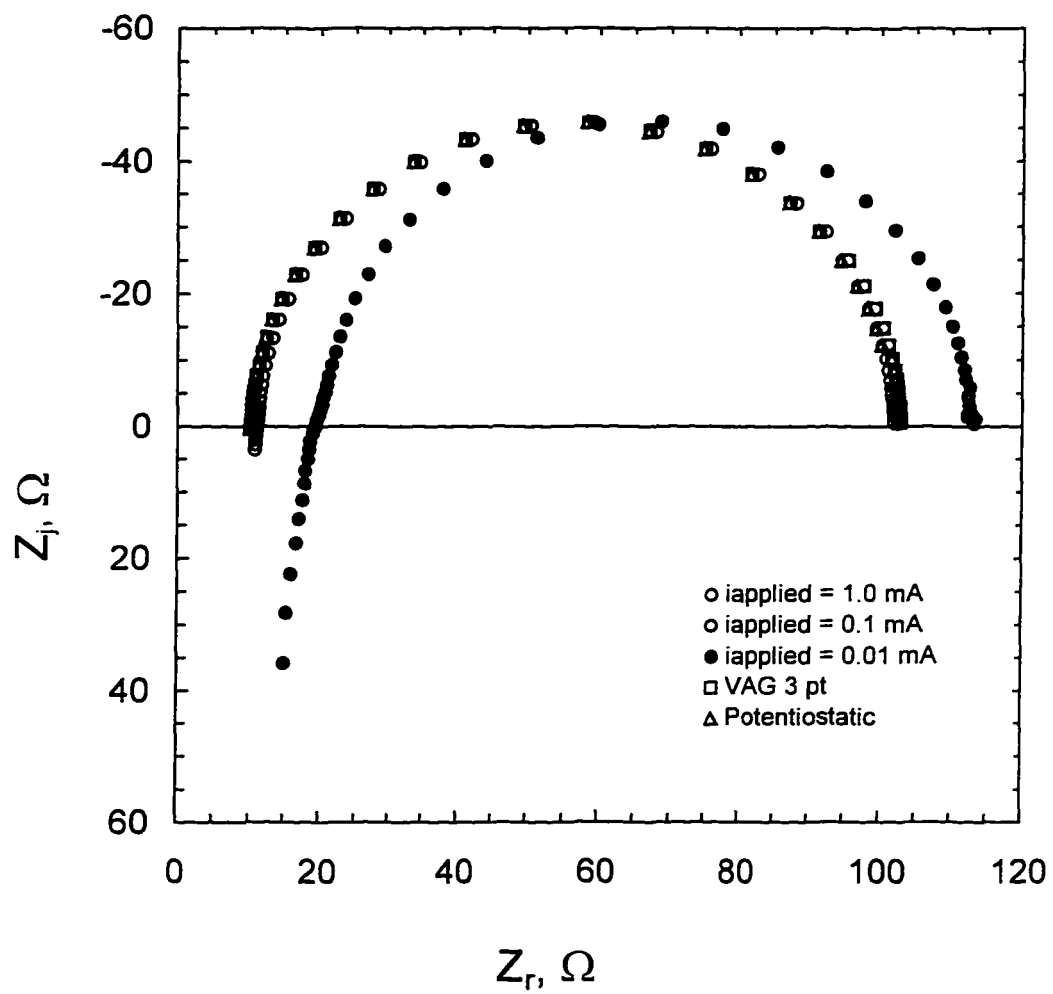
Figure 5.7: Impedance plane plot for test circuit Cell 1 comparing conventional galvanostatic, VAG, and potentiostatic techniques.
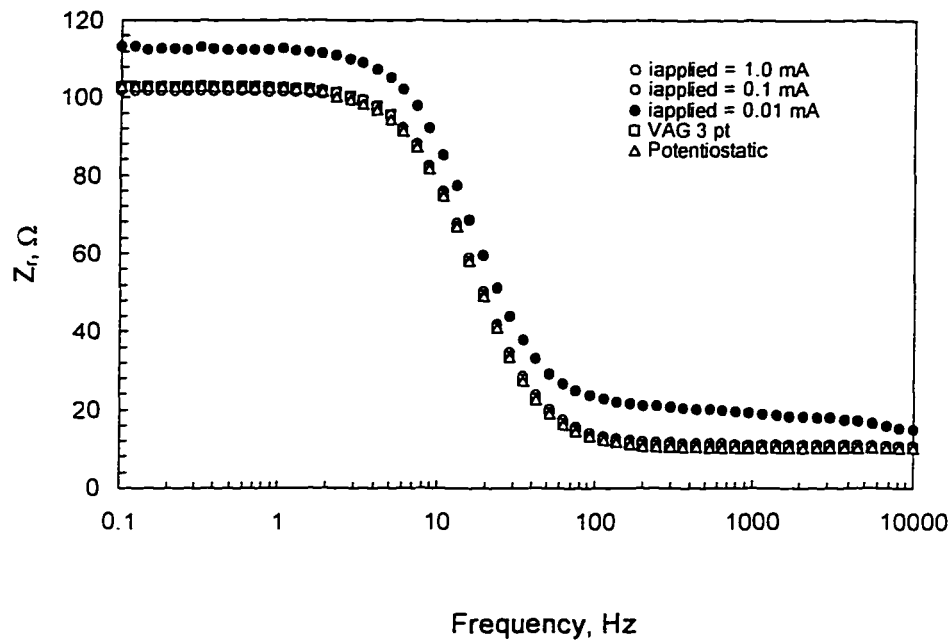
Figure 5.8: The real component of the impedance as a function of frequency for test circuit Cell 1 comparing conventional galvanostatic, VAG, and potentiostatic techniques.
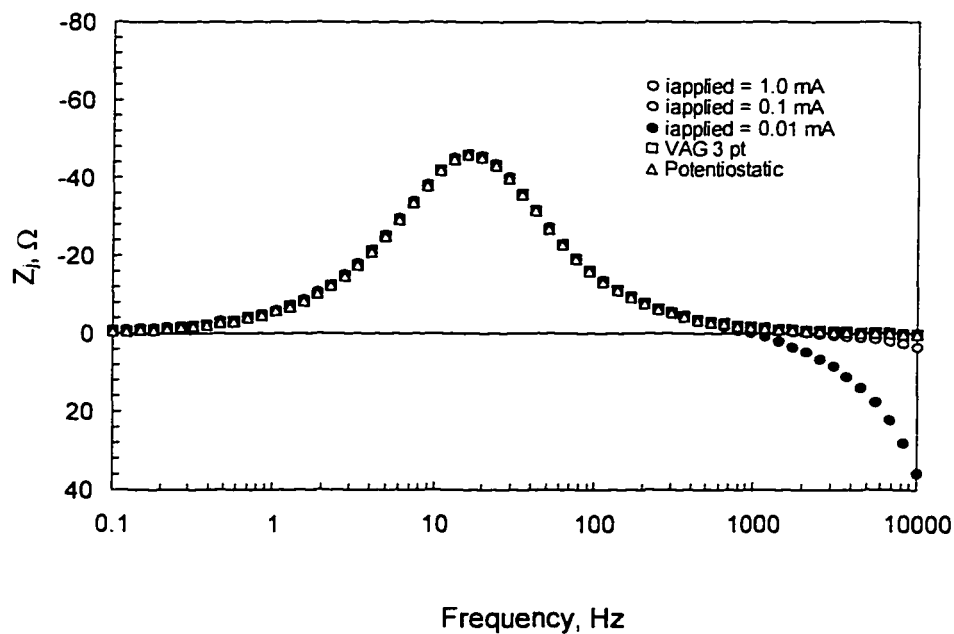
Figure 5.9: The imaginary component of the impedance as a function of frequency for test circuit Cell 1 comparing conventional galvanostatic, VAG, and potentiostatic techniques.
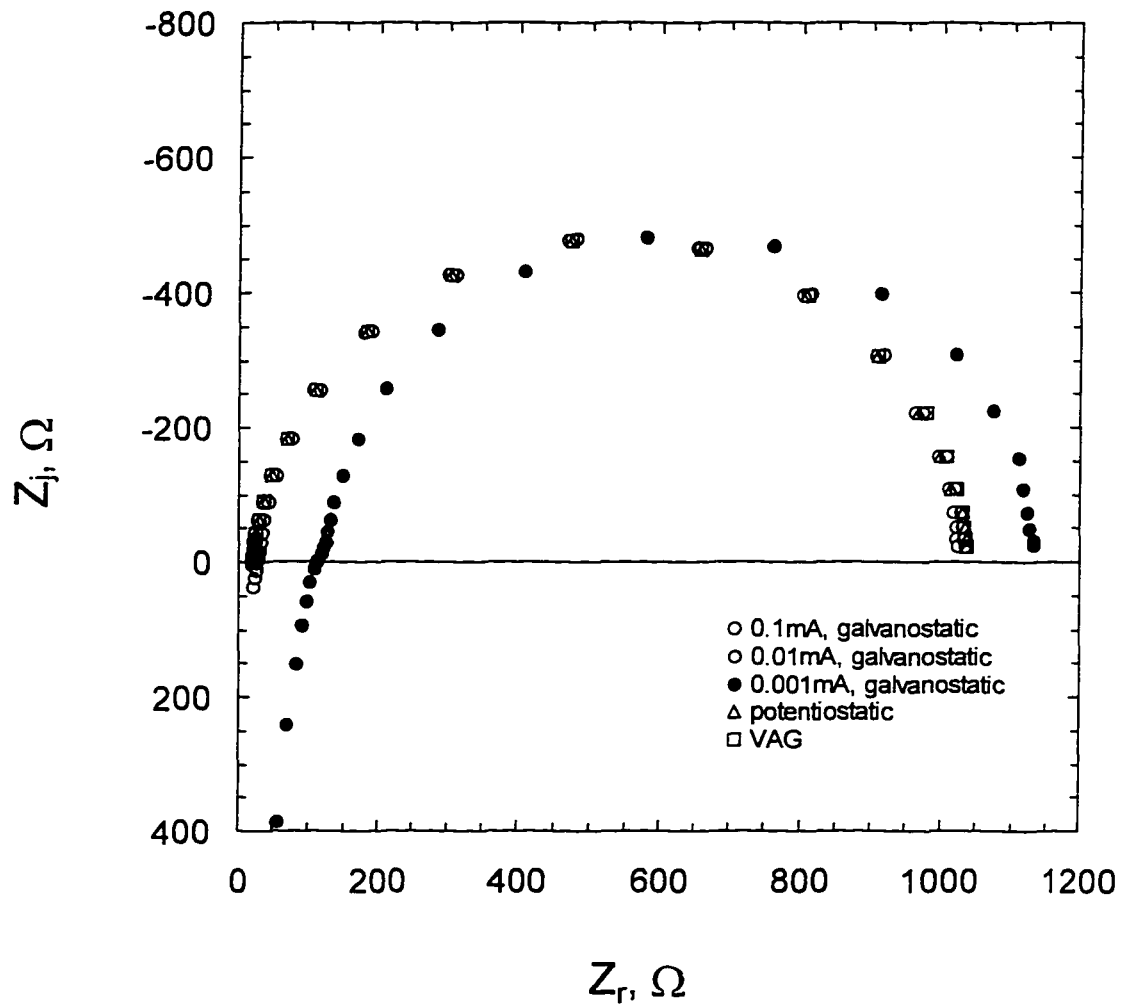
Figure 5.10: Impedance plane plot for test circuit Cell 2 comparing conventional galvanostatic, VAG, and potentiostatic techniques. Note the order of magnitude change in the impedance values compared to Cell 1.
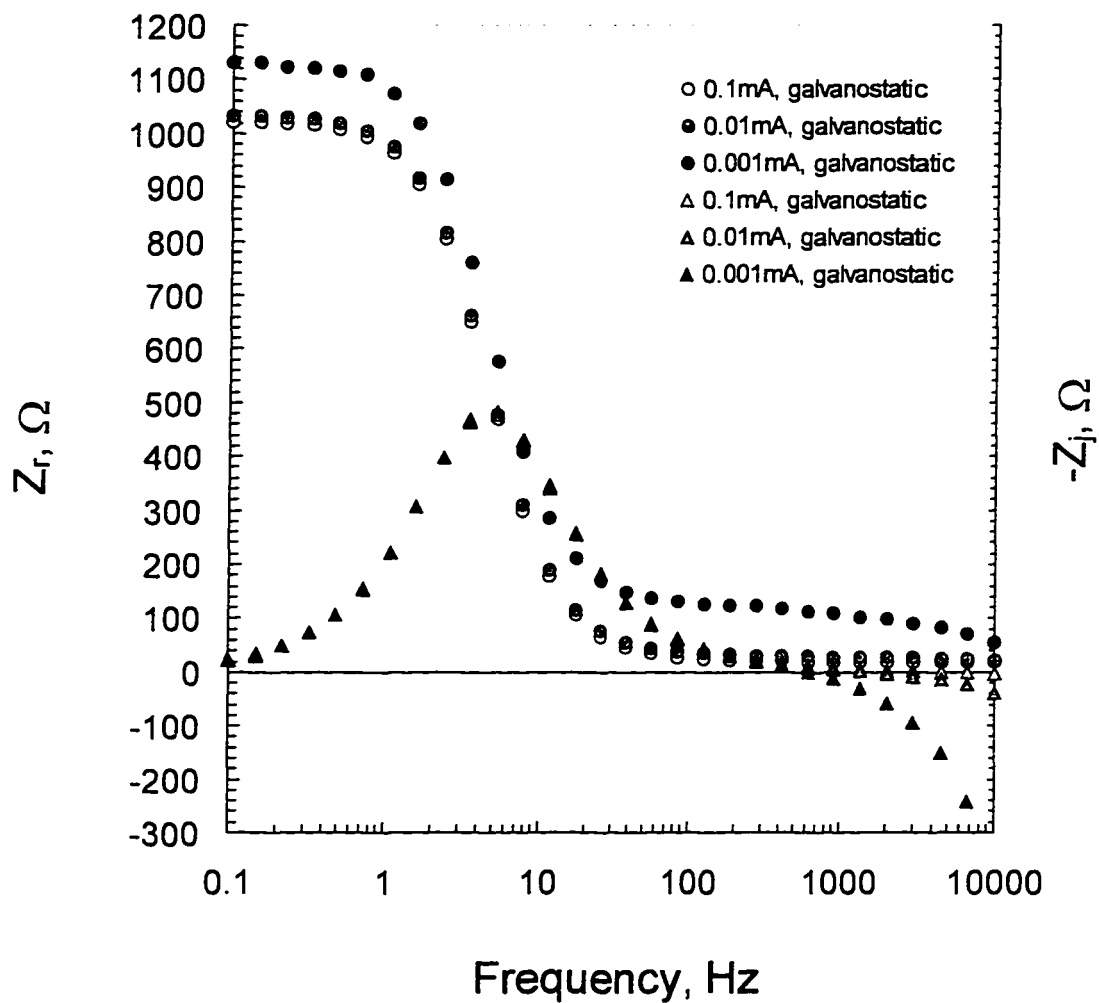
Figure 5.11: The real and imaginary components of the impedance as a function of frequency for test circuit Cell 2 comparing conventional galvanostatic, VAG, and potentiostatic techniques.

5.6 Experimental Studies

A comparison of techniques in Section 5.5 illustrated how the use of conventional impedance techniques under given conditions can result in erroneous data. This is true even for stable systems such as the electrical circuits used earlier to compare techniques. The key strength to the VAG technique is, however, the ability to collect consistent data even with difficult to measure systems such as those with transient baselines. The copper/synthetic sea water system has the potential for a changing baseline or corrosion potential with time, which can increase problems in the potentiostatic mode. Following are several examples of data collected on a copper / synthetic sea water system using potentiostatic, conventional galvanostatic, and VAG techniques. Impedance spectra collected with the conventional potentiostatic and variable amplitude galvanostatic modulation are presented in Figure 5.12. The three sequential variable amplitude galvanostatic scans show good reproducibility. The subsequent three conventional potentiostatic scans demonstrate significant differences, caused by imposition of an anodic bias as the system changed with time. The conventional potentiostatic data can be shown by the measurement model technique (Agarwal et al. 1992, Agarwal et al. 1993a/b, Agarwal 1994, Agarwal et al. 1995a/b) to be less consistent with the Kramers-Kronig relations than are the VAG data.

The large range of impedance values for this system makes it difficult if not impossible to collect impedance data using the conventional galvanostatic techniques. The problem is that, to retain an acceptable signal-to-noise ratio at high frequencies, the perturbation must be sufficiently large as to cause a non-linear response at low

frequencies. This problem is demonstrated in Figure 5.13, where spectra collected with the conventional galvanostatic, conventional potentiostatic, and variable amplitude galvanostatic modulation are presented. A fixed current amplitude of 0.01 mA yields serious errors at high frequency which have the appearance of a bias error rather than that of a stochastic noise. This is consistent with the results obtained using electrical circuits. The electrical circuits described in Section 5.5 were designed mimic the behavior of the copper corrosion cell. The comparison of the galvanostatic results to those obtained under VAG modulation, presented in Figures 5.14 and 5.15, reveal that the spectrum obtained under galvanostatic modulation with a 0.01 mA amplitude is in good agreement with the VAG results at low frequency, but shows large discrepancies at high frequency. The high frequency errors can be reduced (but not eliminated) by increasing the current perturbation amplitude to a value of 0.1 mA. Although this improves the data collected at high frequency, violation of linearity constraints are evident at low frequency.

Consistent with the results presented in Figure 5.12, comparison of the squares and triangles in Figure 5.13 reveals that the results obtained under conventional potentiostatic modulation are not as reproducible as those obtained under the VAG method. Slight drifts in the corrosion potential cause DC conditions which perturb the system and cause errors in the results.
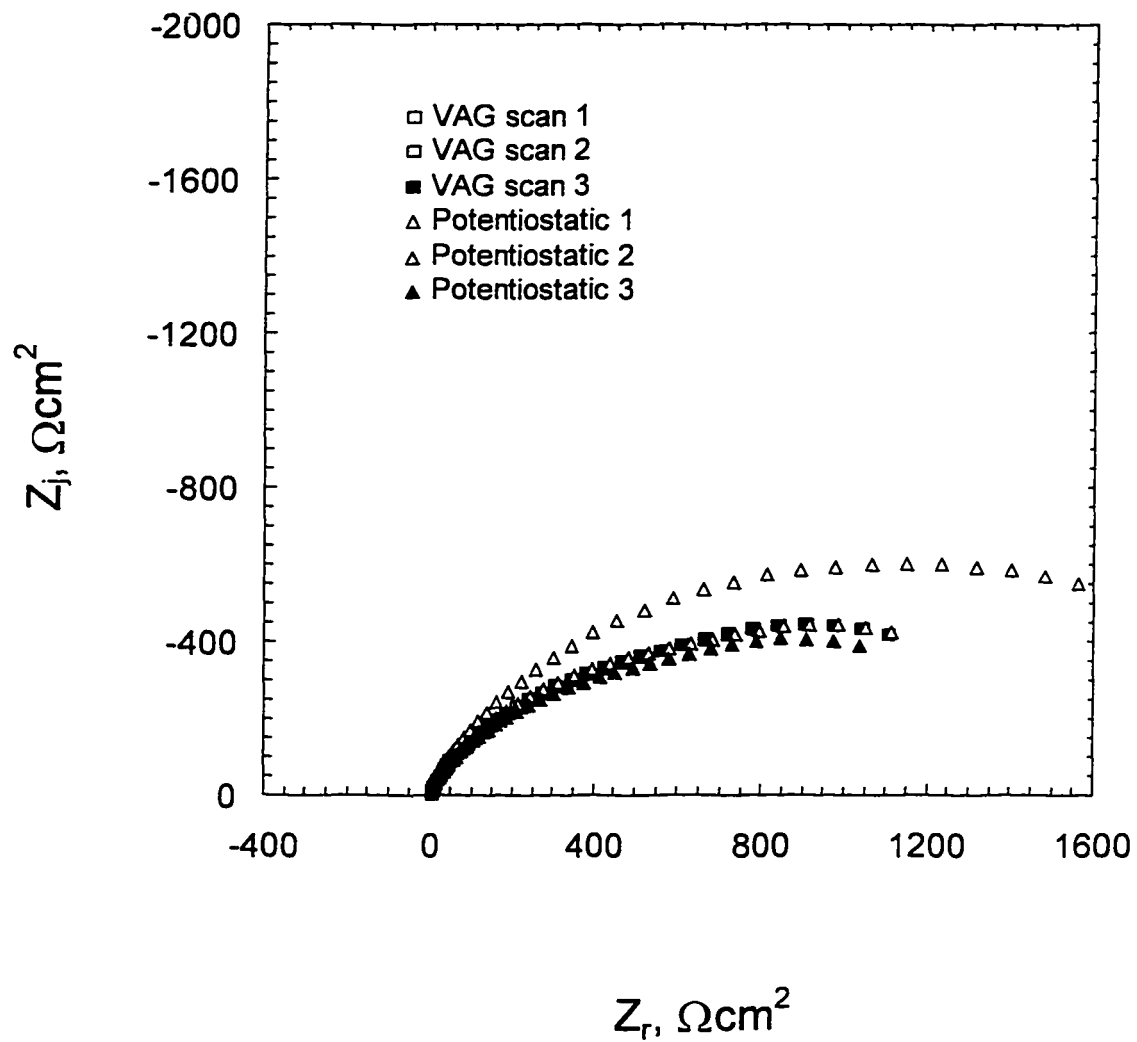
Figure 5.12: Impedance plane plot for 99.9% pure copper electrode immersed in ASTM
1141 synthetic sea water. Comparison between VAG and potentiostatic
techniques suggest that small changes in the system adversely effect
measurements made in the potentiostatic mode while measurements
conducted in the VAG mode are reproducible.
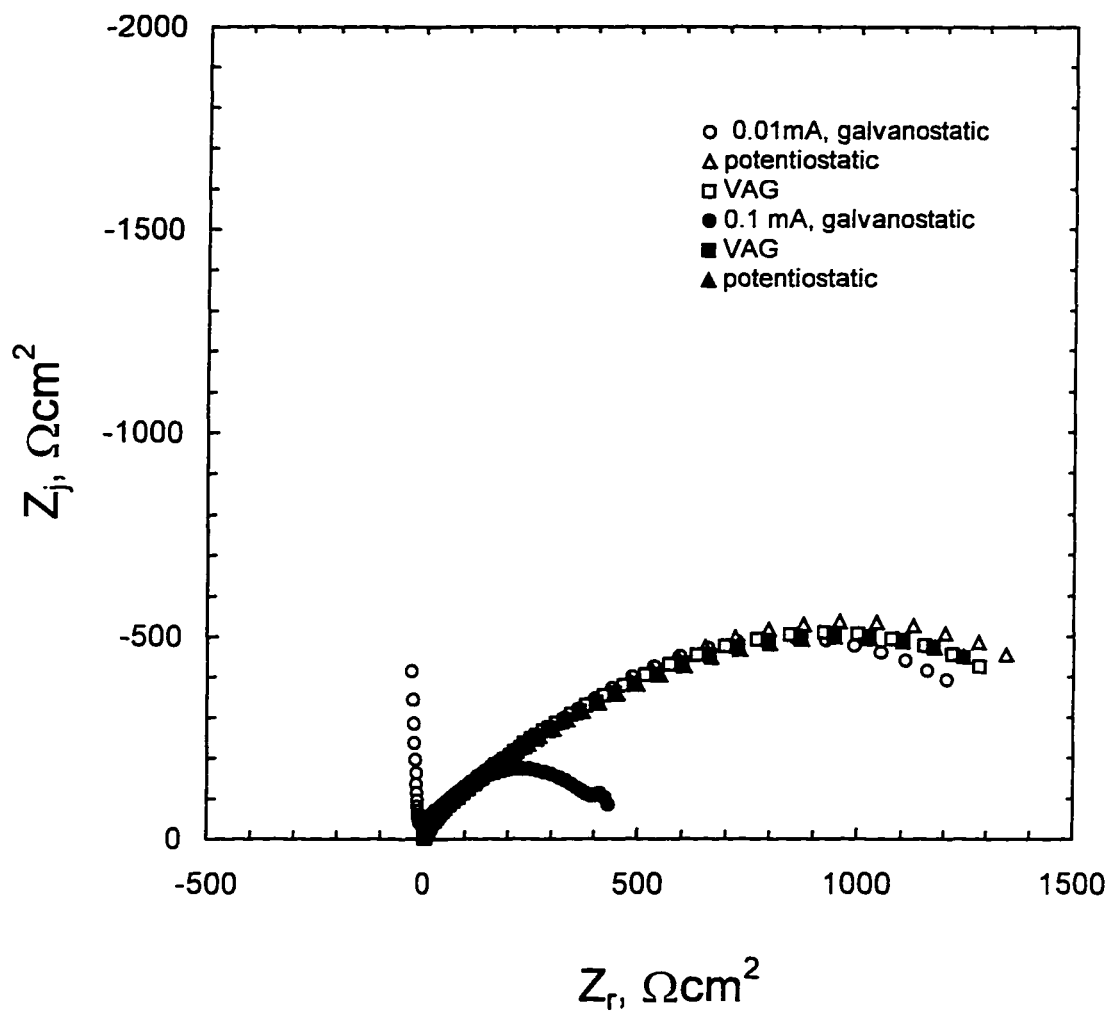
Figure 5.13: Impedance plane plot for 99.9% pure copper electrode immersed in ASTM
1141 synthetic sea water. Comparison between conventional fixed amplitude
galvanostatic, VAG, and potentiostatic techniques.
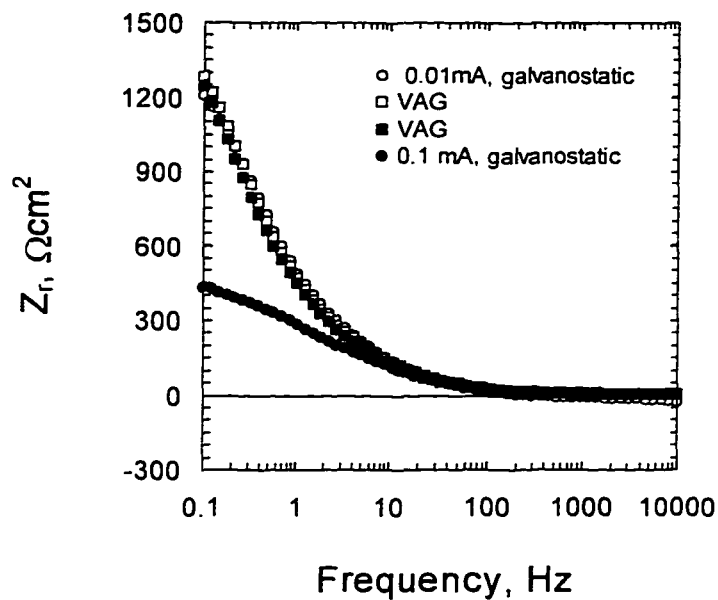
Figure 5.14: The real component of the impedance as a function of frequency for data presented in Figure 5.13. 99.9% copper immersed in synthetic sea water comparing conventional galvanostatic and VAG techniques.
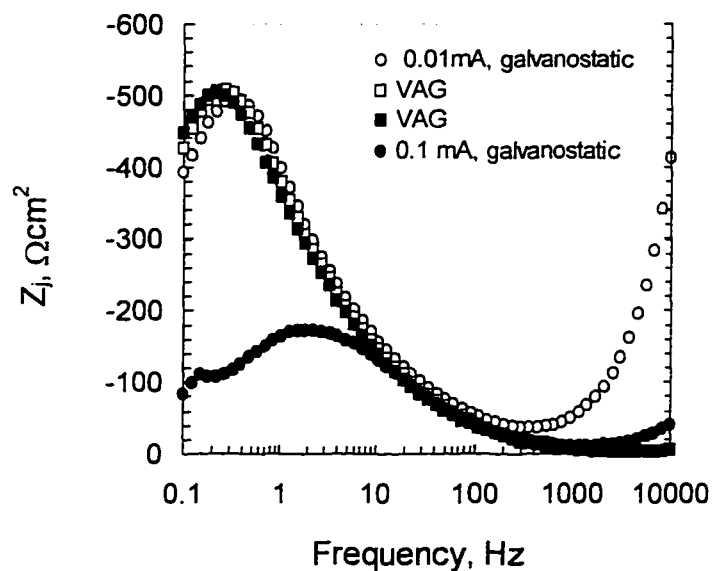
Figure 5.15: The imaginary component of the impedance as a function of frequency (see Figure 5.13) for 99.9% copper immersed in synthetic sea water comparing conventional galvanostatic and VAG techniques.

CHAPTER 6
RESULTS AND DISCUSSION

Results for experiments conducted on copper and copper nickel alloy electrodes are presented in this chapter. Electrochemical, X-ray photoelectron spectroscopy (XPS), and digital image data were collected on the samples. Copper and copper alloys were tested in a variety of environments, and the results were compared. Velocity, dissolved O_2 content, and pH were among the experimental parameters adjusted and the response to these changes is discussed in this section.

An important aspect of this work is the ability to predict the polarization impedance of the system without a process model. With the use of the measurement model, a value for the polarization impedance can be predicted. The measurement model can be used to calculate the standard error of the prediction using a Monte Carlo simulation. Section 6.1 of this chapter outlines the measurement model technique and describes the utility of this method in analyzing impedance spectra in the absence of a process model. The measurement model approach was applied to a variety of systems and the results of the analysis are presented in Sections 6.3 through 6.6.

Electrochemical techniques used consisted of electrochemical impedance spectroscopy, corrosion potential monitoring, and linear sweep voltammetry. Electrochemical techniques provide insight into the state of the electrode surface and also give information on the progress of film formation, modification, and/or removal. Sections 6.3, 6.4, and 6.6 include results of 99.9% pure copper samples investigated in

aerated and partially-aerated solutions with dissolved O_2 concentrations of 7.0 and 6.0 ppm, respectively. Aerated solutions were maintained by bubbling CO_2 scrubbed through the solution with an electric pump. The partially aerated solutions were allowed an air-liquid interface where O_2 and CO_2 could diffuse passively into solution. The response of small changes to the pH (8.06 to 8.24) in the partially-aerated solutions had little effect on the corrosion potential or the impedance response. Changes in the velocity, however, had an observable effect on the corrosion potential and a large effect on the impedance. In several experiments the impedance response was reduced by 50%. In well-aerated solutions, velocity changes had little effect on the corrosion potential or the impedance response. Results of experiments conducted on 70/30 copper/nickel alloys are presented in Section 6.5.

The XPS technique was used to investigate species present on the surface of the electrode after exposure to synthetic sea water, and digital imaging was used to maintain a record of the condition of the surface throughout a run and to provide visual indications of shear-induced corrosion.

All the electrochemical data collected during this work resulted from the immersion of an electrode in ASTM 1141 synthetic sea water at 25° C. Potential measurements were all conducted relative to a saturated calomel electrode (SCE). The jet velocities investigated ranged from 0.0 to 6.2 m/s at the jet nozzle. Aerated and partially aerated solutions were examined and results of each were compared. The electrochemical impedance spectroscopy technique used for this work was the VAG technique with a few exceptions as noted. The copper-sea water system has the potential for a changing baseline or corrosion potential which will accentuate problems in the potentiostatic mode.

6.1 The Measurement Model Approach

The differences in surface reactivity can be quantified, even in the absence of a detailed mathematical model for the corrosion of copper, through use of the measurement model approach. This quantification follows three steps:

1. Identification of the frequency-dependent error structure following the method presented by Agarwal *et al.* (1992)

2. Identification of the portion of the spectrum that is consistent with the Kramers-Kronig relations following the method presented by Agarwal *et al.* (1993a). High frequency data were found to be corrupted by instrumental artifacts. The low frequency data were typically found to be consistent with the Kramers-Kronig relations except for data collected early in the experiment where the system was changing rapidly.

3. Regression of the measurement model to the part of the spectrum found to be consistent with the Kramers-Kronig relations using the error structure found in part 1 above to weight the regression.

The regressed parameter values were used to extrapolate to the zero frequency limit, and Monte Carlo simulations were performed using the standard deviations of the regressed parameters to estimate the confidence interval for the extrapolation. The polarization impedance was obtained by subtracting the regressed solution resistance from the extrapolated zero-frequency value. The polarization impedance supplies a good indication of how well a surface is protected, i.e. the corrosion resistance of the surface. A knowledge of the predicted polarization impedance through the use of the measurement model technique provides a powerful tool in materials selection for real-

world applications and can be equally beneficial in the field for determining *in situ* materials performance.

6.2 Linear Sweep Voltammetry

Linear sweep voltammetry was used to investigate the formation of films on a copper electrode under quiescent conditions. An aerated solution of synthetic sea water of pH $\approx$ 8.2 and 25°C was used as the electrolyte. Figure 6.1 shows the current as a function of potential, sweeping from a cathodic potential of -1.0 volts to the anodic potential of 1.0 volts. Figure 6.1 displays three linear sweeps of different rates ranging from 1.0 mV/s to 13.3 mV/s. The different sweep rates do not overlap indicating that the system was not at an equilibrium state during the sweeps. This also suggests a mass transfer limited condition because the currents were lower for the initial portion of the sweep. The corrosion potential for a polished copper electrode in synthetic sea water is approximately -300 mV versus SCE. The application of the initial cathodic potential shifted the potential value corresponding to the zero current condition to lower values. This shift is more significant at the faster sweep rate and at the slower rates, the zero current potential approaches the equilibrium value. The anodic portion of the curve exhibits a higher current for the 13.3 mV/s sweep which suggests that a thicker protective film had formed during the 1.0 and 2.0 mV/s sweeps (Charrière 1997).

The four plateaus apparent in each of the sweeps presented in Figure 6.1 represent regions where current was limited by mass transfer through surface films which increased the impedance. The dotted line for the 1.0 mV/s has an inflection point where the current drops at approximately -400 mV versus SCE. This suggests that a film formed protecting

the surface. The increasing potential eventually overrides the protective capability of the film.

Presented in Figure 6.2 is a cyclic voltammogram with a sweep rate of 66 mV/s sweeping from -1.0 volts to 1.0 volts and back to -1.0 volts. The difference between the forward curve and the reverse curve suggests that the sweep rate was too rapid to allow the system to equilibrate during one or both sweep directions.

Potentiostatic regulation of 99.9% pure copper electrode in flowing (≈ 0.1 m/s) aerated synthetic sea water is displayed in Figure 6.3. Low velocities were used for these runs for the purpose of maintaining uniform mass transfer, while minimizing the shear at the electrode surface. Potentials were maintained at constant values of 100, 200, and 400 mV for the duration of each run. All traces indicated that the formation of a salt film resulted in a decrease in the current. An incident of shear-induced removal of a salt film was observed for the 200 mV (SCE) experiment. The film completely covered the electrode surface and stabilized which is evident to the right of the second vertical dotted line where the current remains constant. The film became unstable at time 160 seconds, and removal of the film resulted in an increase in current. The film completely separated from the surface at time 320 seconds where an abrupt increase in the current is visible in the trace.

Video images corresponding to the 200 mV (SCE) trace are presented in Figures 6.4 and 6.5. In an impinging jet apparatus with flow, salt films will form on the periphery of a copper disk electrode and move inward. Visual examination or digital image analysis can be used to determine the location of the leading edge of the salt film. These films appear as rings or halos on the electrode surface. Conversely, salt films dissolve from the

interior of the disk towards the outside. Figures 6.4 and 6.5 present images illustrating the formation and dissolution of salt films on the surface of a copper electrode (order of images is from left to right). The 200 mV (SCE) potential was applied and the progression of the formation of the film can be observed in Figure 6.4. A plausible explanation of the images in Figure 6.4 is that an anodic potential was applied resulting in the formation of salt films. The first film, yellow in color can be seen in the first image of Figure 6.4 and is pointed out by the arrow. The second film, which was more visible in the second and third images with a darker, almost purple hue. This film gave way to a third film, which can be seen near the periphery of the last image. Three possible scenarios may have taken place. The first is that three different films formed and became unstable and dissolved resulting in the formation of the other films. The second situation involves three films forming at different times and being covered by the film which formed next, and the third scenario is that one or more of the color changes is due to a change in thickness of the film.

Removal of the salt film can be observed in Figure 6.5. The first image is of a almost fully film-covered electrode, the film being yellowish orange in color. As time passed the film lightened and began to break off in parts starting at the edge of the disk due to a higher shear stress. The lightening of the film suggests a thinning effect, however, the absence of the dark film suggests the presence of two different films. The dark film was less stable than the orange-yellow film with a short residence time on the disk at the given potential. A significant increase in the current (from 12 to 15 mA) was seen immediately following the loss of the large portion of film pointed out in the second and third images by arrow (Charrière 1997). The salt films on the electrode surface were

not firmly adhered to the surface and were susceptible to shear stresses. The shear was highest at the periphery of the disk resulting in the removal of the film on the outside of the disk first. This work demonstrated the capability of the impinging jet video imaging system to detect and monitor the radial dependence of film growth and dissolution, as well as shear induced removal of films.
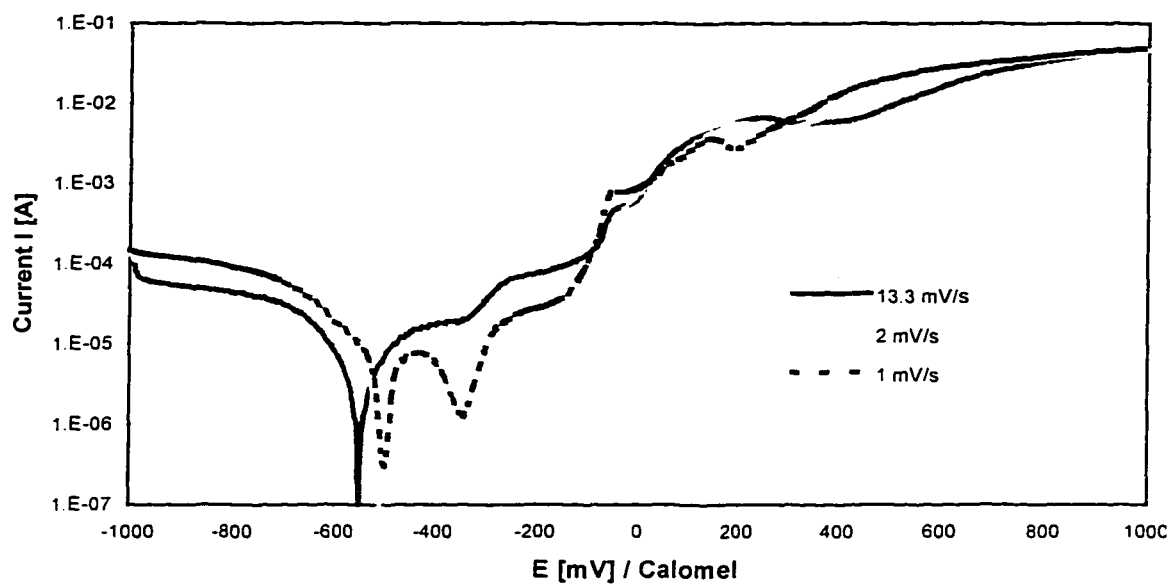
Figure 6.1: Linear sweep voltammogram at three different sweep rates. Applied potential versus resulting current (Charrière 1997). Plateau areas indicate formation of salt films. Slower sweep rates allow for more complete formation of films resulting in a decrease in current.
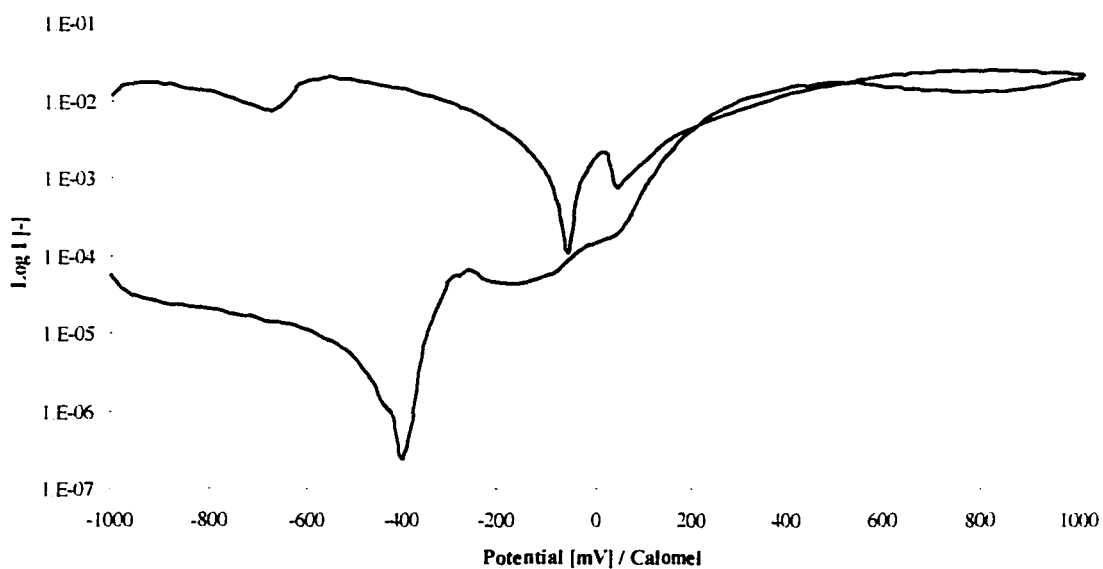
Figure 6.2: Cyclic voltammogram with a rate of 66 mV/s (Charrière 1997). Plateau areas indicate the formation and dissolution of films.
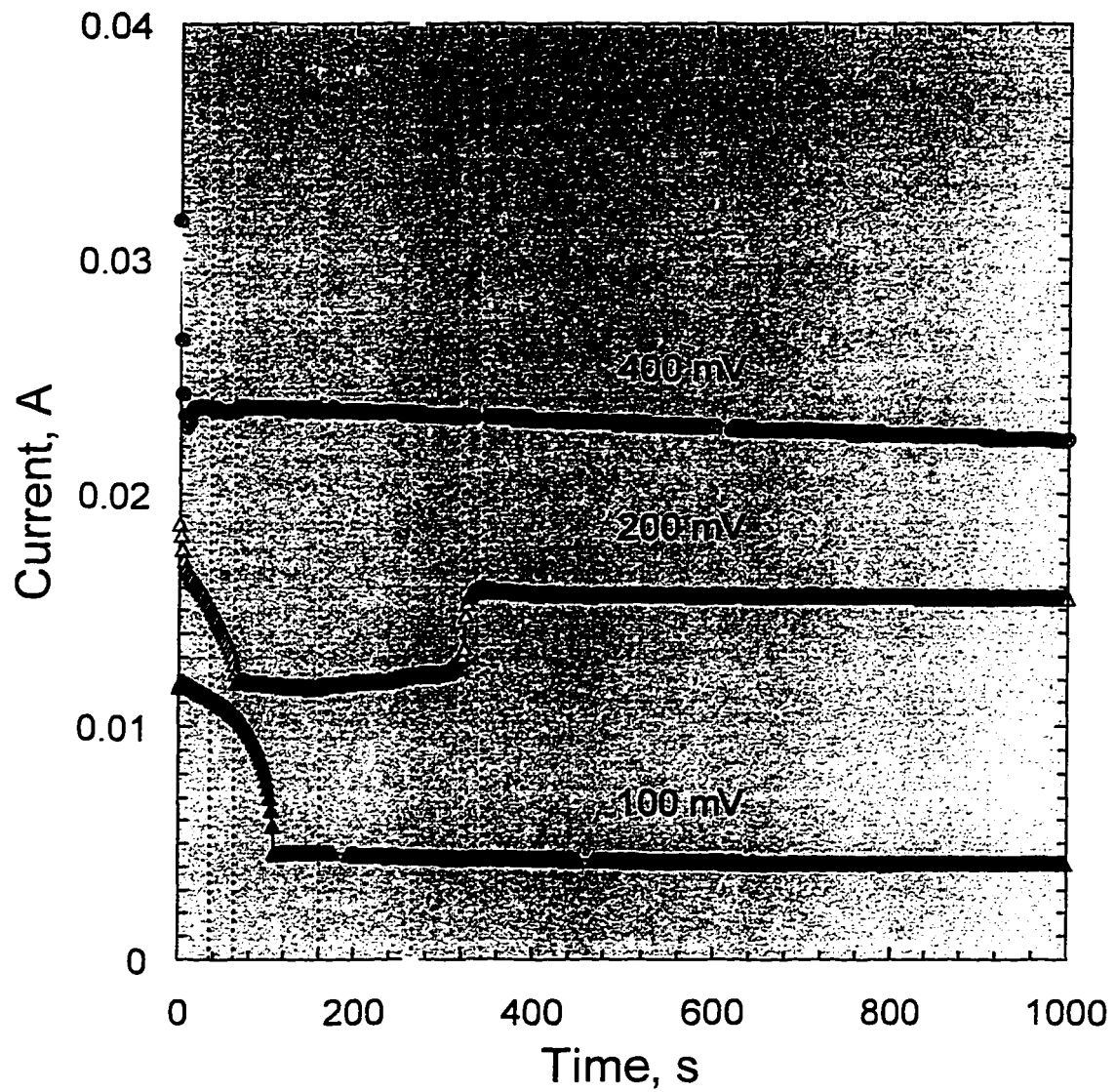
Figure 6.3: Potential time traces for 99.9% pure copper in aerated synthetic sea water. Velocity ($\approx$ 0.1 m/s) maintained at low value primarily to ensure uniform mass transfer to the surface and removal of corrosion produces not tightly adhered to the surface.
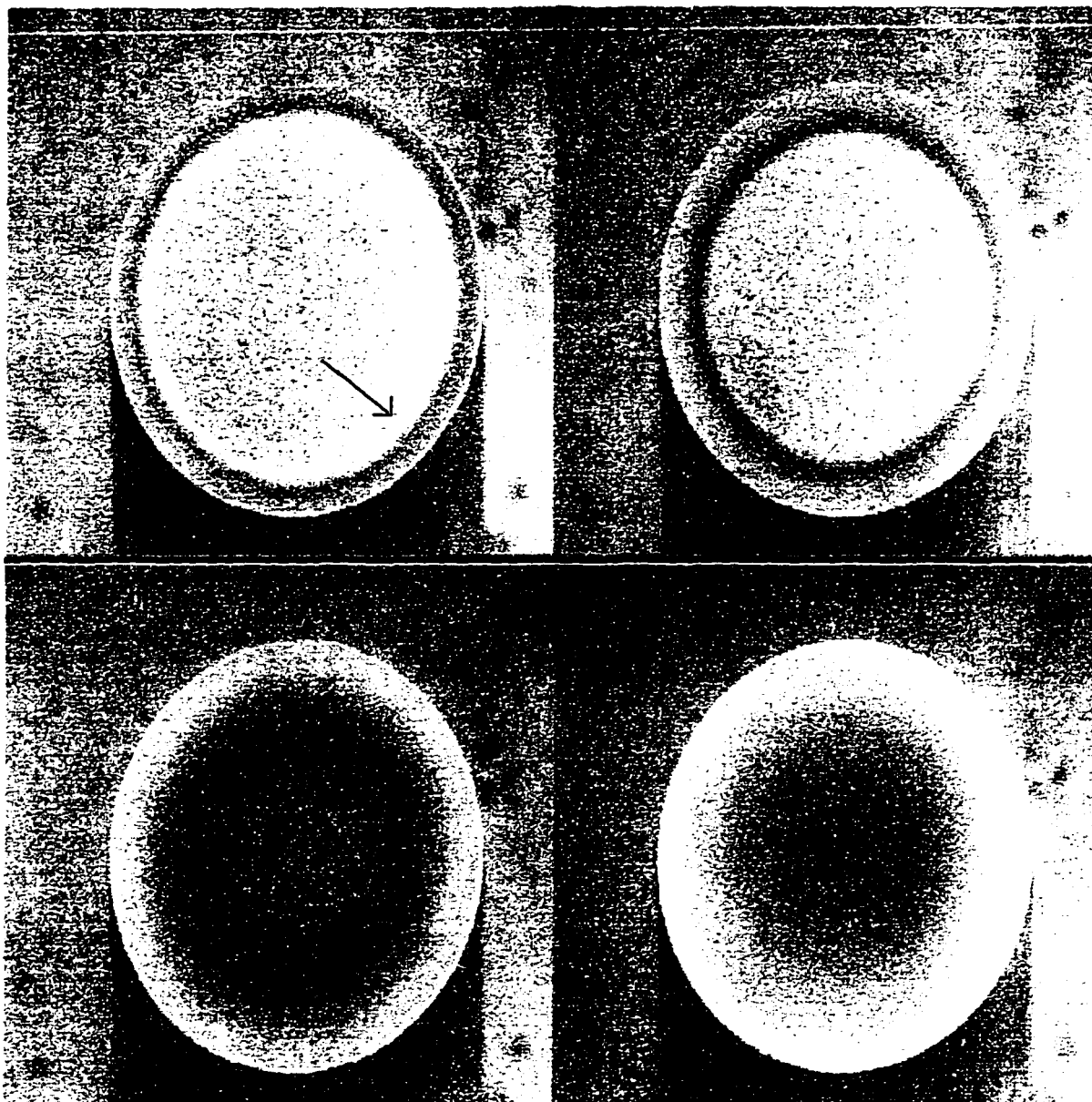
Figure 6.4: Progression of a film growing during potentiostatic control at constant 200.0 mV. Images progress from left to right, total elapsed time = 1000 seconds (Charrière 1997). Films originate at the periphery and grow towards the center of electrode.
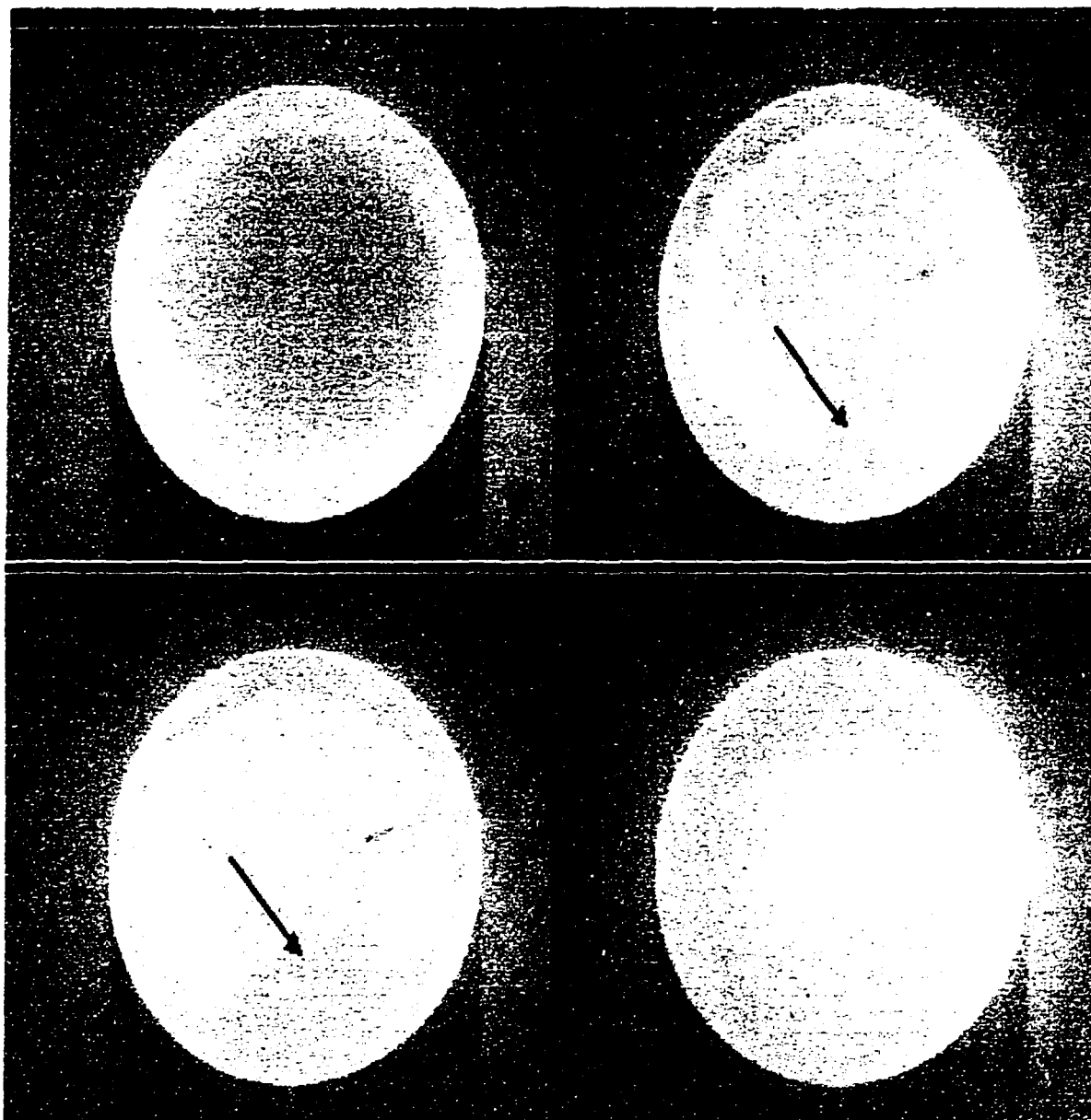
Figure 6.5: Progression of a film removal from electrode surface during potentiostatic control at constant 200.0 mV. Images progress left to right, total elapsed time = 1000 seconds (Charrière 1997). Film became unstable and was removed by shear beginning at the outer edge because of a higher shear stress.

6.3 Copper in Partially-Aerated Electrolyte: Part 1

The time frame for the experiment presented here spans 33 days. The resulting corrosion potential data, impedance data, and digital images, are identified by the time from the start of the experiment. Changes in the jet velocity and adjustments in the pH were conducted during the experiment, and the influence of these changes on the corrosion potential, impedance, and surface appearance were investigated. A time line for the experiment is presented in Table 6.1.

The working electrode was 99.9% pure copper immersed in synthetic sea water. The corrosion potential is presented in Figure 6.6 as a function of time for the entire 33 day period. The initial corrosion potential behavior of all the copper and copper/nickel alloys studied for this work was similar in the sense that the corrosion potential, immediately after submersion, increased rapidly during the first few hours (Agarwal 1993a). For the freely corroding systems investigated in this work, the corrosion potential became more positive from the initial measurement, and the rate of change slowed until a constant value was reached. The difference between the initial value and the constant value was as much as 70 mV.

The jet velocity for the first seven days was controlled at 1 m/s and the pH was 8.05. Corrosion potential data for the first seven days of the experiment are presented in Figure 6.11. A pseudo-steady-state value of -283 mV for the corrosion potential was reached after approximately 48 hours, and this value fluctuated by less than 2 mV over the next five days. Impedance data collected over the first five hours of this run are displayed in Figure 6.12. The common trend for the impedance collected over time was

that of an initial decrease in the impedance followed by an increase to a pseudo steady state value. This steady-state value was typically achieved after several days. The extrapolated values for the polarization impedance are presented in Figure 6.13 for scans taken in the first 5 hours. The polarization impedance decreased with time in the initial seven hours of an experiment. The extrapolated value for the polarization impedance was used here to indicate the level to which the surface is protected.

The velocity was reduced to zero after seven days and was kept quiescent for 16 days. Flow was resumed at 1.0 m/s and a series of impedance scans were conducted to investigate changes in the electrode reactivity over the quiescent period. Figure 6.14 displays impedance scans taken before and after the 16 day quiescent period. Video images of the copper surface revealed the presence of a thick film. Comparison of impedance data sets at time = 158 and 551 hours revealed an increase in the impedance over the period of time the solution was stagnant. Figures 6.7 and 6.8 show images of the electrode before and directly after the quiescent period. One can observe a precipitate on the electrode surface in Figure 6.8 which was providing additional protection of the surface but was not strongly adhered. The blue green color suggests the presents of cuprous chloride dihydrate (taken from Table 2.4). The first scan after the quiescent period, presented in Figure 6.14 (shaded circles), was collected in the potentiostatic mode to ensure potential perturbation of 10 mV while all the other scans were collected in the VAG mode. A slight discrepancy between potentiostatic and galvanostatic data is attributed to the presence of a DC component generated by a difference in the applied bias and the corrosion potential baseline, a necessary procedure in the potentiostatic mode.

Data set 556.6 (triangles) was collected after an instrumentation malfunction caused a large cathodic potential on the order of -1.3 volts to be applied to the system for approximately 2 minutes, resulting in the evolution of hydrogen from the electrode surface and removal of films. The impedance values after the potential excursion were reduced by a factor of 10 as compared to the impedance scans prior to the cathodic applied potential. A noticeable change in the appearance of the electrode surface was evident, and the presence of hydrogen bubbles on the surface was observed in the video images (refer to Figure 6.9). The surface film was disrupted, and portions of the film were removed, leaving bare copper sites visible on the surface of the electrode. The decrease in the impedance observed after the potential disturbance suggests the removal of a protective film, and this hypothesis is supported by the digital images captured before and after the disturbance.

Approximately 25 minutes after the potential disturbance, flow was resumed. Air that had accumulated in the lines was removed, and the jet velocity was adjusted to 1 m/s. The changes in the appearance of the electrode surface can be viewed in Figure 6.10 which shows that both the blue-green precipitate and the hydrogen gas bubbles had been swept away by fluid movement. Comparison between Figures 6.8 and 6.10 confirms the removal of the brown oxide layer that had formed on the electrode and presence of bare copper sites after the cathodic potential application.

Electrochemical data collection resumed 25 minutes after flow was started. The corrosion potential data collected at the conclusion of the quiescent period and after flow was resumed is presented in Figure 6.15. The triangles in Figure 6.15 represent corrosion potential measurements taken immediately preceding impedance scans while the

diamonds represent measurements taken immediately following these same scans. These data were collected in the absence of flow. The pre-scan potential measurement are reasonably constant at about -231mV, while the post-scan measurement showed more variation due to the slight disturbances to the system caused by the measurement. After potential disturbance and the flow was resumed the corrosion potential data are displayed as circles in Figure 6.15. The outlying points around -340mV are attributed to the application of the -1.3 volts previously discussed. As can be seen from the data, the cathodic applied potential dramatically influenced the impedance response, corrosion potential, and visual appearance of the electrode surface.

The corrosion potential returned to the value before the potential disturbance after a period of 120 hours and remained constant for several days. A small adjustment of pH by addition of NaOH had no discernible effect on the corrosion potential. The corrosion potential changed abruptly, however, following an increase in jet velocities of 1.0 to 6.75 m/s. The values for the shear stress corresponding to these velocities at a radial position of $r/r_0 = 0.8$ are 14.5 and 195 N/m^2, respectively.

Impedance data collected during this leg of the experiment are presented in Figure 6.16. It can be observed from Figure 6.16 that the impedance increased steadily after the potential disturbance which corresponds to a decrease in reactivity as the protective films reestablished. The value for the impedance was approaching a constant value after an additional 150 hours. A pH modification from 8.05 to 8.24 had no discernible effect on the impedance response when plotted in impedance plane format, however, the influence of a change in jet velocity from 1.0 to 6.75 m/s on the impedance of the electrode is easily seen in Figure 6.16.

The polarization impedances corresponding to impedance data displayed in Figure 6.16 are shown in Figure 6.17 as a function of time. The general trend of the impedance increasing over time can be observed. The sensitivity of the impedance responses to changes in flow rate and pH can seen in Figure 6.16. The polarization impedance and the associated confidence intervals given in Figure 6.17 were obtained by the measurement model concept developed in this group as part of the infrastructure for the erosion-corrosion experiments. The impedance response was found to be slightly sensitive to the small adjustment of pH, and also shows a large increase in the reactivity of the surface following the increase in jet velocity.

The video micrographs shown in Figures 6.18 through 6.21 give insight on the evolution of the electrode surface. The polished copper electrode surface for the first experiment discussed here is presented in Figure 6.18. This micrograph corresponds to a time immediately after submersion in solution. Polishing marks not evident out of solution by the naked eye can be observed in the micrograph. These polishing flaws were left by the 0.05 micron alumina powder used in the final stage of wet polishing. An evolution of the surface from the initial features can be seen in Figure 6.19 where a uniform film was observable on the surface. After the system recovered from the potential excursion, a similar uniform film was observed (Figure 6.21). The increase in jet velocity resulted in a large reduction in the polarization impedance, however a uniform film was still present on the electrode surface (Figure 6.21). The observable increase in the sharpness of Figure 6.21 as compared to Figure 6.20 was attributed to removal of a loosely adhered salt film. No ring-shaped features were evident in the

micrographs suggesting that the salt film was quickly removed when the velocity changed and that the oxide layer below was still intact.

Table 6.1: Time line highlighting major events for the experiment presented in Figures 6.5 - 6.16.

Time, h	Event
0	experiment start, u=1m/s, pH = 8.05, Figure 16a image captured
169	flow suspended, u=0 m/s, pH = 8.05, Figure 16b image captured
550-556	conduct impedance and corrosion potential measurements in quiescent solution, pH = 8.13
556	applied potential of -1.3 volts,
557	flow initiated, u=1m/s, Figure 13 image captured
557	resumed standard collection of E_{corr} and Z
671	Figure 16c image captured
718	pH change from 8.06 to 8.24
742	velocity change from 1m/s to 6.8 m/s
814	Figure 17d image captured
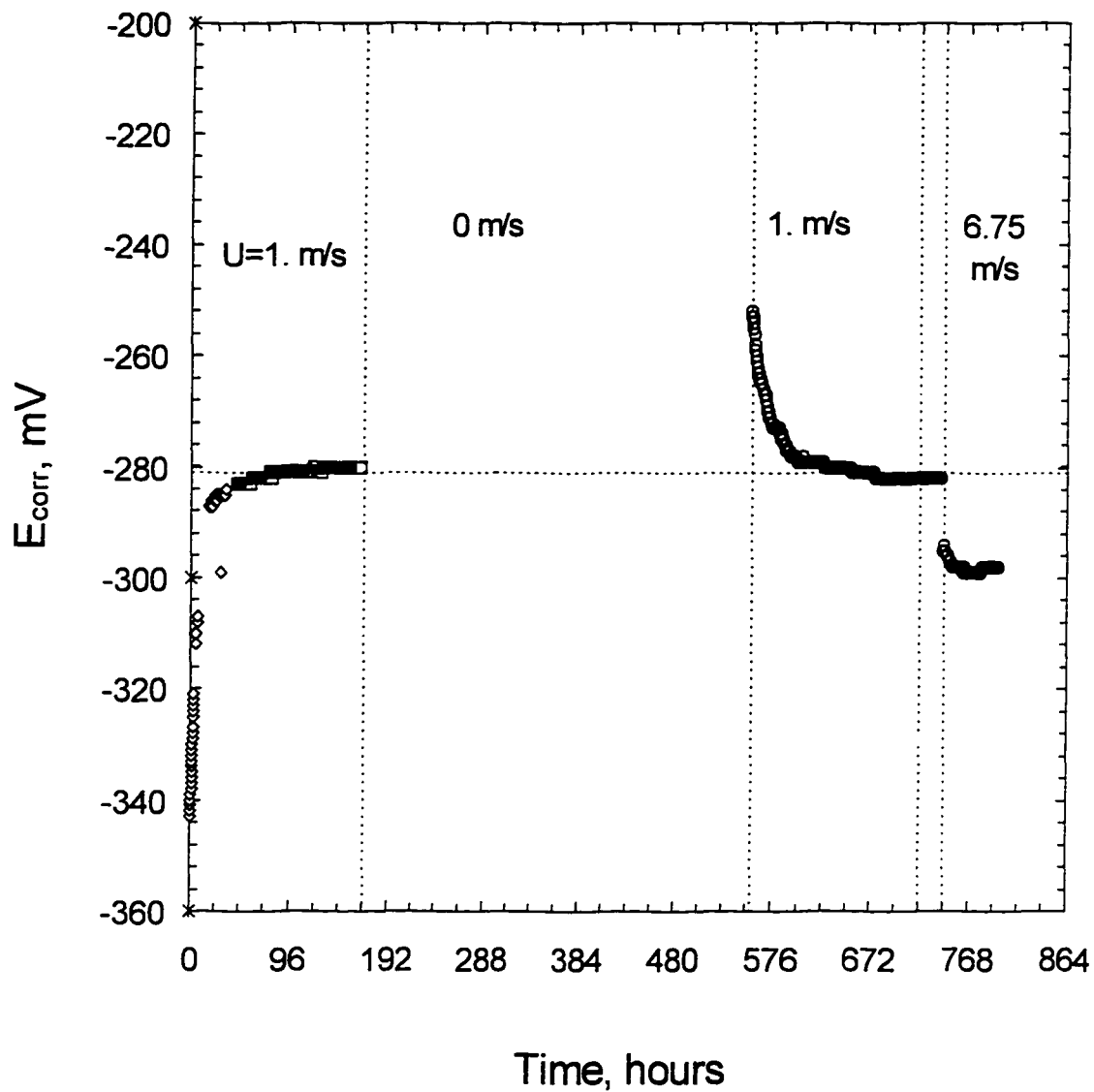
Figure 6.6: Corrosion potential of 99.9% Cu measured as a function of time for a period of 33 days. Electrode remained in stagnant fluid from t=190 to 550 hours. A cathodic potential was applied at t=556 hours and flow was resumed at t=557 hours.
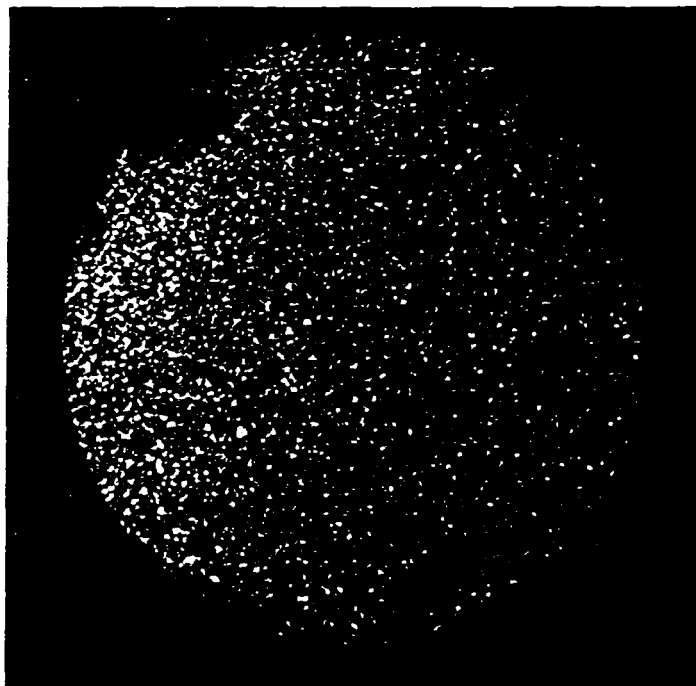
Figure 6.7: Video micrograph obtained for the experiment described in Table 6.1. Pure copper in non-aerated electrolyte before quiescent period, time = 190 hours.
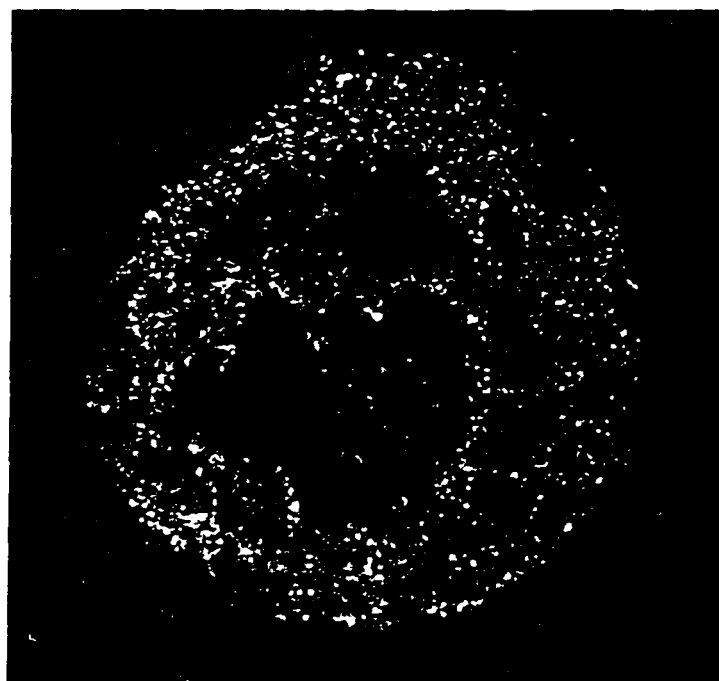
Figure 6.8: Video micrograph obtained for the experiment described in Table 6.1. Pure copper in non-aerated electrolyte after quiescent period, time = 555 hours.
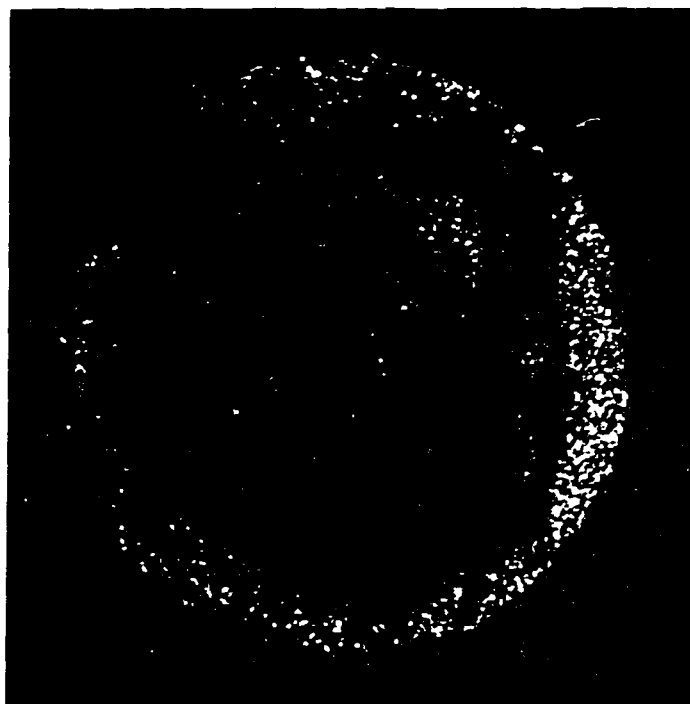
Figure 6.9: Video micrograph obtained for the experiment described in Table 6.1. Pure copper in non-aerated electrolyte after quiescent period and potential disturbance. Hydrogen bubbles and bare copper visible, time = 556 hours.
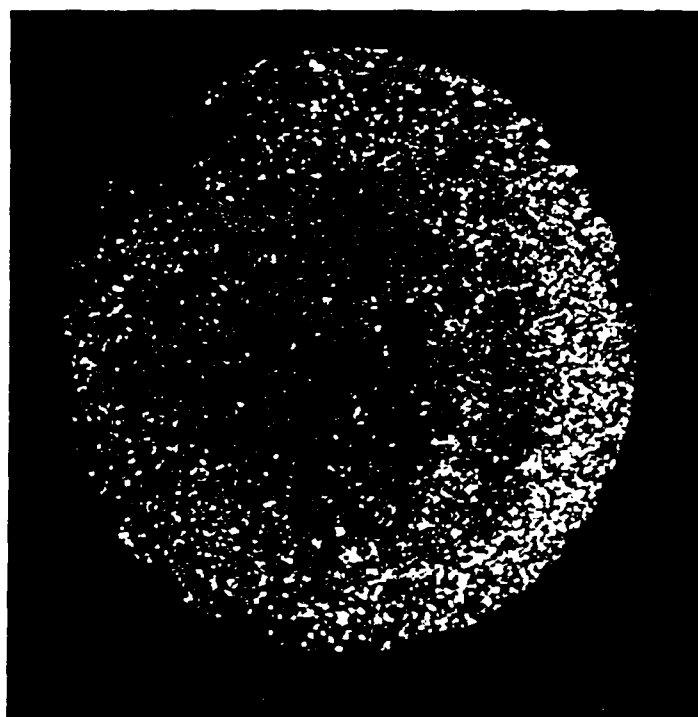
Figure 6.10: Pure copper in non-aerated electrolyte after flow resumption, time = 558 hours.
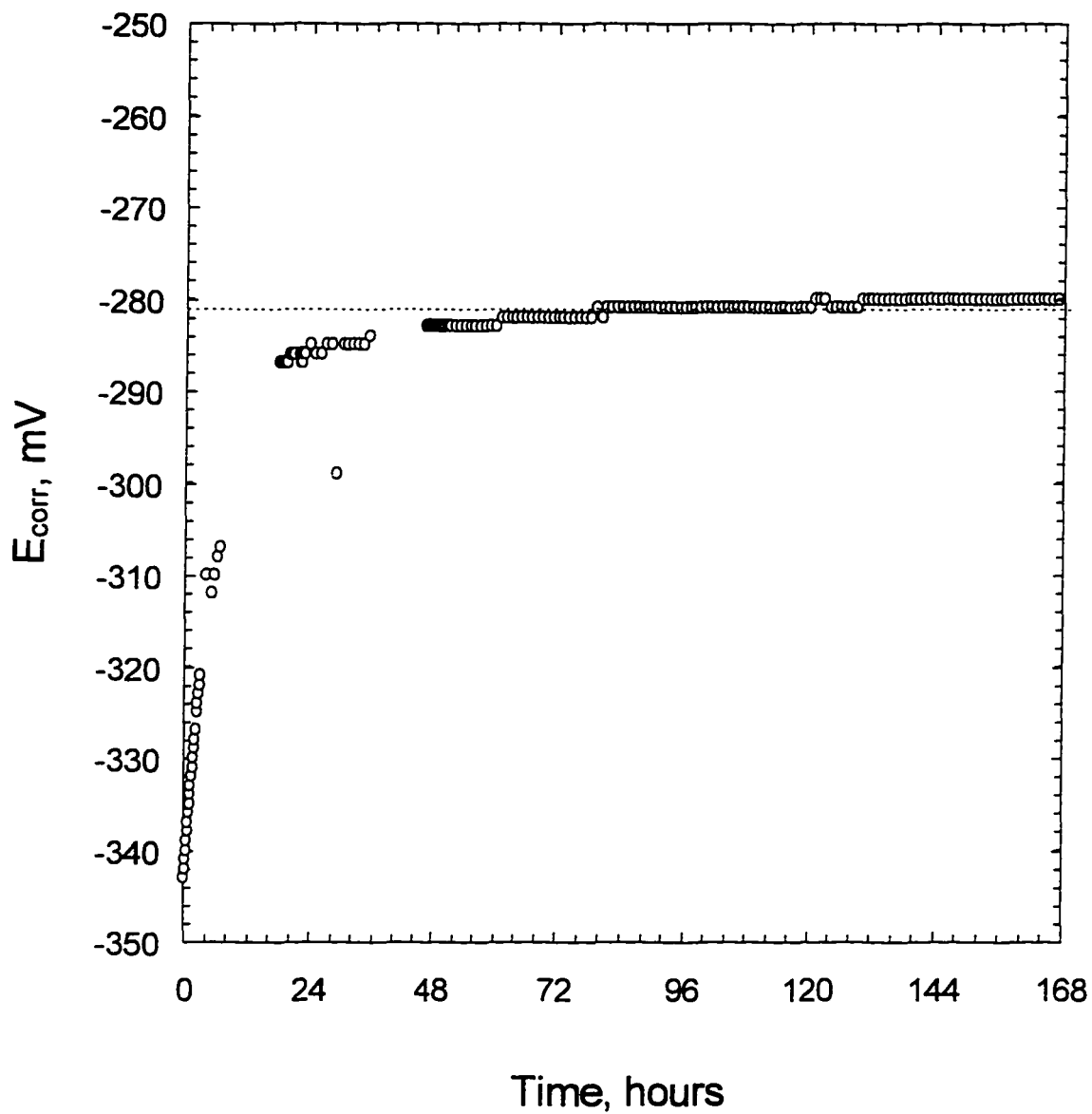
Figure 6.11 An expanded time scale for the Corrosion potential data presented in Figure 6.6. First seven days of immersion.
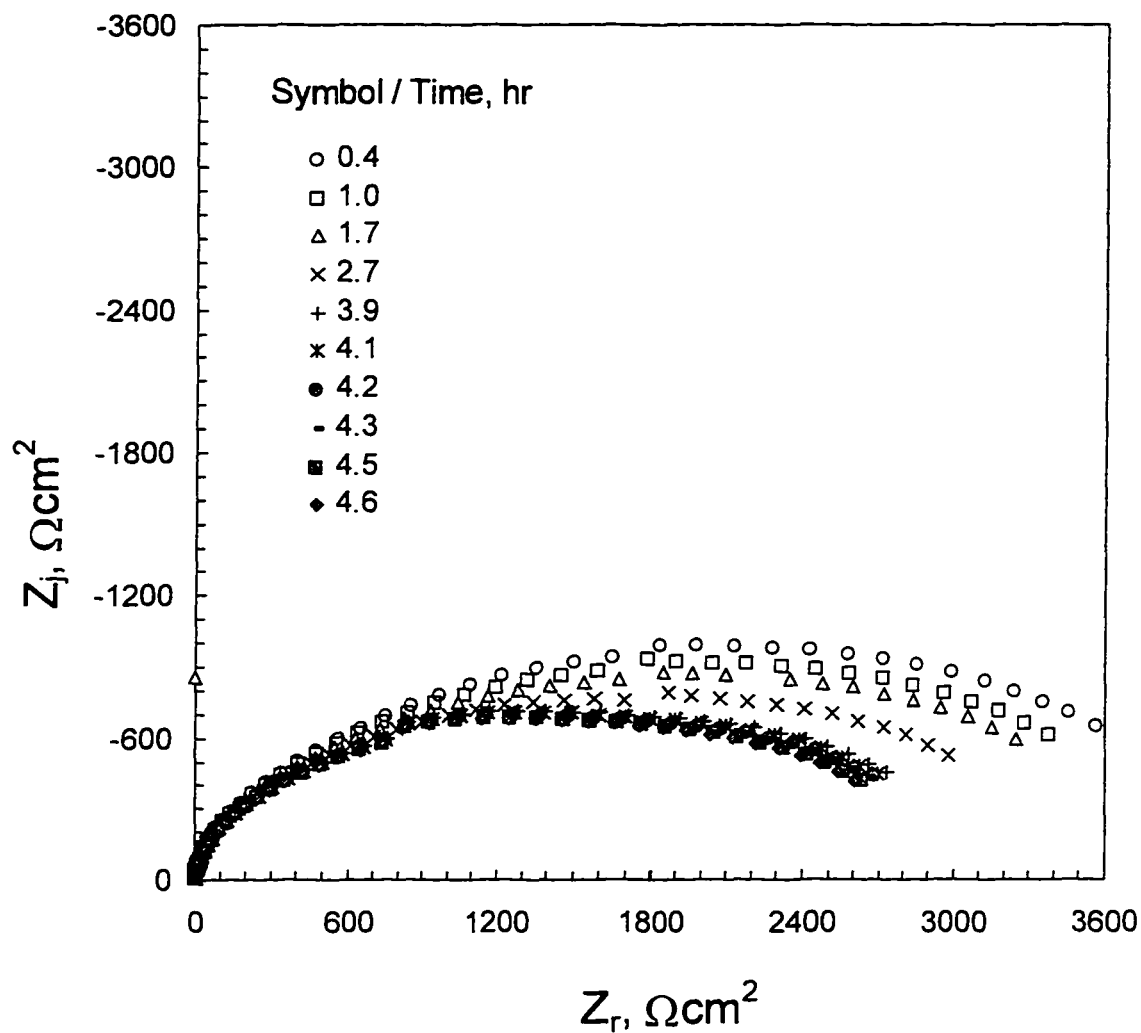
Figure 6.12: Impedance data for 99.9% Cu taken during the first five hours of submersion. The general trend was that the polarization impedance decreased for approximately seven hours after submersion and then increased to a steady state value.
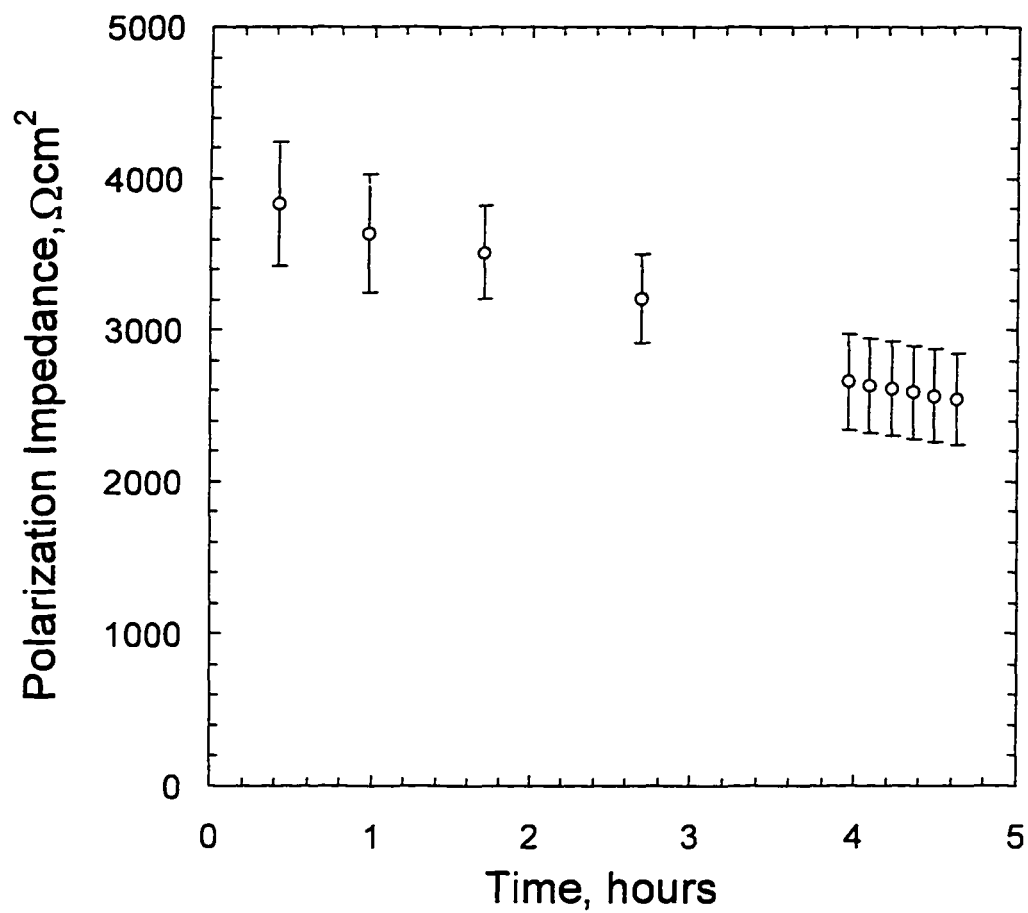
Figure 6.13: Polarization impedance corresponding to impedance scans shown in Figure 6.12. Values and associated error predicted through the use of a measurement model.
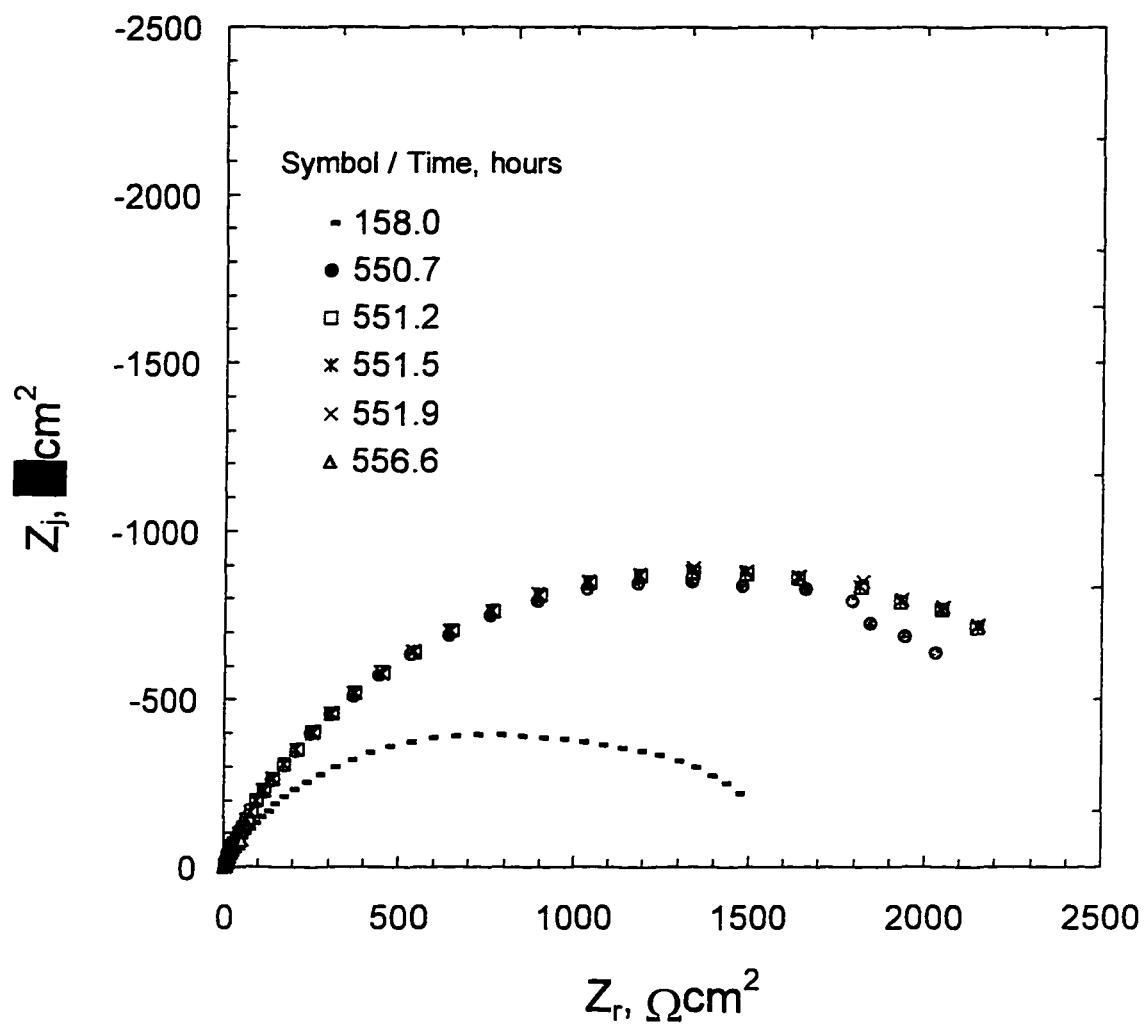
Figure 6.14: Impedance scans for 99.9% Cu before and at the end of the 16 day quiescent period. Velocity for time=158 spectra was 1.0 m/s, all other scans the velocity was 0.0 m/s
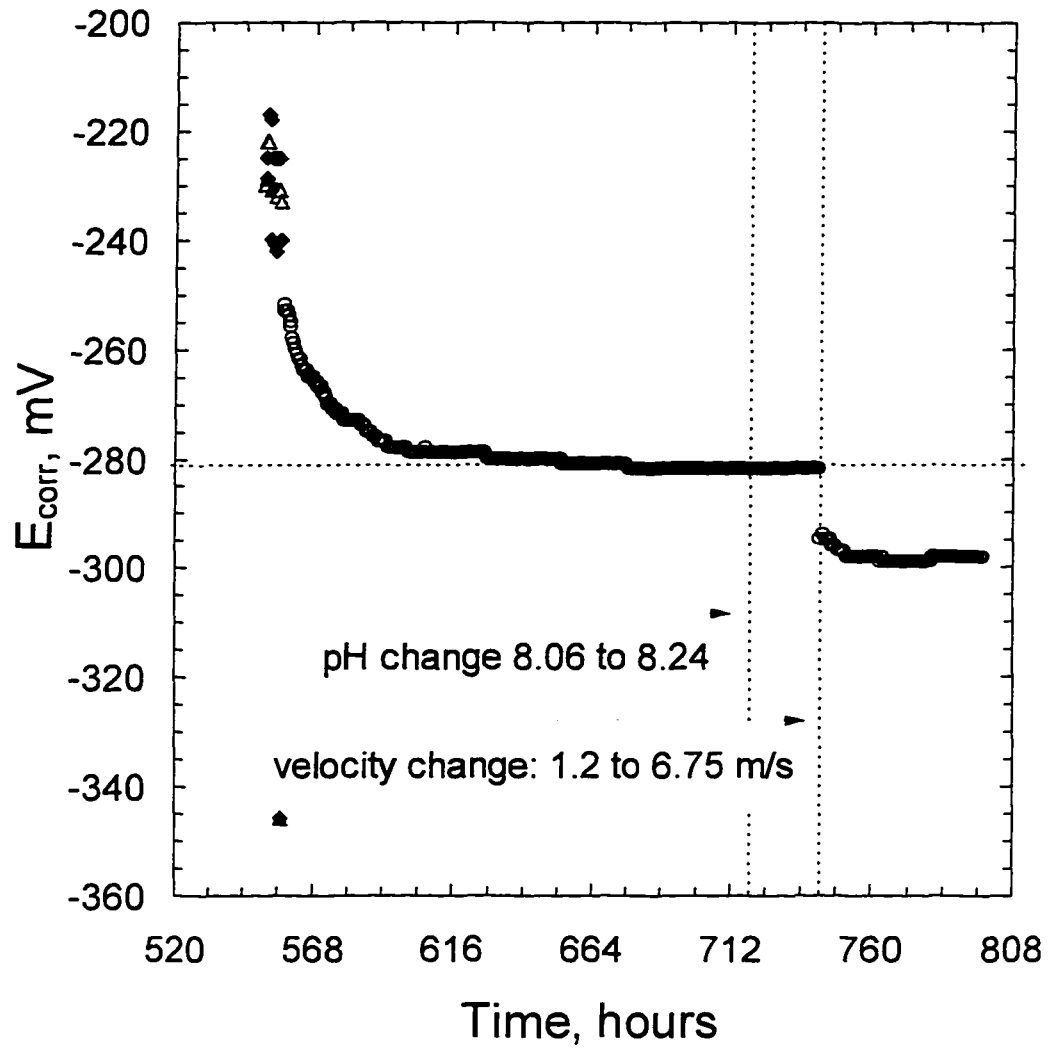
Figure 6.15: Copper electrode corrosion potential as a function of time. Cathodic potential applied (-1.3 V) before start of experiment. A change in the pH showed no effect in corrosion potential while a velocity change clearly affected the corrosion potential for a non-aerated solution.
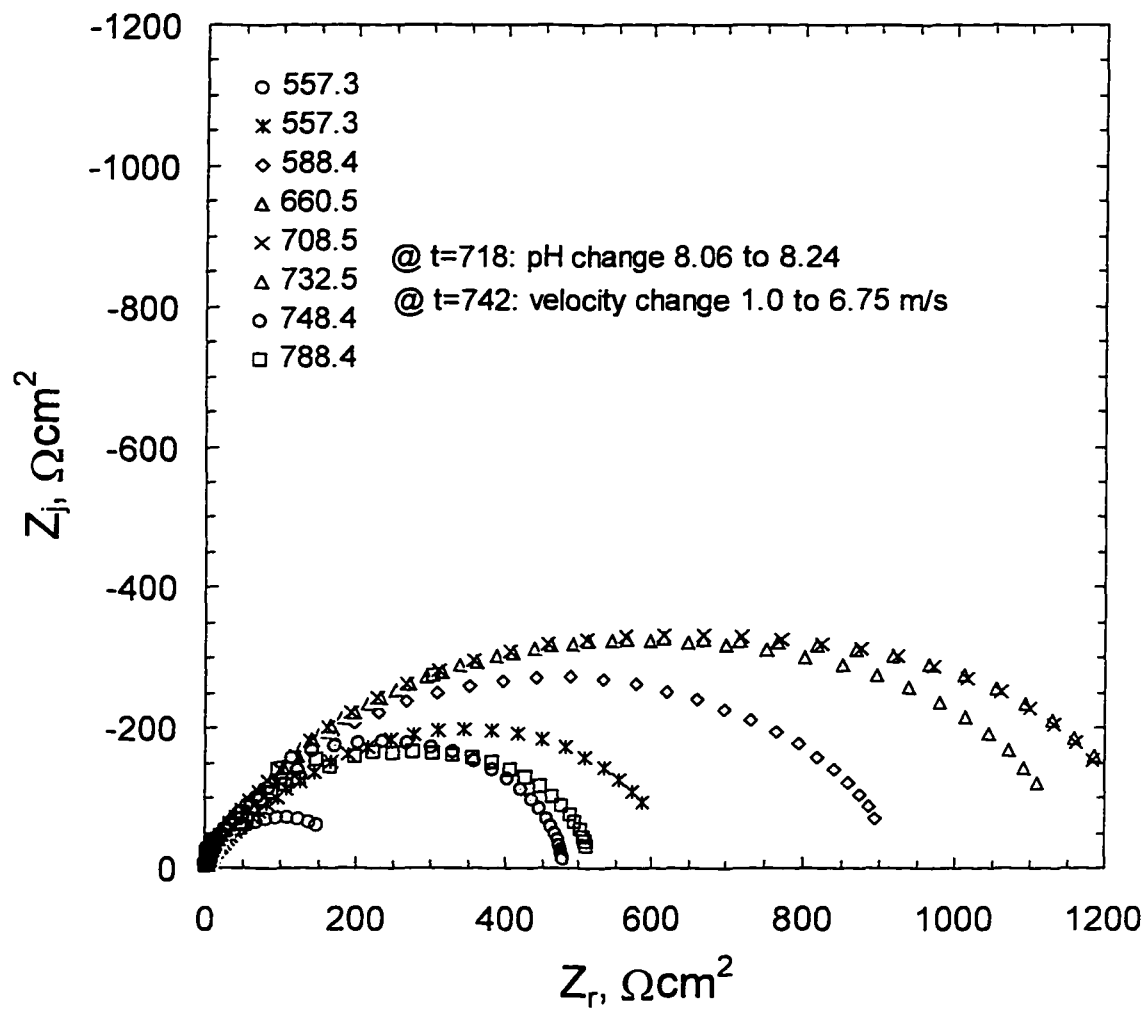
Figure 6.16: Impedance data collected for 99.9% Cu over the course of the 231 hours corresponding to the corrosion potential data in Figure 6.15.
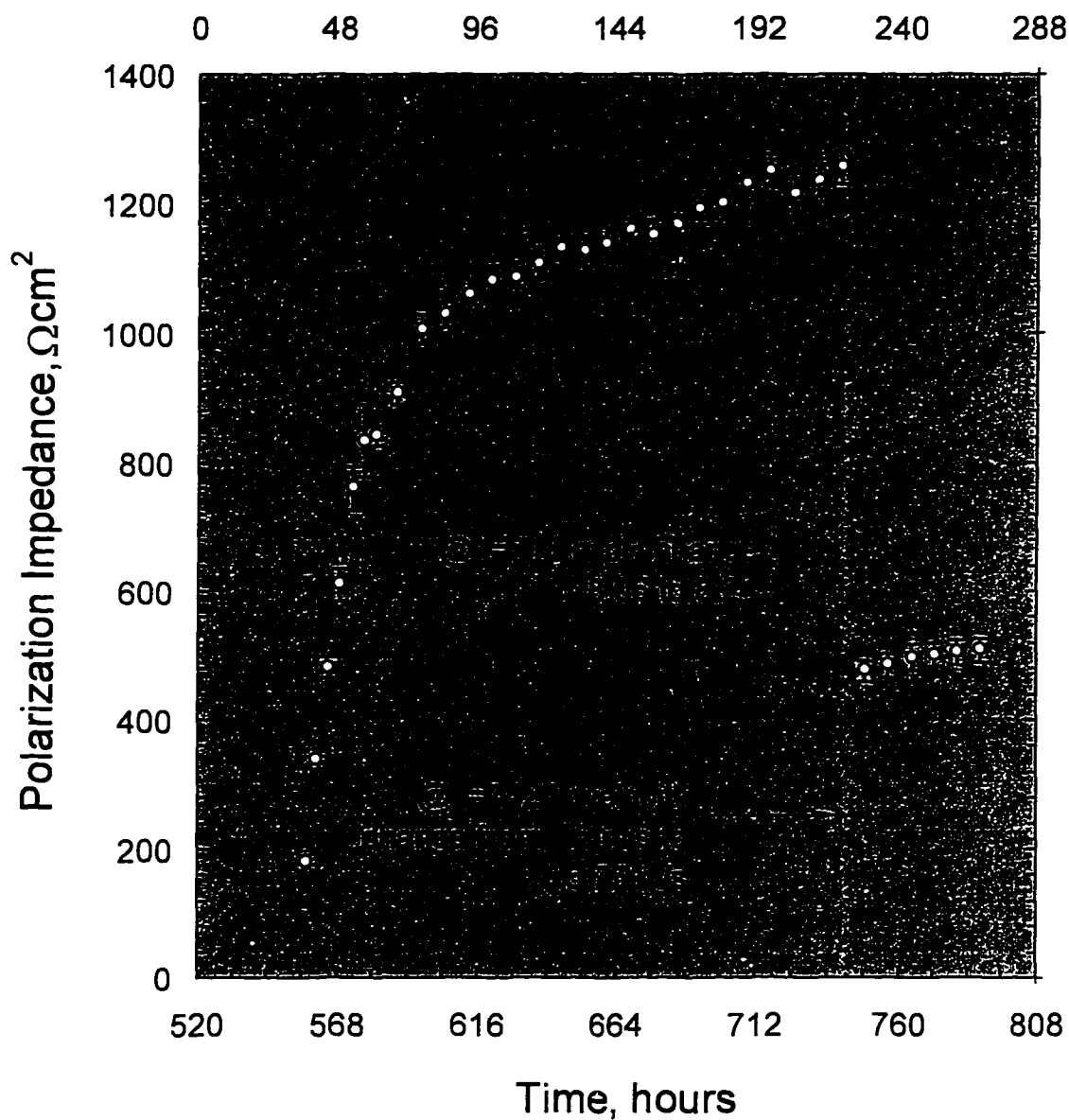
Figure 6.17: Polarization impedance encompassing impedance scans shown in Figure 6.16. Values and associated error were predicted through the use of a measurement model.
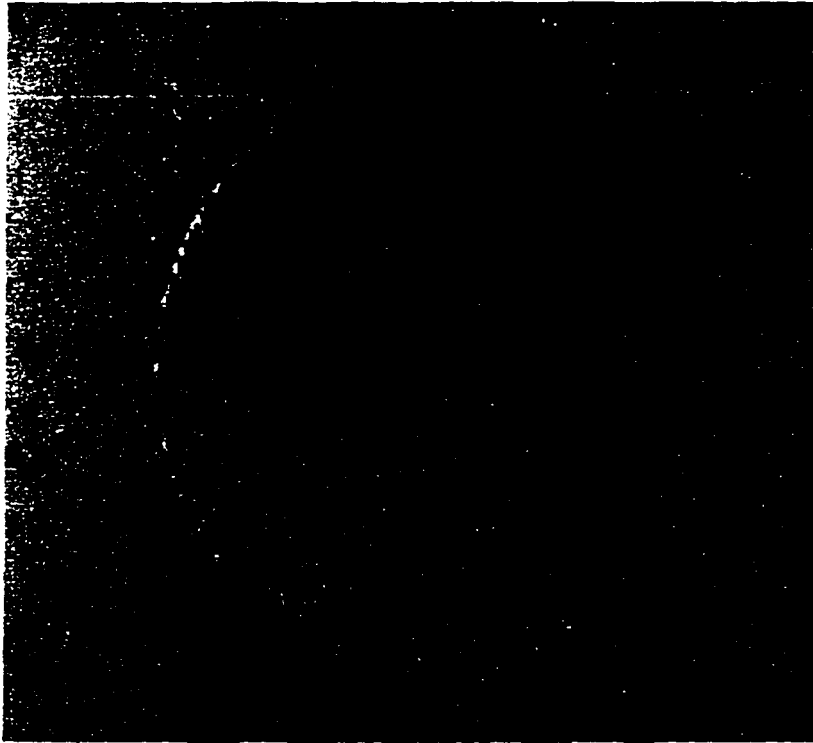
Figure 6.18: Video micrograph obtained for the experiment described in Table 6.1. Pure copper in non-aerated electrolyte immediately after submersion, time = 0 hours. Polished state.
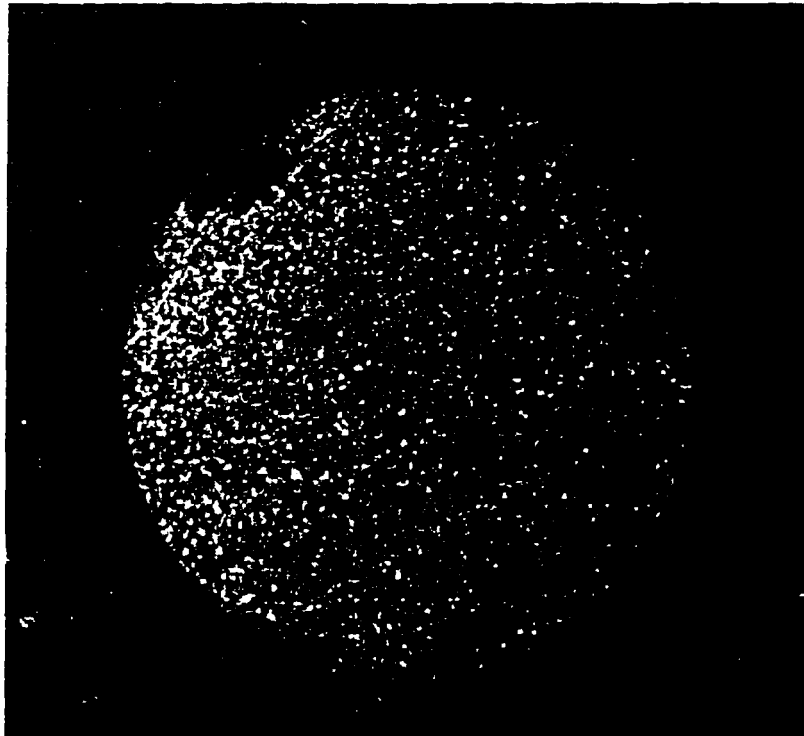
Figure 6.19: Video micrograph obtained for the experiment described in Table 6.1. Pure copper in non-aerated electrolyte at time = 169 hours.
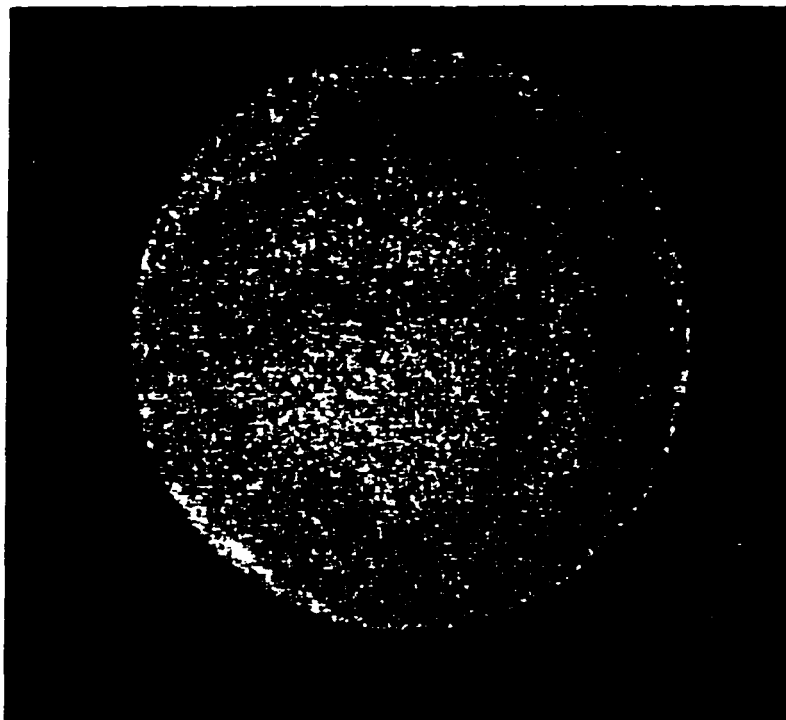
Figure 6.20: Video micrograph obtained for the experiment described in Table 6.1. Pure copper in non-aerated electrolyte at time = 671 hours.
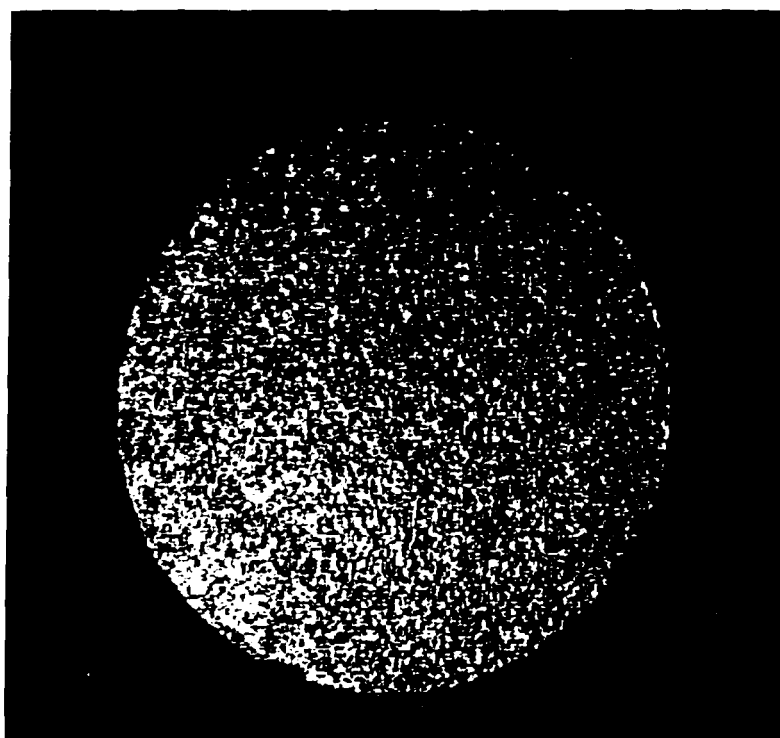
Figure 6.21: Video micrograph obtained for the experiment described in Table 6.1. Pure copper in non-aerated electrolyte at time = 814 hours.

6.4 Copper in Partially-Aerated Electrolyte: Part 2

The data presented in this section were collected without use of a pump for aeration. The only source of aeration was passive diffusion through the air-liquid interface in the solution reservoir resulting in a dissolved O_2 concentration of 6 ppm. Corrosion potential data is displayed in Figure 6.22 as a function of time for a 99.9% pure copper electrode in partially aerated synthetic sea water. A dramatic initial drop of 25 mV in the corrosion potential took place in the first 2 hours of immersion followed by an increase in the corrosion potential of approximately 40 mV followed the initial drop in potential. These rapid changes in the corrosion potential were attributed to the initial changes that took place when the electrode was taken from an air environment and place in an aqueous environment. The electrode surface was initially polished as described in the experimental methods chapter.

The formation and dissolution of films in the early stages of the experiment accounted for the changing corrosion potential as well as changing impedance values. The rate at which the corrosion potential changed was greatly reduced after the first six hours of immersion. A common pattern followed where the corrosion potential oscillated before coming to a pseudo steady-state value. The corrosion potential can remain somewhat constant over several hours or days during this pseudo-steady state condition. This behavior also indicates the formation and modification of one or more films on the surface of the electrode.

For this experiment the first pseudo steady-state value was -210 mV (SCE). A large drop in the corrosion potential was observed at time $\approx$ 50 hours, however, sufficient data was not available to determine the cause of this sudden shift in potential. The shift

could have resulted from an external perturbation in the form of pH and/or temperature shift, or from a naturally occurring phenomenal within the system. After this disturbance the system reached a pseudo steady-state value of -223 mV (SCE) and remained at this value, ± 1mV, until a modification in the flow rate was initiated.

Impedance spectra corresponding to the corrosion potential data in Figure 6.22 are displayed in an impedance plane plot in Figure 6.23. One can observe a steady increase in the impedance, as a function of time, until a constant value was reached, as indicated by the shaded circles and stars in Figure 6.23. The corrosion potential was constant at -223 mV (SCE) and the impedance spectra were collected 18 hours apart with good reproducibility. Experiments showed that even after the corrosion potential reached a constant value the impedance of the system continued to increase until eventually reaching a steady state condition. The impedance for this experiment reached and maintained a constant value until the flow rate was adjusted from 2.0 to 6.2 m/s. The increase in velocity resulted in an immediate decrease in the corrosion potential and impedance. Both the impedance and the corrosion potential again stabilized after the change in velocity, however, the values were different than the constant values before the velocity. Two major phenomena contributed to the decrease in the impedance, the first was an increase mass transfer of reacting species to the electrode surface. Also contributing to the decrease in impedance was the dissolution of salt film on the surface due to the velocity change. One can observe from Figure 6.23 that the impedance increased slightly after the initial decrease caused by the velocity change. The impedance eventually reached another pseudo steady-state condition. The higher flow prohibited the modulus of the impedance from reaching the previously higher value.

Multiple impedance spectra were consecutively collected at the conclusion of this experiment to investigate the effect of potential perturbation amplitudes on the surface films. The velocity was maintained at 6.0 m/s and the pH was 8.26. Several impedance spectra were collected consecutively in the VAG mode and the perturbation amplitude was incrementally increased with each scan. Periodically an impedance spectra was collected with a low target amplitude, e.g. 5.0 to 15.0 mV, to ensure a linear response and to determine whether previous the potential perturbation had disrupted or modified the protective film on the surface of the electrode.

Perturbation potential as high as 40 mV had no lasting effect on the impedance of the system, however, a perturbation potential of 50 mV dramatically effected the films present on the electrode surface. One can observe from Figure 6.24 that the modulus of the impedance irreversibly decreased by a factor of four due to the 50 mV potential perturbation. This is an extremely important observation in that potentials on the order of 50 mV can be generated somewhat easily and could result in the disruption of a protective film leading to premature failure of copper components in corrosion environments. The films that were removed or modified would eventually grow back but for the time frame of interest, this removal was irreversible.
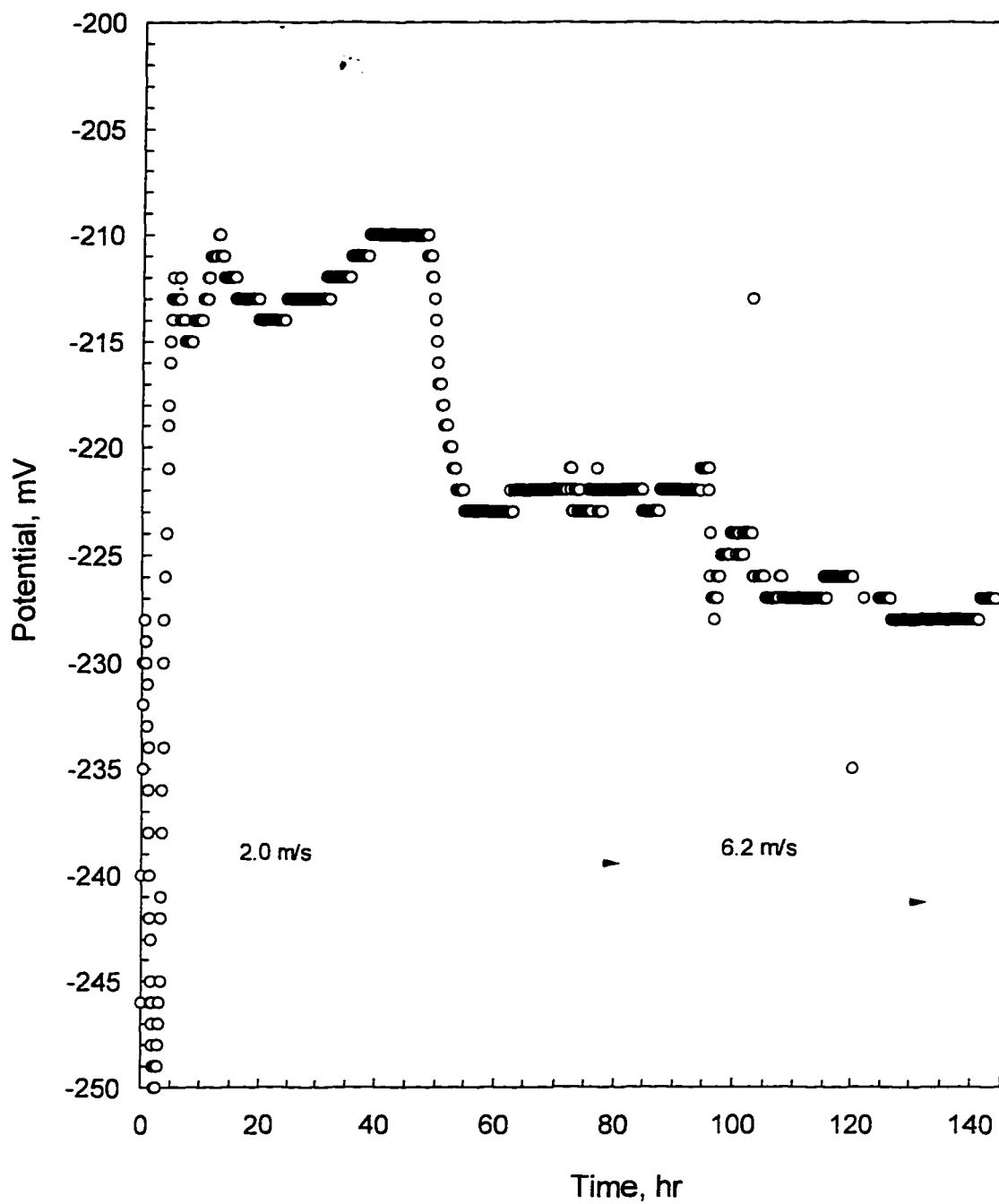
Figure 6.22: Corrosion potential as a function of time for a 99.9% pure copper electrode in non-aerated ASTM 1141 electrolyte. Change in the corrosion potential due to velocity increase is evident.
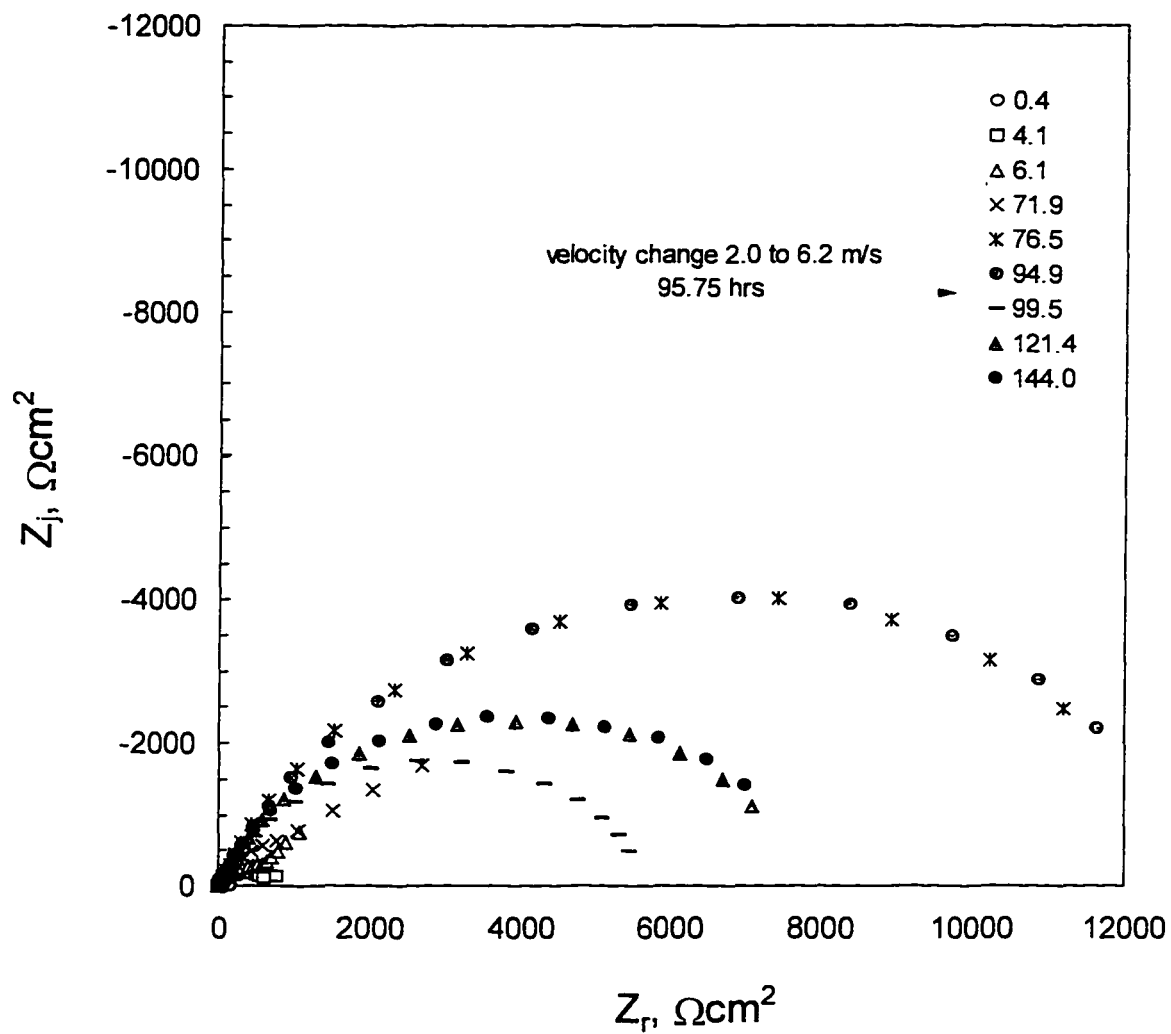
Figure 6.23: Impedance collected on 99.9% copper over a period of 144 hours. The solution was not aerated and the effect of a velocity change from 2.0 to 6.2 m/s is observable.
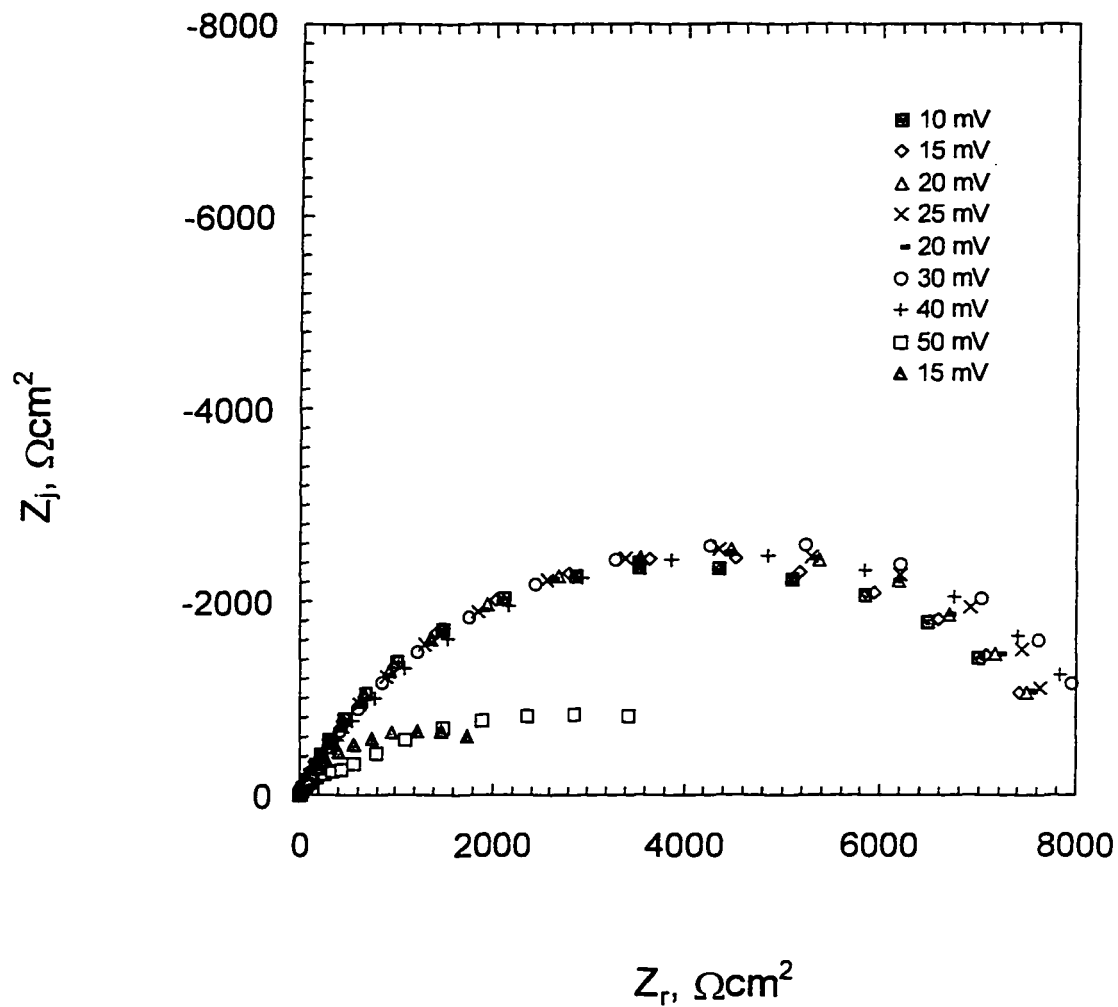
Figure 6.24: Nyquist plot for VAG experiments at different target amplitudes for 99.9% pure copper in non-aerated synthetic sea water. Effect of all amplitudes below 50.0 mV are reversible. An amplitude of 50.0mV dramatically and irreversibly changes the surface of the electrode.

6.5 70/30 Copper/Nickel Alloy in Aerated Electrolyte

The corrosion potential as a function of time for a 70/30 copper/nickel electrode in synthetic sea water aerated with CO_2 scrubbed air is displayed in Figure 6.25. The initial velocity was 2.0 m/s and the pH was 8.18. The initial drop and subsequent increase in the corrosion potential was not as dramatic as seen with the 90/10 copper/nickel or the pure copper. Similar to the other metals investigated, oscillations in the corrosion potential were evident with the 70/30 alloy. The 70/30 copper/nickel alloy did not reach a constant corrosion potential as quickly as did the copper, and, after eight days, the corrosion potential was still increasing. This was an indication that the reactions at the surface of the electrode was slower or thicker films were being formed. The copper nickel alloy also displayed a higher sensitivity to impedance measurement. Disturbances of up to 5 mV were seen after measurements. This disturbance to the system emanated from a performance flaw in the potentiostat, where if the potentiostat is remotely controlled, a mild potential was applied to the cell immediately after the remote cell on command was initiated and .ie the first data point was collected. The higher impedance values for this system lead to a greater potential disturbance for the same current perturbation. The 70/30 alloy approached a pseudo steady-state potential of -200 mV (SCE) after an increase in velocity to 6.0 m/s.

The impedance data corresponding to the corrosion potential plot in Figure 6.25 are presented in Figure 6.26. It is evident from the modulus of the impedance that the 70/30 alloy was more resistive to corrosion that was the pure copper. Impedance data collected on the sample over a two week period tended to be less predictable than the copper system. The modulus of the impedance increased and decreased in what seemed

to be a random manner throughout the entire experiment. A velocity change from 2.0 m/s to 6.0 m/s resulted in a moderate change in both the corrosion potential and the impedance values. Displayed in Figure 6.27 are data taken before and after the velocity change. Multiple sets of three spectra were collected at each time indicated to ensure reproducibility. The spectra collected 1 hour after the velocity change indicated a slight decrease in the modulus.

Presented in Figure 6.28 is the polarization impedance of the 70/30 alloy. One can observe how this value changed with time and also how the velocity change affected the polarization impedance. The polarization resistance can assists scientist and engineer assess the corrosion resistance of a material in the lab on in service in the field. Comparison between the predicted values for polarization impedance of the 70/30 copper/nickel versus the pure copper indicates that the alloy would perform significantly better (from a corrosion stand point, in sea water) than the pure copper.
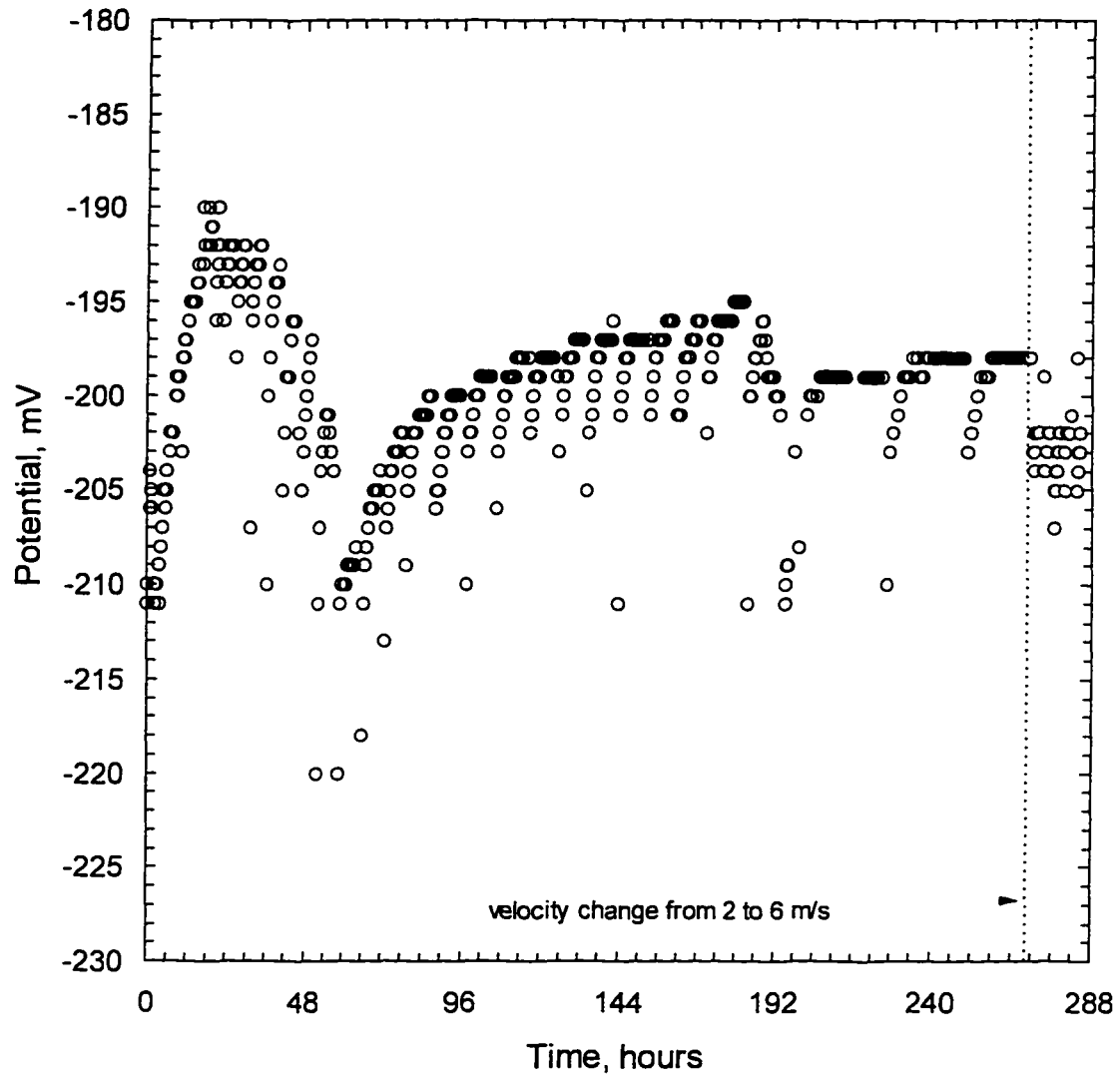
Figure 6.25: Corrosion potential (SCE) data collected on 70/30 copper/nickel over a period of 288 hours. The solution was aerated with CO_2 scrubbed air and the effect of a velocity change from 2.0 to 6.0 m/s is observable.
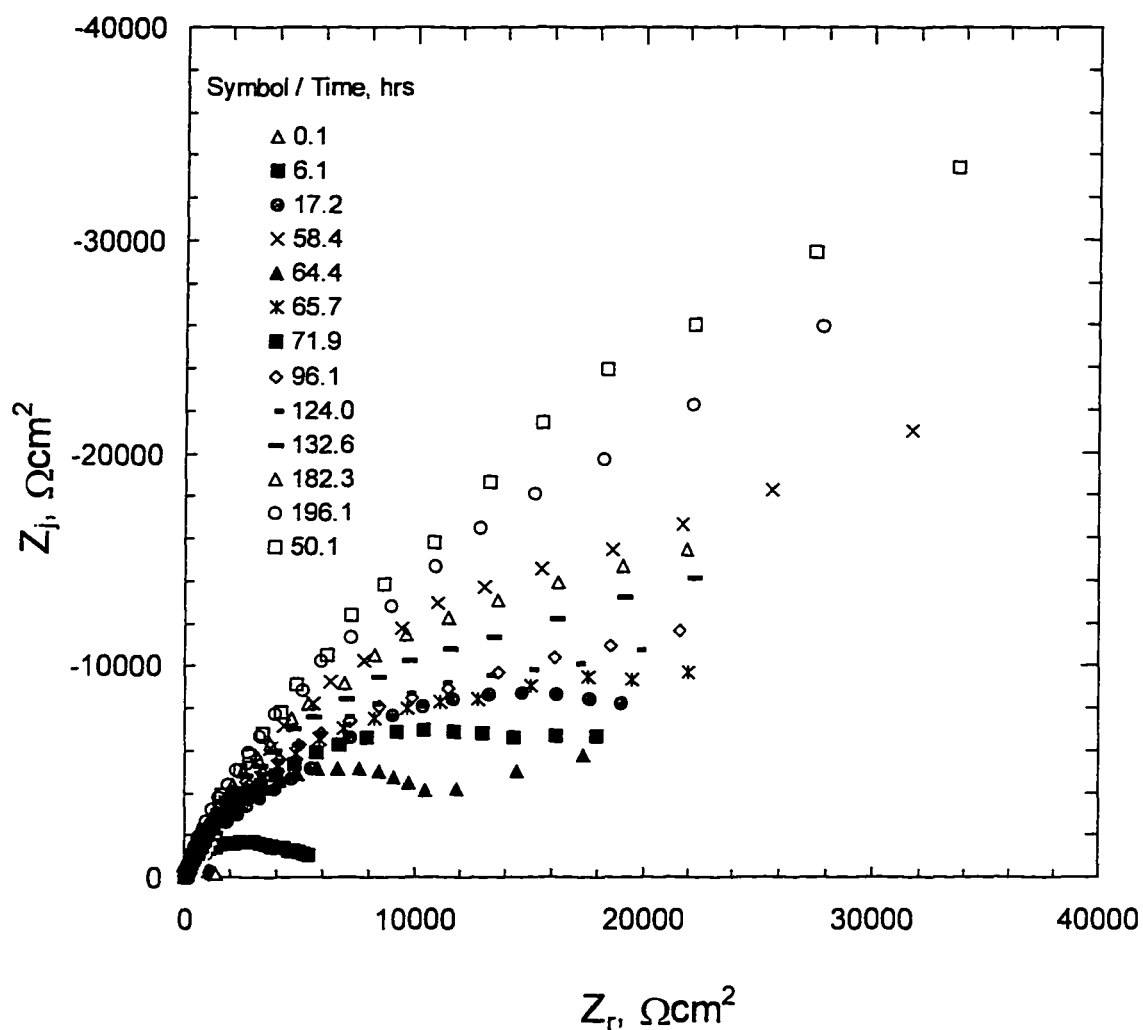
Figure 6.26: Impedance plane plot of several impedance spectra collected on a 70/30 copper/nickel alloy electrode with CO_2 scrubbed aeration over the course of 11 days. The susceptibility of the film to disturbance and measurement procedure is evident from the sporadic increase and decrease of the impedance values.
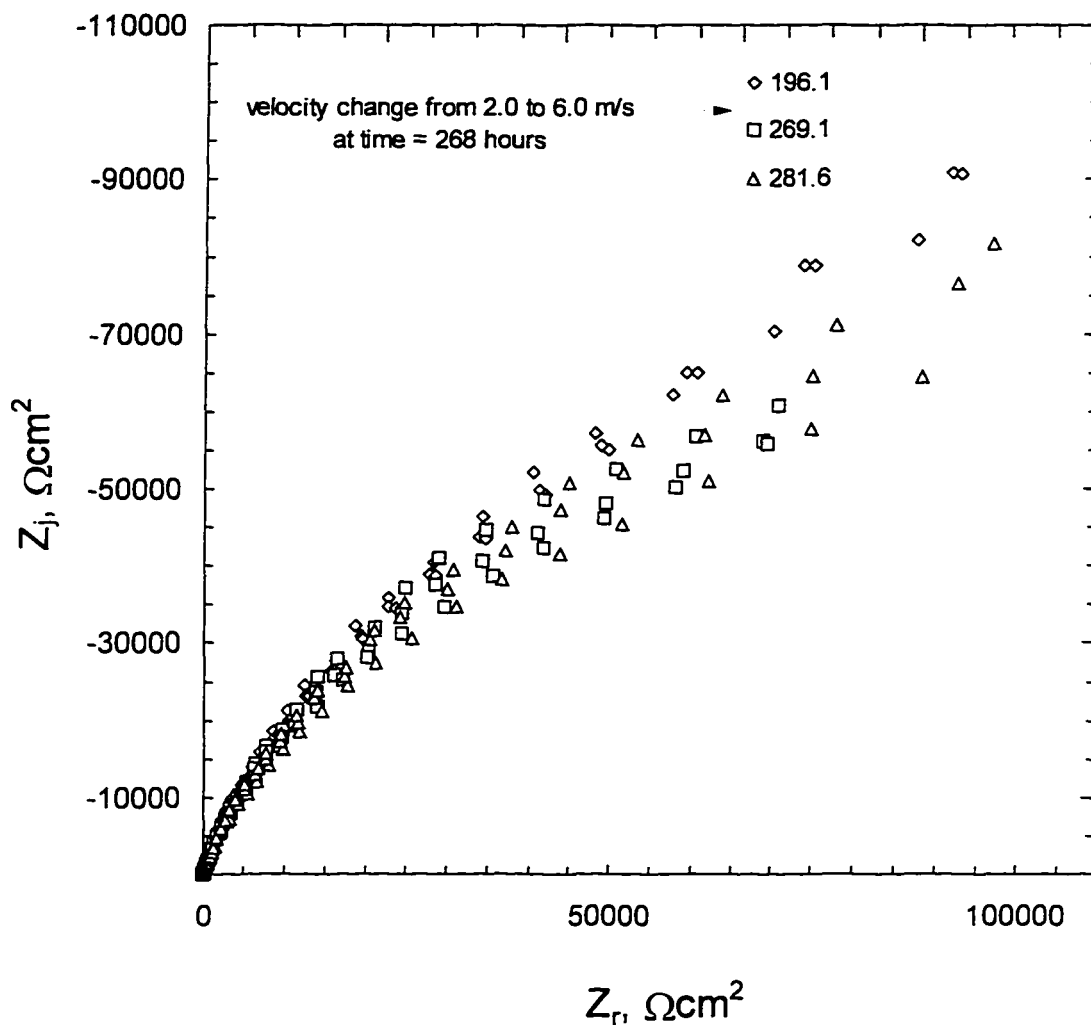
Figure 6.27: Impedance data collected on 70/30 copper/nickel corresponding to corrosion potential data in Figure 6.25. The solution was aerated with CO_2 scrubbed air and a slight effect of a velocity change from 2.0 to 6.0 m/s is observable.
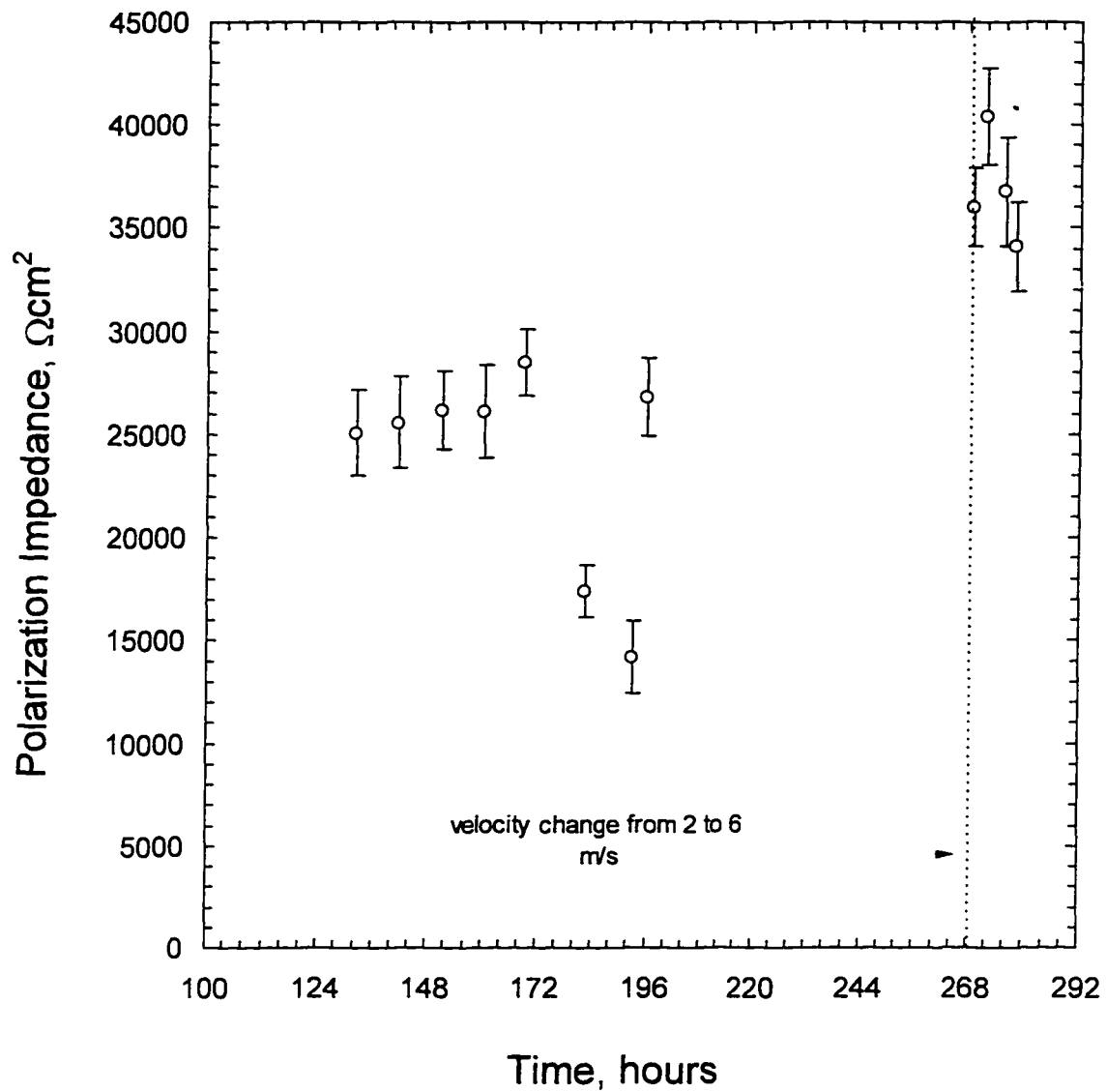
Figure 6.28: Polarization impedance predicted by the measurement model for 70/30 copper nickel alloy in synthetic sea water.

6.6 Copper in Aerated Electrolyte

The data presented in Figures 6.29 through 6.36 were collected on a copper electrode in synthetic sea water aerated with CO_2 scrubbed air. The dissolved O_2 concentration was 7.0 ppm and the pH was 8.2. The corrosion potential data for the system is displayed in Figure 6.29. A cathodic potential of -414 mV was applied to the electrode for 120 seconds after submersion and immediately prior to data collection to remove oxide films which may have formed after electrode preparation. The initial decay in the corrosion potential evident in each of the other experiments was not present in this experiment due to the cathodic potential applied to the electrode. This potential removed any oxide layer which formed after polishing and cleaning and during the time involved in mounting the electrode in the cell base plate.

The initial velocity for this experiment was 1.0 m/s which was incrementally increased over the 20 days of this experiment. The corrosion potential increased over the first three days of immersion, as was characteristic of all other systems investigated in this work. After reaching a maximum of -215 mV, the corrosion potential decreased at a fairly constant rate until day ten. At this point the corrosion potential remained at -243, ±3 mV, until a velocity change was implemented 48 hours later. The velocity was increased from 1.0 to 2.0 m/s resulting in a decrease of 2 mV in the baseline corrosion potential. Figure 6.30 contains impedance data collected before and after the velocity change. The constant value for the impedance displayed on the impedance plane plot of Figure 6.30 indicates that a pseudo steady state condition had been reached before the velocity change. The change in velocity had little effect on the magnitude of the impedance which can be observed by the shaded diamonds and triangles in Figure 6.30

(taken immediately after and 26 hours after the velocity change). The slight decrease in the magnitude of the impedance can be attributed to increased mass transfer of the reactive species to the surface and not to removal of a film. Film removal is expected to cause a dramatic reduction in the impedance.

The velocity was increased from 2.0 m/s to 4.0 m/s at time = 340 hours. This increase in velocity had a minimal effect on both the corrosion potential and the impedance response. Figure 6.29 displays a decrease of approximately 2.0 mV in the corrosion potential. Impedance data collected before and after the velocity change are presented in Figure 6.31. The system had again reached a pseudo steady state condition before the velocity change which is apparent by the constant impedance values recorded for greater than 24 hours preceding the velocity change. The increased mass transfer to the surface had a slight effect in the impedance response which can be observed in Figure 6.31. A velocity change from 4.0 to 6.2 m/s yielded similar results. Figure 6.32 displays impedance data before and after each velocity change and the overall difference in the magnitude was small compared to what one would expect for velocity-enhanced corrosion due to removal of an oxide film. Oxide films have a protective quality and removal of these films would have resulted in a large reduction of the impedance. The small changes in the corrosion potential and impedance response for each velocity change in this case can be attributed to increased mass transfer to the surface and time dependent characteristics of the system.

The polarization impedance of the copper electrode as a function of time for the entire experiment is presented in Figure 6.33. The change in velocity had little effect on the predicted polarization impedance, reaffirming the conclusion that shear removal of a

film was not present for this system even at the high shear rates present at velocities over 6.0 m/s.

The corrosion potential of the electrode for the first 24 hours of immersion is presented in Figure 6.34. The effect of holding a cathodic potential on the electrode before collecting data is evident. Figure 6.35 contains impedance data for the first 24 hours where the magnitude of the impedance decreases after immersion and reaches a minimum around time = 8 hours. The decrease in the impedance may indicate a roughening of the surface which is supported by video images. The magnitude of the impedance increases after the minimum until a pseudo-steady-state condition is reached. The corresponding polarization impedance predictions are displayed in Figure 6.36 where an initial decrease in the polarization resistance is visible. This decrease is associated with removal of native oxide layers that were not removed by the pre-polarization of the electrode. The increase in the polarization impedance, after reaching a minimum, indicated that the surface of the electrode was becoming increasingly resistant to corrosion.
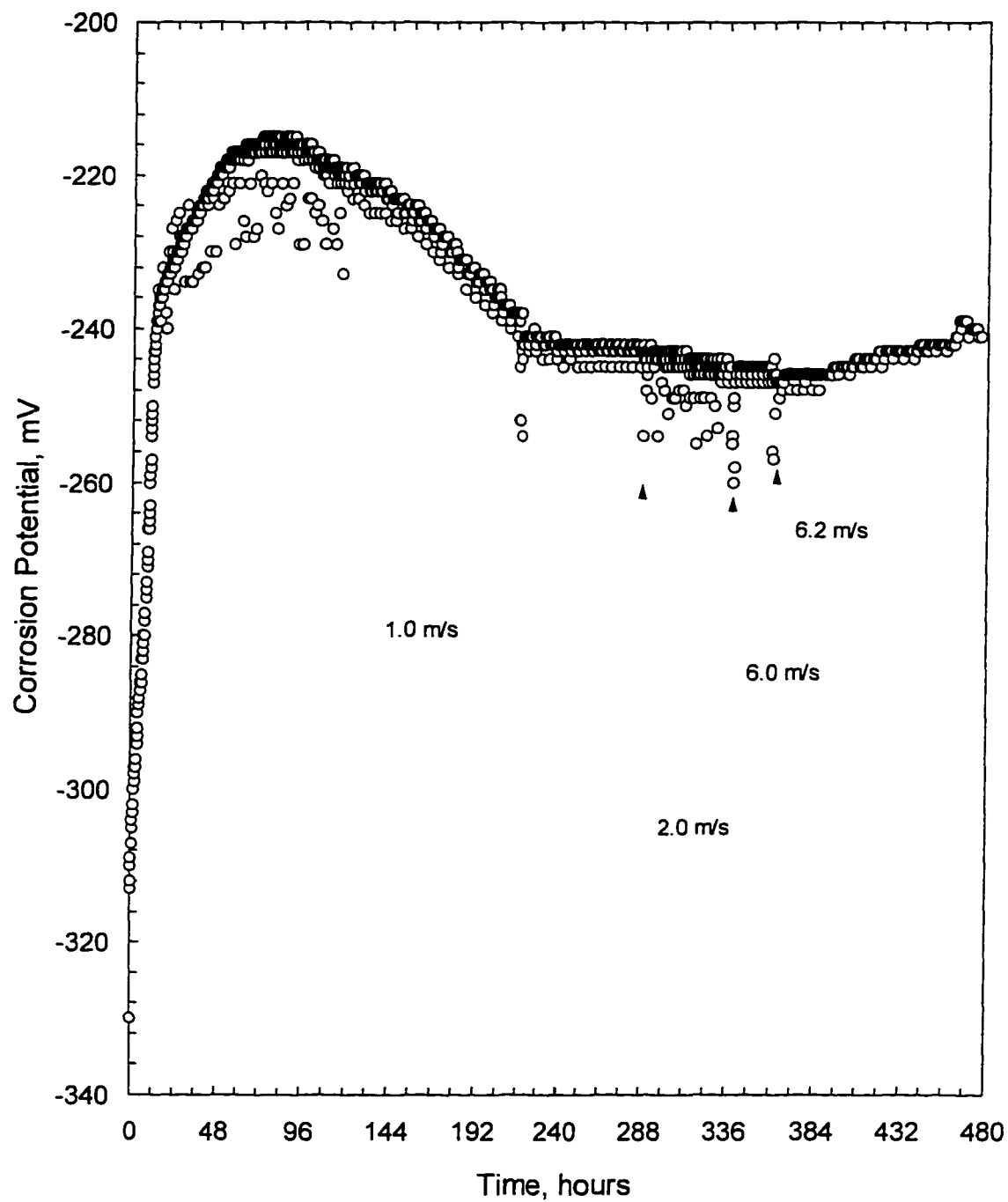
Figure 6.29: Corrosion potential measured of copper as a function of time for well aerated synthetic sea water electrolyte. A negligible effect of velocity is seen.
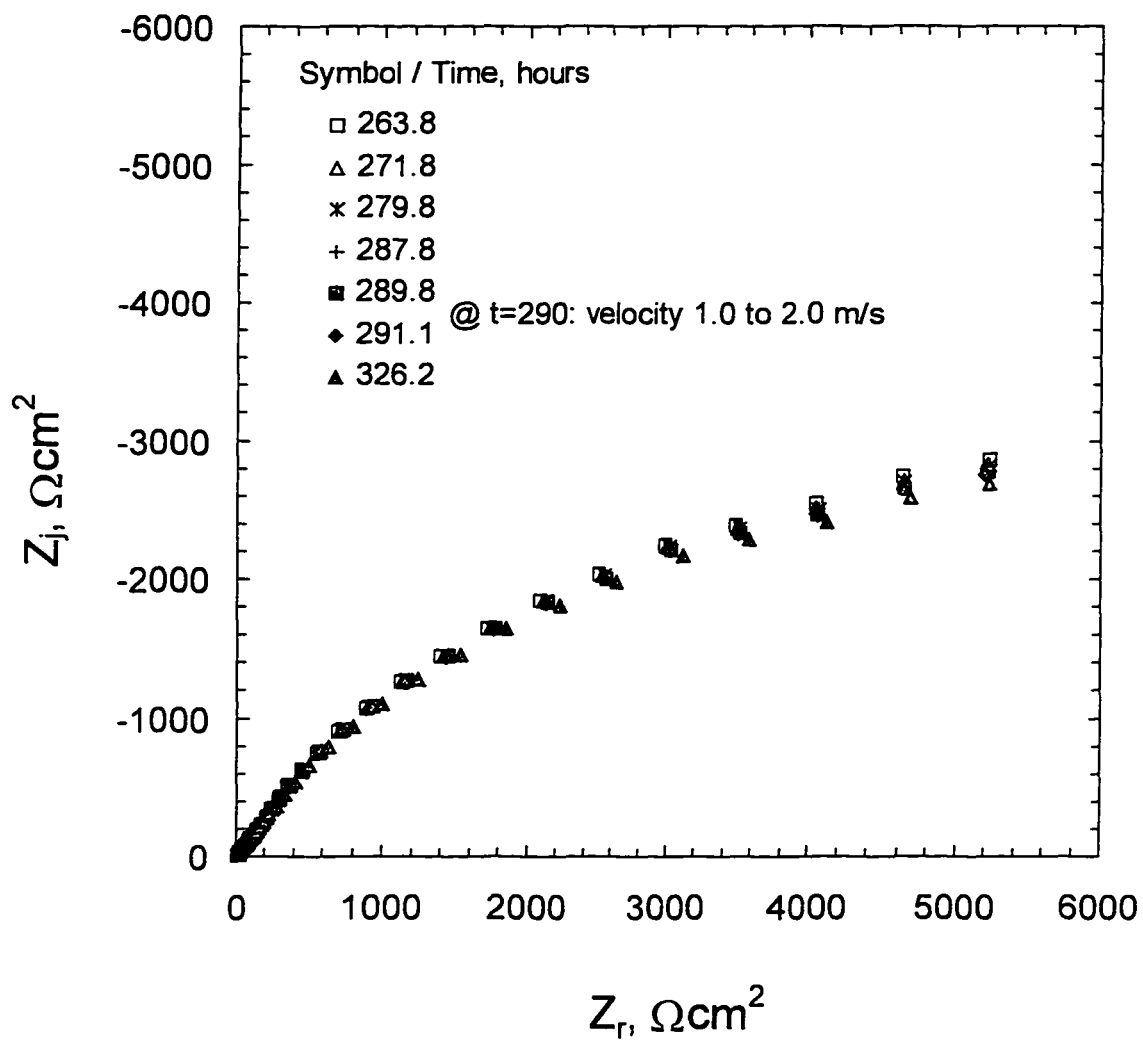
Figure 6.30: Impedance plane plot for copper electrode in well aerated sea water before and after velocity change from 1.0 to 2.0 m/s.

122
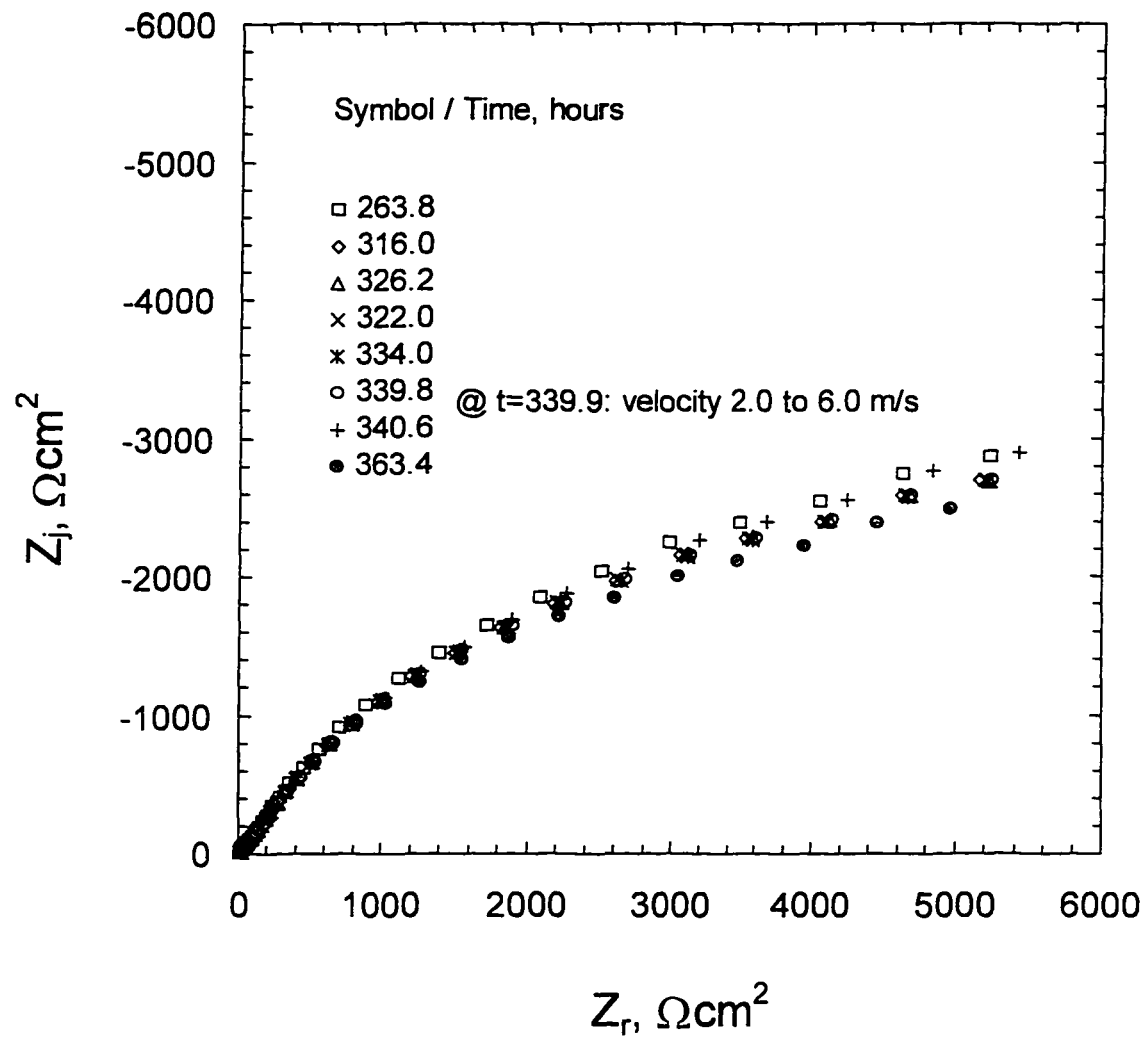
Figure 6.31: Impedance plane plot for copper electrode in well aerated sea water before and after velocity change from 2.0 to 6.0 m/s.
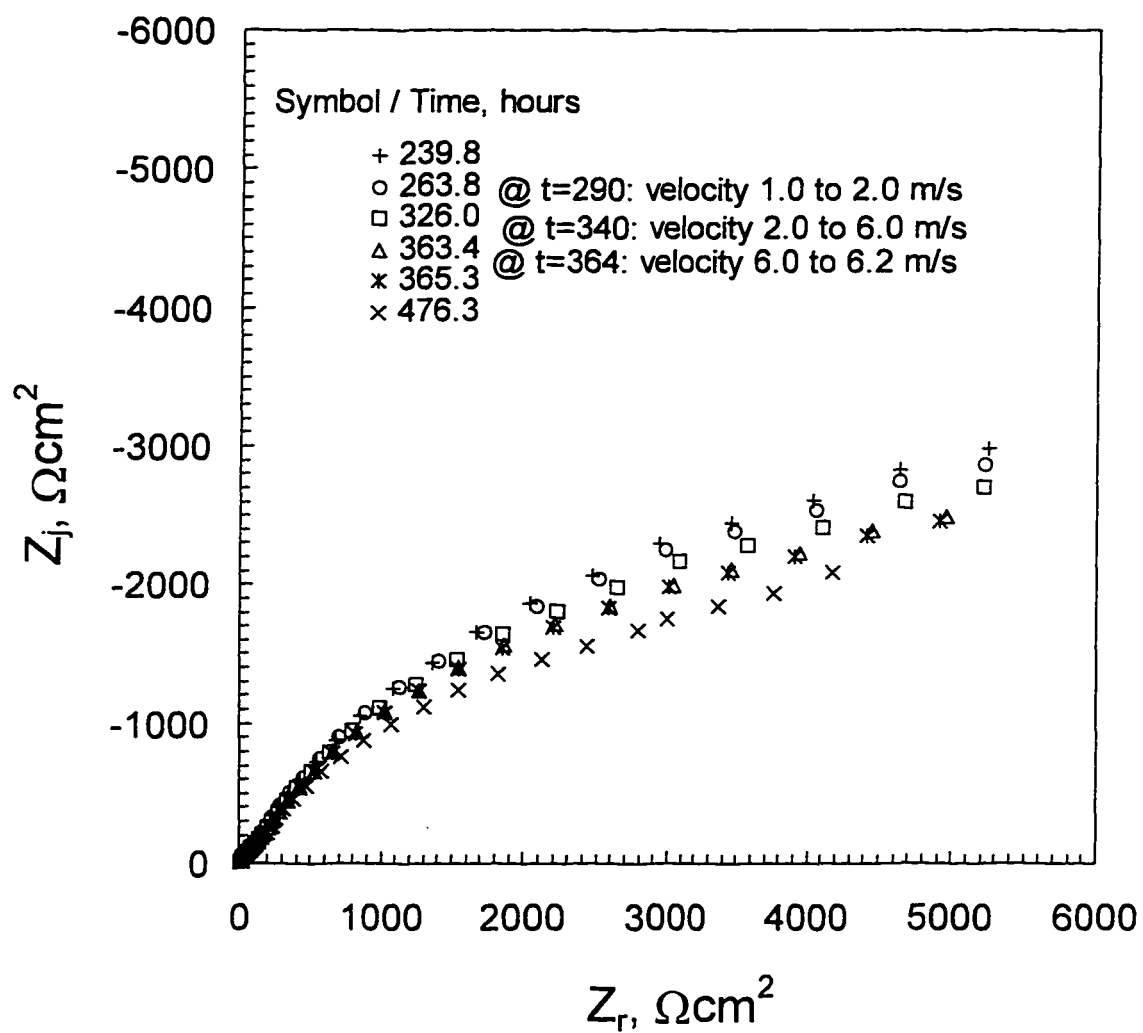
Figure 6.32: Impedance plane plot for copper electrode in well aerated sea water over the course of three velocity changes.
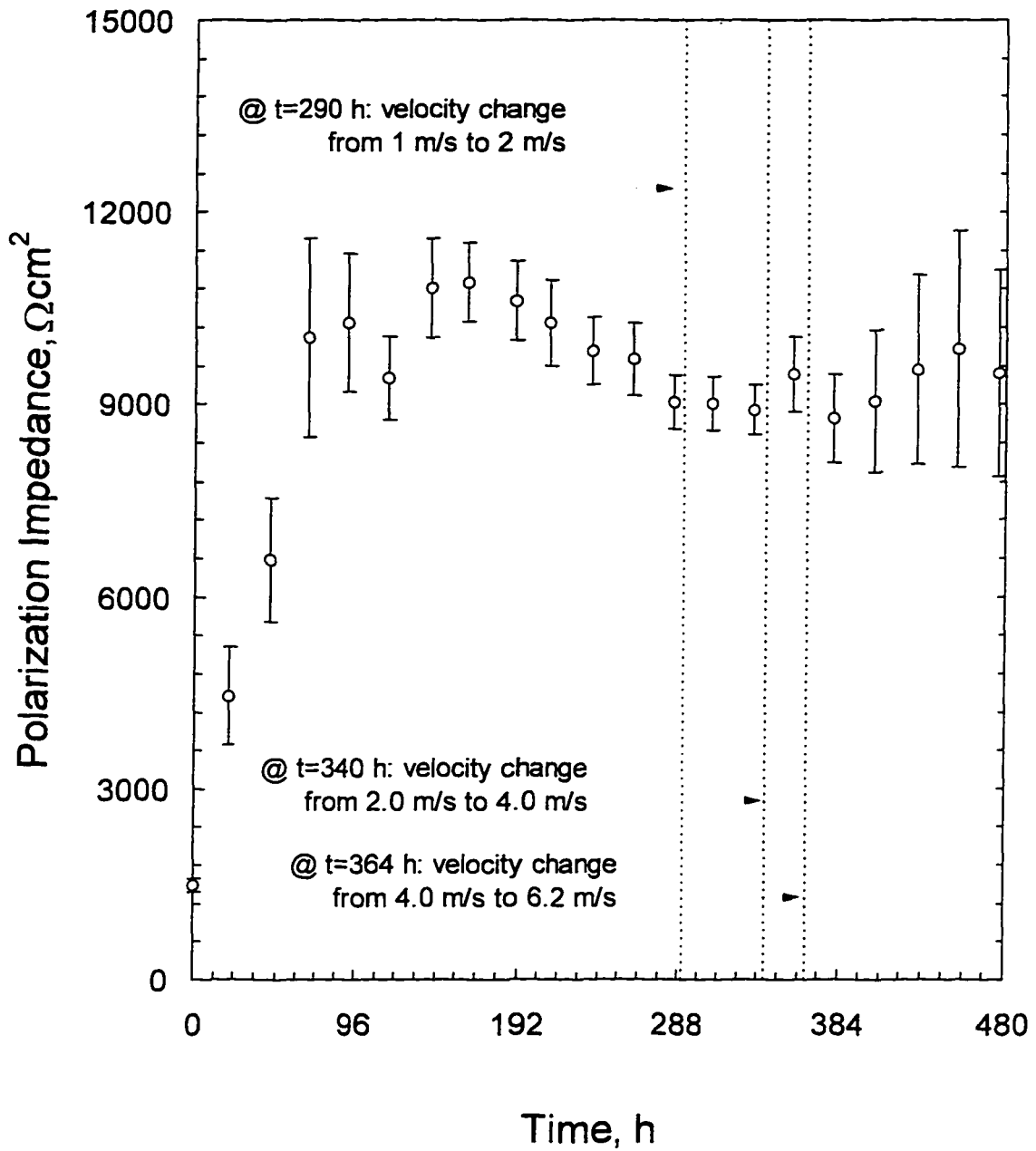
6.33: Predicted polarization impedance for aerated copper synthetic sea water system. Values and associated error predicted through the use of a measurement model. Error bars indicate the 95% confidence interval for each point predicted by a Monte Carlo simulation routine.
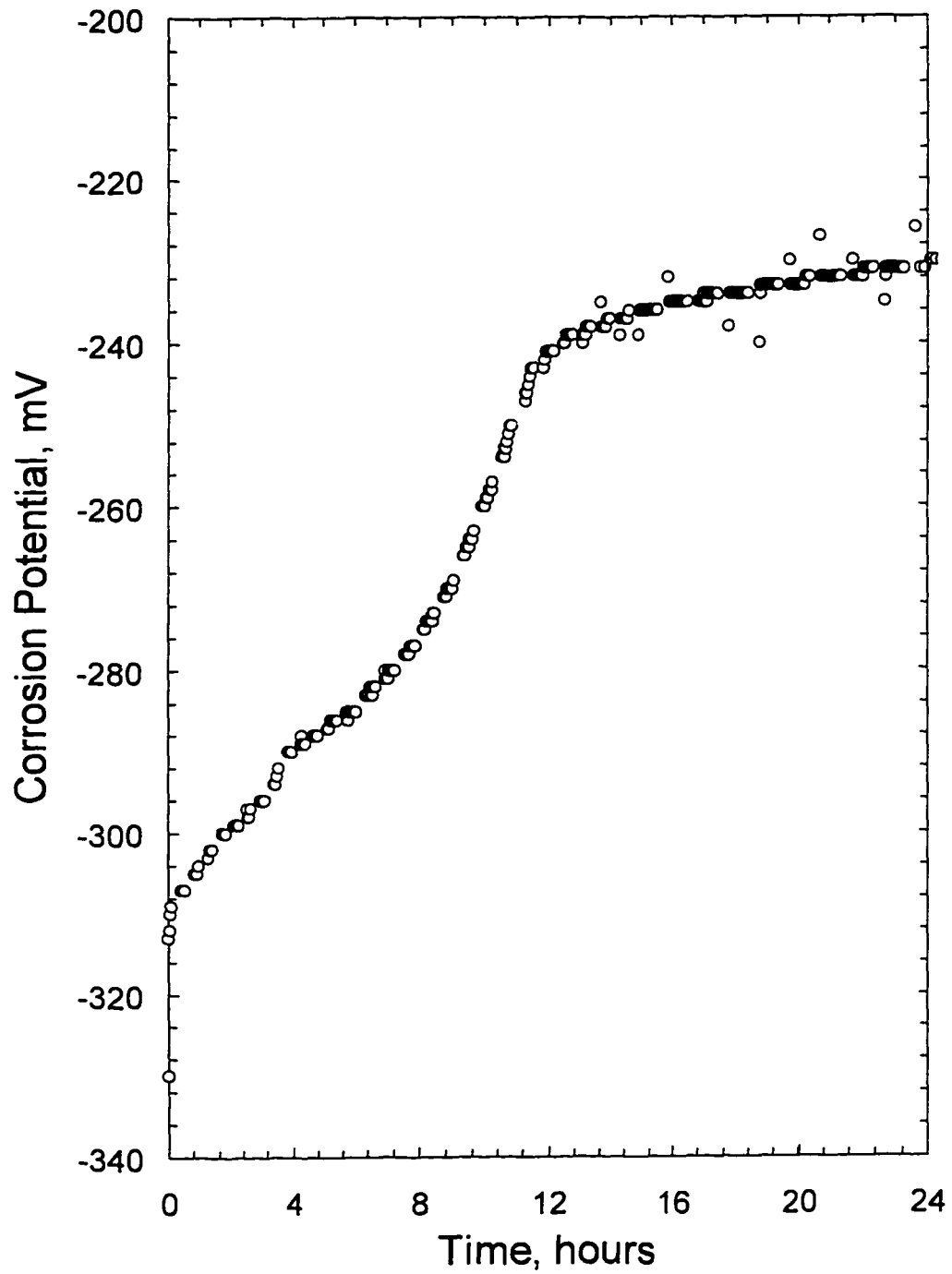
Figure 6.34: Corrosion potential data for the first 24 hours for data presented in Figure 6.29.
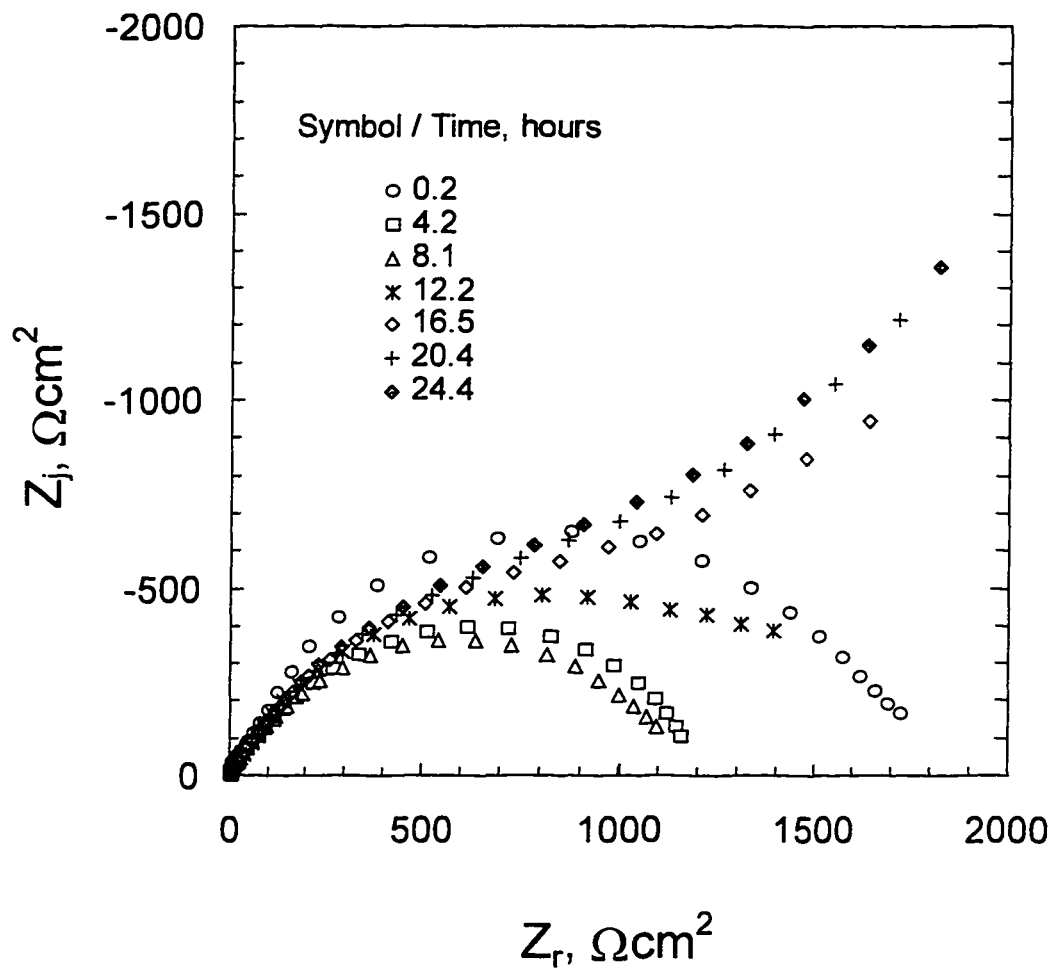
Figure 6.35: Impedance plane plot for copper electrode in well aerated sea water for the first 24 hours of submersion. Jet velocity = 1.0 m/s.
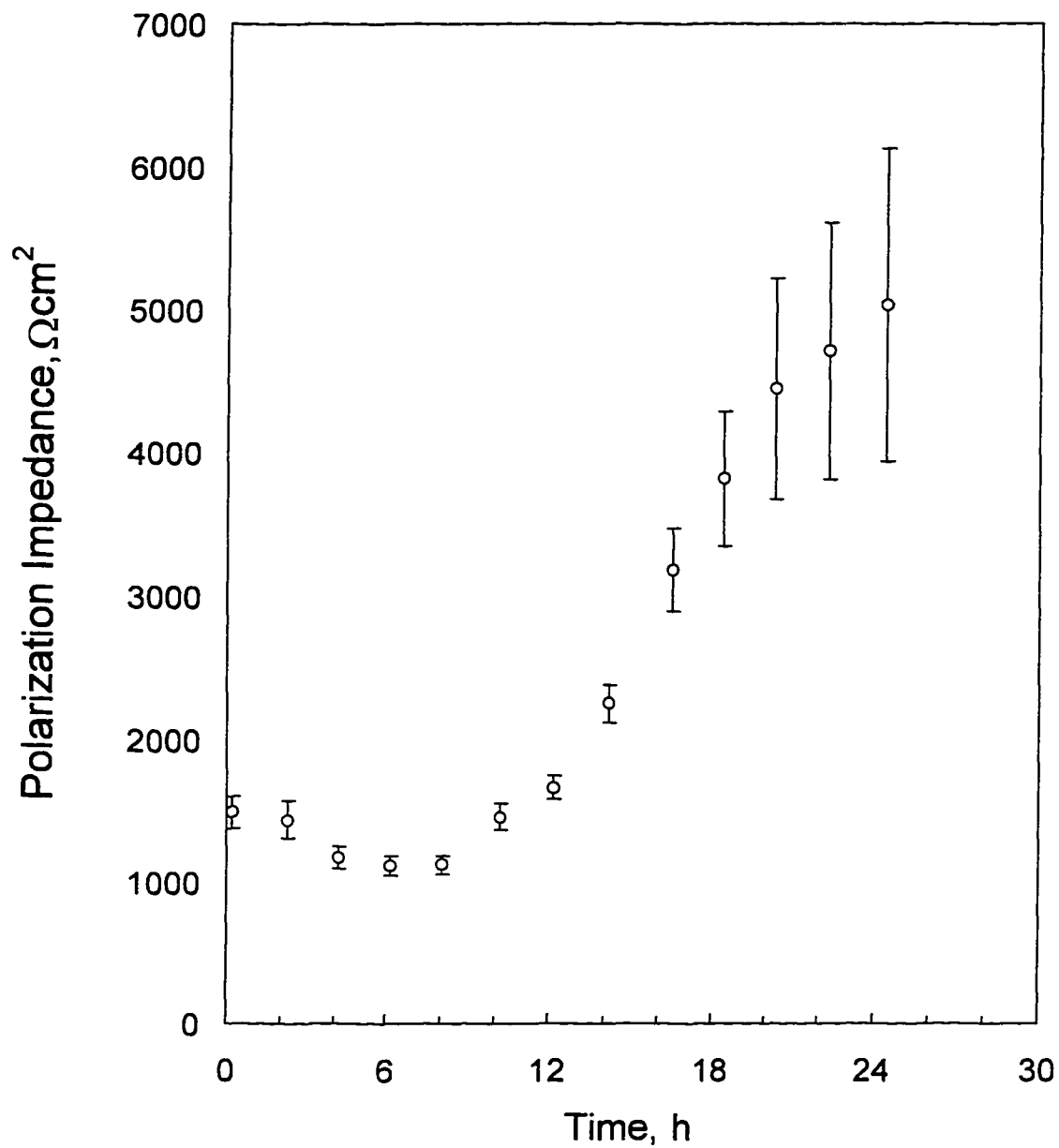
Figure 6.36: Predicted polarization impedance for data displayed in Figure 6.35. Values predicted using the measurement model technique. Error bars indicate the 95% confidence interval for each point predicted by a Monte Carlo simulation routine.

6.7 X-ray Photoelectron Spectroscopy Analysis

In order to investigate what species were present on the surface of a copper electrode after submersion for a period of time, X-ray photoelectron spectroscopy was employed. This analysis technique was implemented to obtain high resolution, high magnification images of the electrode surface after exposure to sea water. XPS also provided a semiquantitative tool for the comparison of element concentrations on the surface of the electrode under different conditions. Concentrations differences related to aeration technique are explored in this section.

X-ray photoelectron spectroscopy, or XPS, is a semiquantitative surface analysis technique useful in investigating elements within the top ten atomic layers. XPS subjects the sample of interest to a beam of X-rays causing emission of a photoelectron. The photoelectrons are emitted from atoms near the surface and are detected by a hemispherical analyzer located above the sample. The energy of the photoelectron is equal to the difference in the X-ray energy, $h\upsilon$, and the electron's original binding energy, E_B.

$$E = h\upsilon - E_B - WF \tag{40}$$

The work function, WF, of the specimen reduces the energy of the detected electron by a small amount. The photoelectron energy is characteristic of the binding energy which depends on the atom species and type of bonding. Therefore, the total number of photoelectrons at a given energy reflects the concentration of a given species with a particular type of bonding (MAIC).

XPS has applications ranging from investigating thin films and interfaces, to the study of thermodynamically unstable species such as polymers, to identification of a specimen's near surface composition. For this work XPS was utilized to determine species present in the copper film and to compare results from films formed in partially aerated solution and aerated solution. The data presented here is in the form of the x axis representing the binding energy of the species and the y axis representing a normalized energy, detected energy, or concentration of species with a given binding energy. Characteristic photoelectron peaks for each element are plotted and the peak size reflects the element concentration in a semiquantitative manner (MAIC).

Data presented in Figures 6.37 through 6.41 include XPS and scanning electron microscope, SEM, data. The XPS data gave a semiquantitative analysis of what elements were present at the surface and the concentration of these elements which in turn gives an indication of what compounds were present. The corresponding SEM image in Figures 6.37,39-41 give a visual representation of the area that was analyzed by XPS. The magnification of the SEM images ranged from 15X to 2000X.

Figures 6.37 and 6.38 contain data collected for a copper electrode previously exposed in partially aerated sea water. The dissolved O_2 content was 6.0 ppm. Solutions that are not vigorously aerated with CO_2 scrubbed air will absorb CO_2 from the atmosphere and this dissolved CO_2 will react with species in solution to form complexes and acids, shifting the pH to a more acidic value. CO_2 production, consumption and dissolution into solution plays a strong role in the regulation of pH in natural waters (Stumm 1981). A slight decrease in the pH (pH=8.17) of the solution for this experiment

was seen due to CO_2 absorption. The number of species present at the surface are considerably less than with aerated solutions.

Figures 6.39 through 6.41 display XPS data and SEM micrograghs a copper electrode previously exposed in aerated sea water. Each data set was obtained at different magnification or location on the electrode surface. The pH for this experiment, which used the same solution as for the partially aerated case, was approximately 8.27. The increase in the pH can be attributed solely to the removal of dissolved CO_2. A slight increase in the bulk pH can cause enough of a change in the local pH to support a variety of film which were not stable in less alkaline environments. Elements including aluminum, magnesium, potasium, calcium, and iron are all distinguishable on the XPS traces when an aerated solution was the electrolye These species complex to make salt, oxide, or other films which are stable in more alkaline environments. One can observe from Figures 6.40 and 6.41 a reduction in the copper species at the surface which was attributed to the selective reaction with the other species and the covering of the surface with films not containing copper. A more significant amount of copper is observable Figure 6.39 because the area analyzed is large and portions of the electrode are not covered by copper deficient films.

The XPS data supports the conclusion that the absorption rate of CO_2 was higher with the passive aeration than with the forced aeration. The higher concentration of dissolved CO_2 resulted in a slight decrease in the bulk pH which shifted the equilibrium of the system to allow films of different composition to form on the surface and be stable.

Figure 6.37: XPS and SEM data for copper electrode after exposure in partially aerated sea water. Magnification for SEM micrograph = 2000X.

TN-5 00   TUE 20-AUG-96   12:35
Cursor: 0.000KeV = 0   ROI   (42) 0.000: 0.000

0.000   VFS = 512   10.240
30
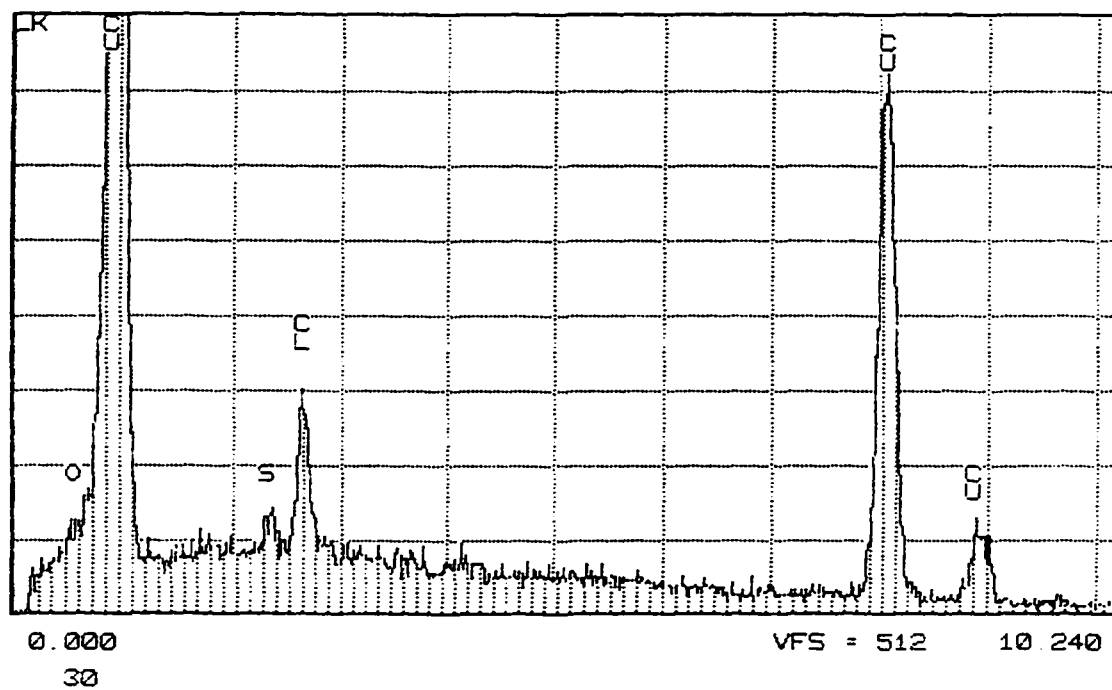
Figure 6.38: XPS data for copper electrode after exposure in partially aerated sea water. Analysis for entire electrode surface.

SERIES II   MON 21-AUG-95 16:11
Cursor: 0 000keV = 0

0 000   VFS = 2045   10 240
  20   SAMPLE #1
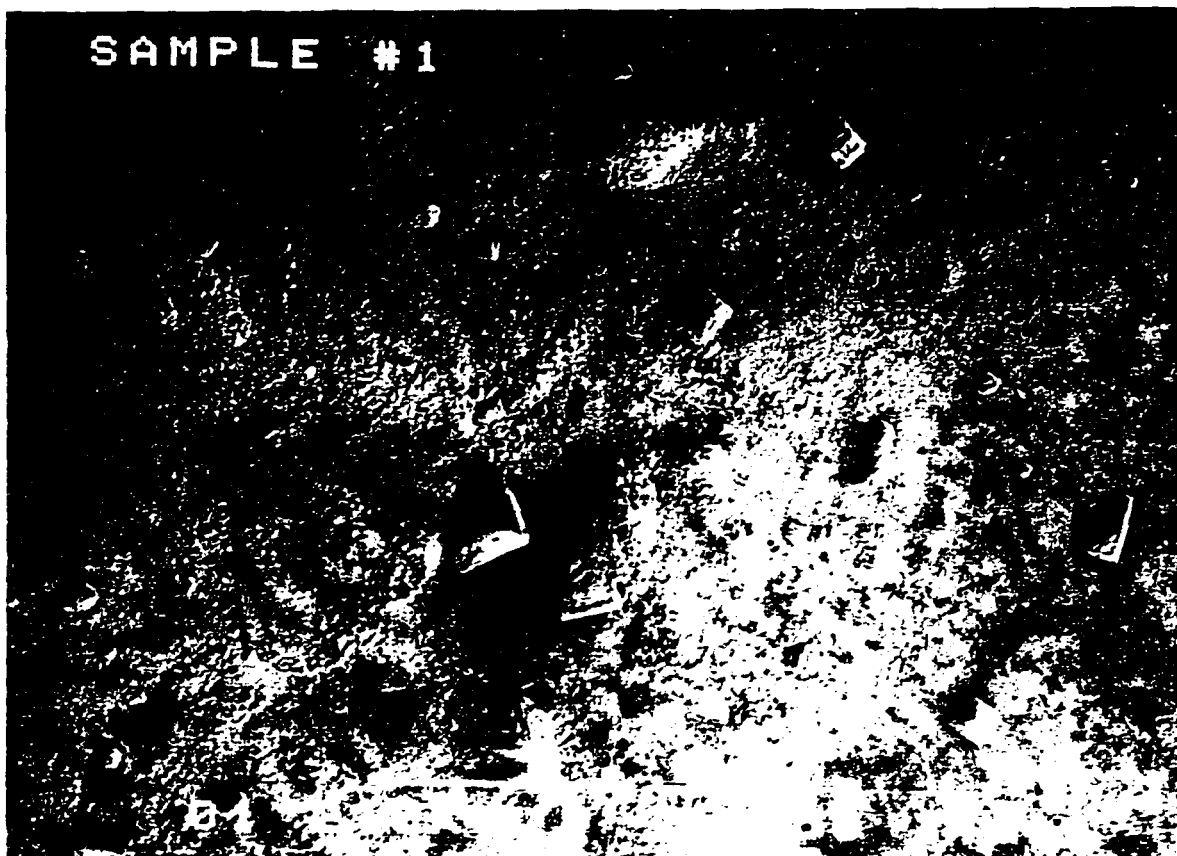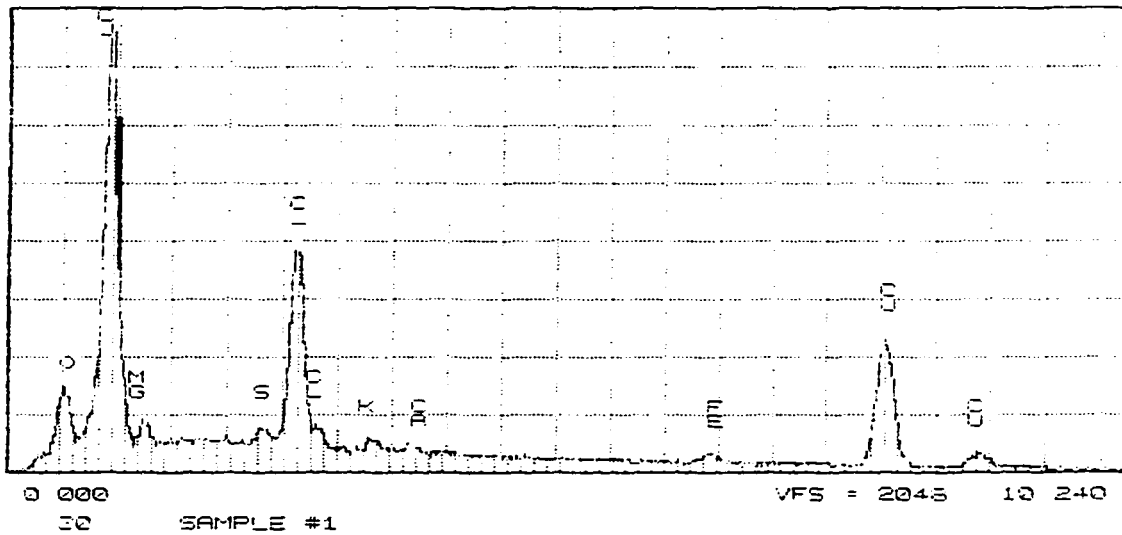
Figure 6.39: XPS and SEM data for copper electrode after exposure in aerated sea water. Magnification for SEM micrograph = 250X.
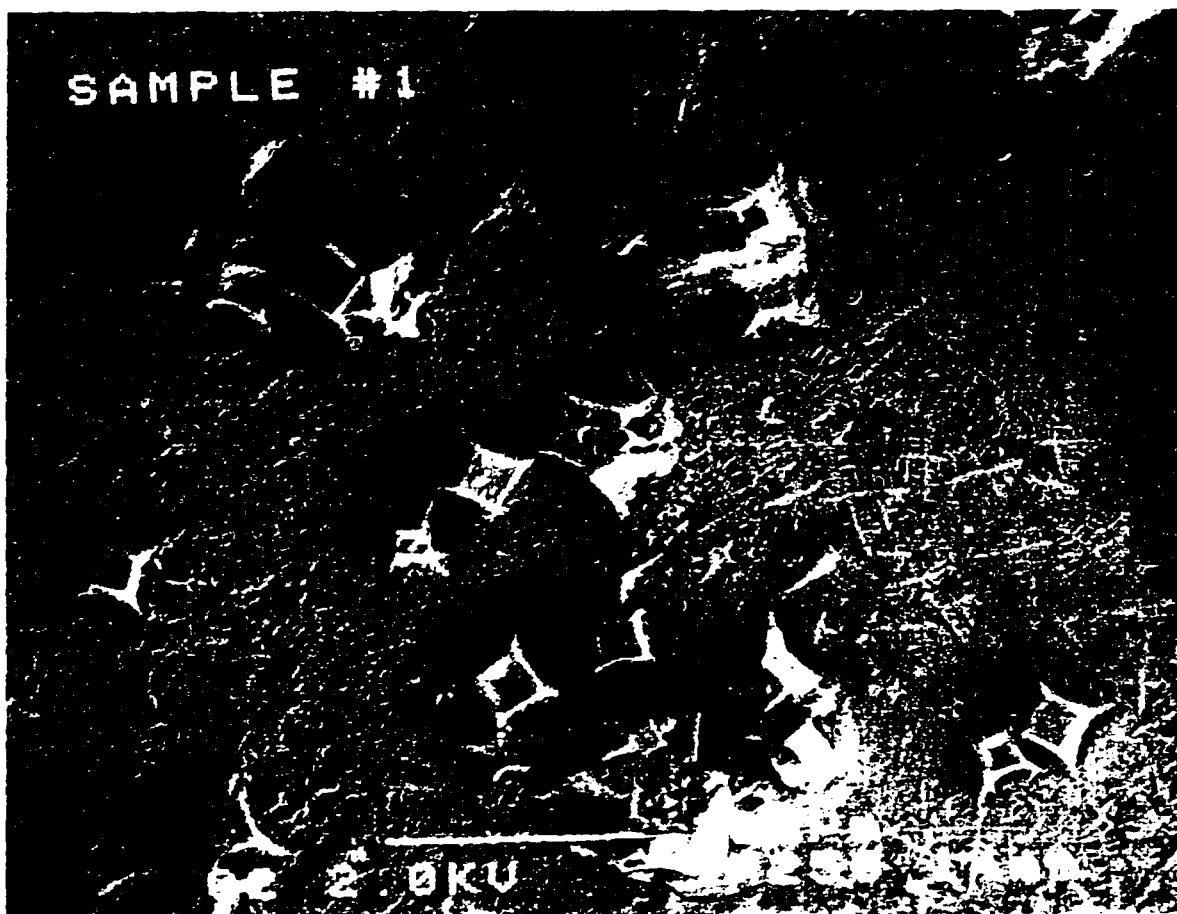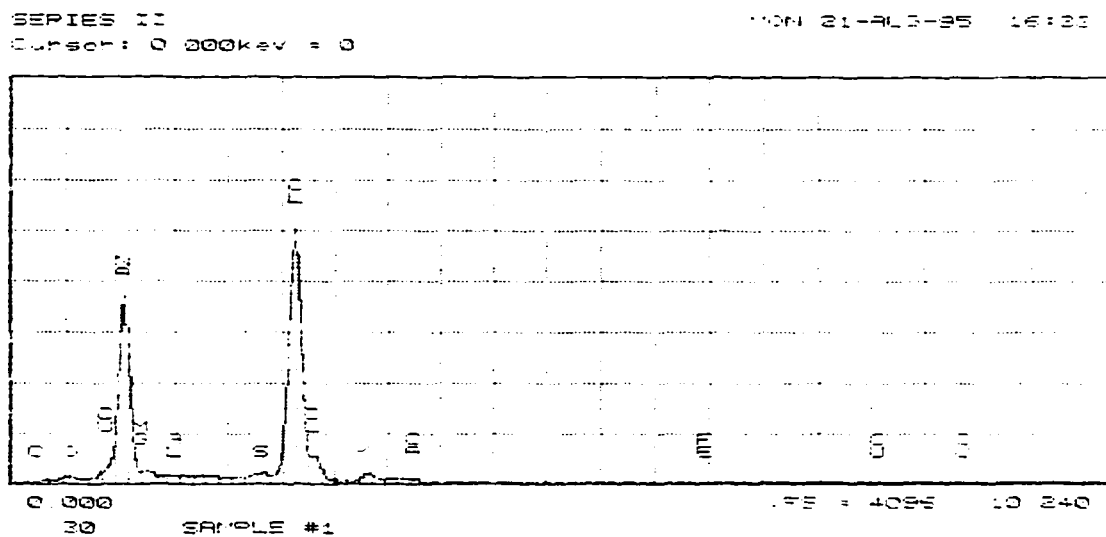
Figure 6.40: XPS and SEM data for copper electrode after exposure in aerated sea water. Magnification for SEM micrograph = 250X.
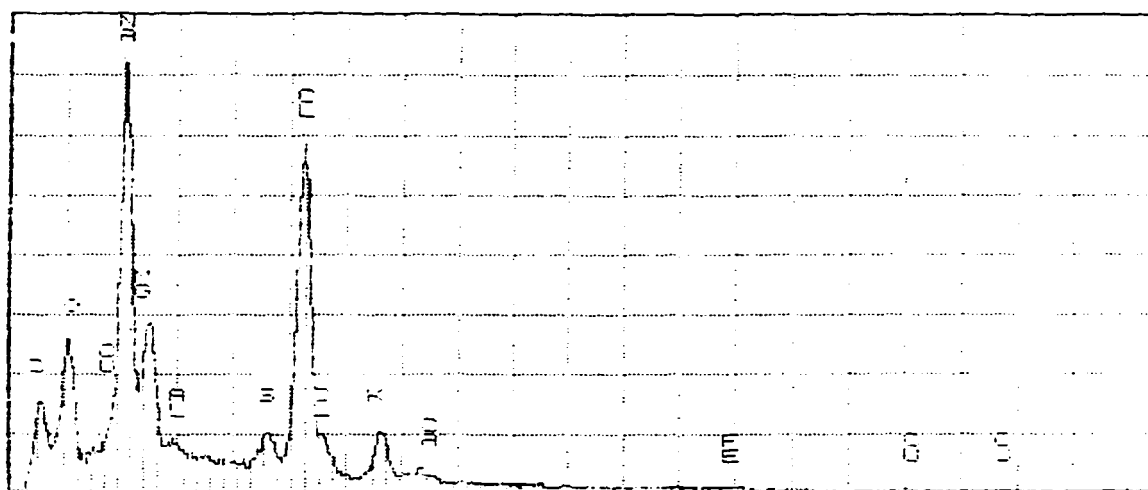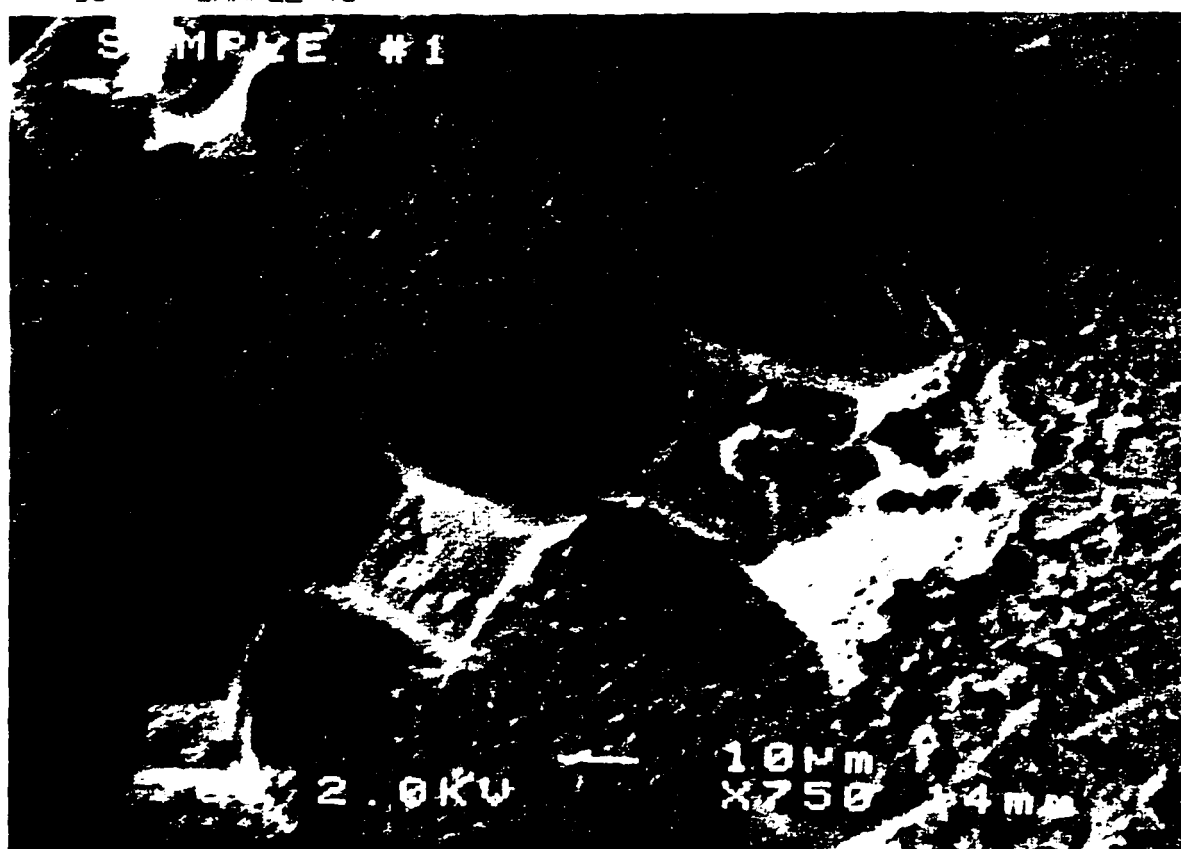
Figure 6.41: XPS and SEM data for copper electrode after exposure in aerated sea water. Magnification for SEM micrograph = 750X.

6.8 Copper Rods in Synthetic Sea Water

To explore the importance of geometry when determining shear induced enhance corrosion, a group of experiments were conducted using flow past a copper rod. The velocity for these experiments was held constant around the cylindrical vessel by a magnetic stirrer and was determined to be approximately 0.5 m/s at the leading edge of the copper rods. This velocity corresponds to a shear that is less than half the reported value for critical shear; therefore, no shear induced corrosion was expected. Thus, any patterns which appeared to correlate to flow were due to other flow induce phenomena.

Two copper rods (alloy = CDA 110) of purity 99.9+% and diameter 0.25" were polished with 4000 grit silicon carbide polishing paper, ultrasonically cleaned in ethanol and submerged in a covered cell of diameter 4.5". The cell contained an inlet and outlet port for solution circulation and the level of the solution provided a submersion depth of the electrodes of approximately 2". The rods were positioned vertically in the cell, 2.5" apart. Laboratory temperature, which remained fairly constant at 25°C, dictated cell temperature. A stirring bar was place in the cell directly between the two rods and the plate stirrer was set to the minimum setting. The pH of the solution at the beginning of the experiment was 8.1 and dropped to 7.62 during the course of the experiment. The final solution conductivity was 74.8 mΩ^{-1}. The rods were allowed to corrode freely for 30 days in synthetic sea water ASTM 1141. Three liters of solution were constantly circulated at 6.0 ml/min through the cell and back to an open air beaker. The cell maintained a constant volume of 500 ml.

Flow patterns observed on the electrode surfaces were consistent with the flow of solution. Figures 6.42 and 6.43 show portions of the electrode where non-uniform films had formed. These blue-green films formed preferentially on the trailing edge of the electrode. An explanation for this may be the fact that mass transfer to the circumference of the electrode was not uniform or that the shear stresses on the electrode surface are lowest at the leading and trailing edge. These films are loosely adhered.

Figures 6.44 and 6.45 show a white band on the surface of the electrode perpendicular to the direction of flow. The highest velocity is believed to be present in these regions. It can be observed from Figure 6.45 that the velocity is reduced near the electrolyte / air interface.

Neither rod formed a uniform or tightly adhered film. A blue-green precipitate collected at the bottom of the cell and refreshing beaker, further supporting the theory that neither electrode passivated and each continued to corrode freely throughout the experiment. An image of the precipitate collected from the bottom of the open air beaker in a pipette is shown in Figure 6.46. The wet precipitate and dry precipitate placed on filter paper are shown in Figures 6.47 and 6.48 respectively. Past experiments using a single rod in a similar cell showed a thicker more developed film and less precipitate being produced. This may suggest that small potential differences between the rods causes the removal of the film as each rod changes roles from acting as an anode first and then as a cathode.

Impedance scans were conducted on both electrodes with platinum foil as the counter electrode and a SCE as the reference electrode. In order to conduct the impedance scans it was necessary to remove the copper electrodes from the cell and place

them in a separate bath. The bath was a stagnant system with electrolyte from the stirred system. The modulus of the impedance was on the same order of magnitude as past situations where a single rod was placed in solution. Because the system changed, (primarily due to the elimination of flow), the impedance values of the rods changed rapidly during the course of three consecutive scans. The six impedance scans (three for each rod) are presented in Figure 6.49. The impedance values for each rod consistently decreased with time. This result is consistent with the observation that the films present on the electrode surface were loosely adhered and flaked off the rod after the system changed. From past experience it is known that if the rod were allowed to remain in solution, the impedance would decrease to a point and then increase as more stable films formed.

These experiments allude to the importance of cell design when investigating shear induced enhance corrosion. Mass transfer phenomena affecting corrosion can be falsely perceived as a shear induced phenomena.
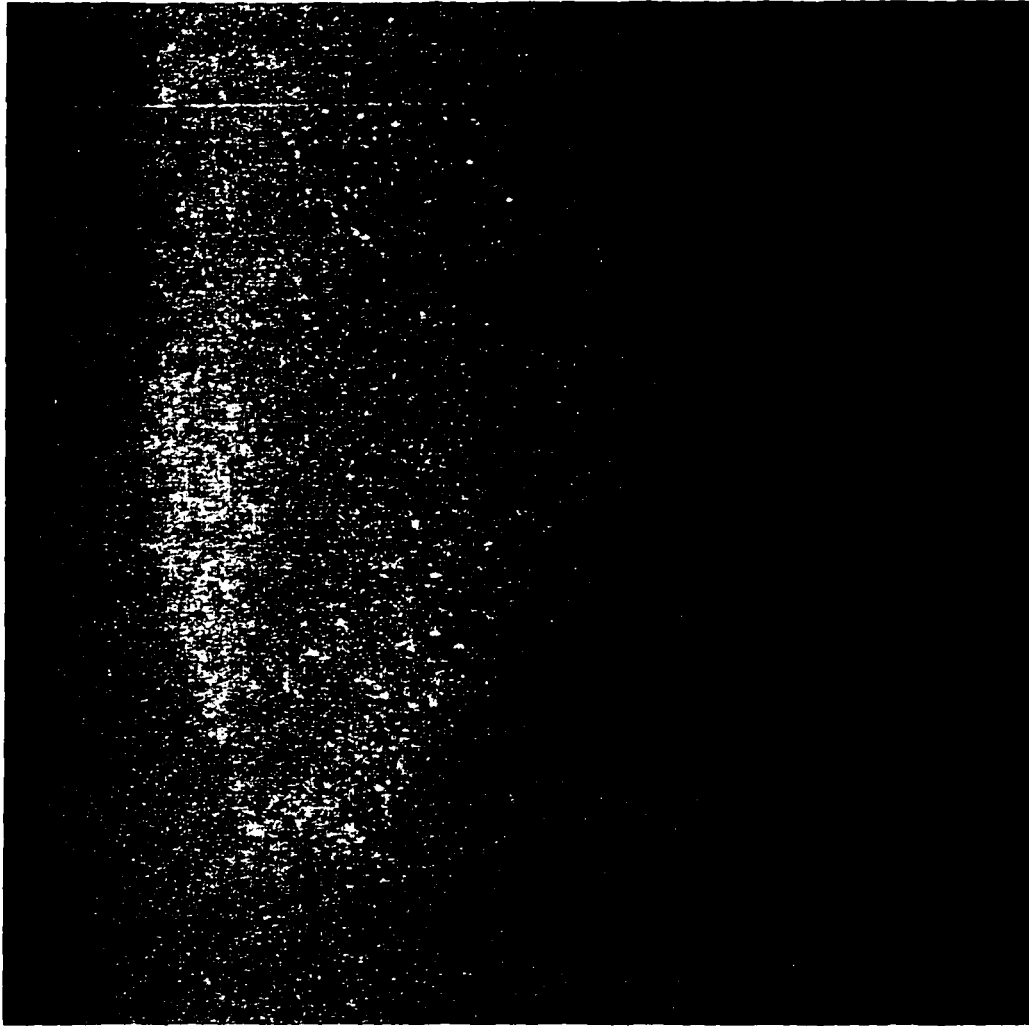
Figure 6.42: Trailing edge of copper electrode. Oxide film visible near center of downstream portion of the electrode. The direction of flow of the electrolyte is out from the page.
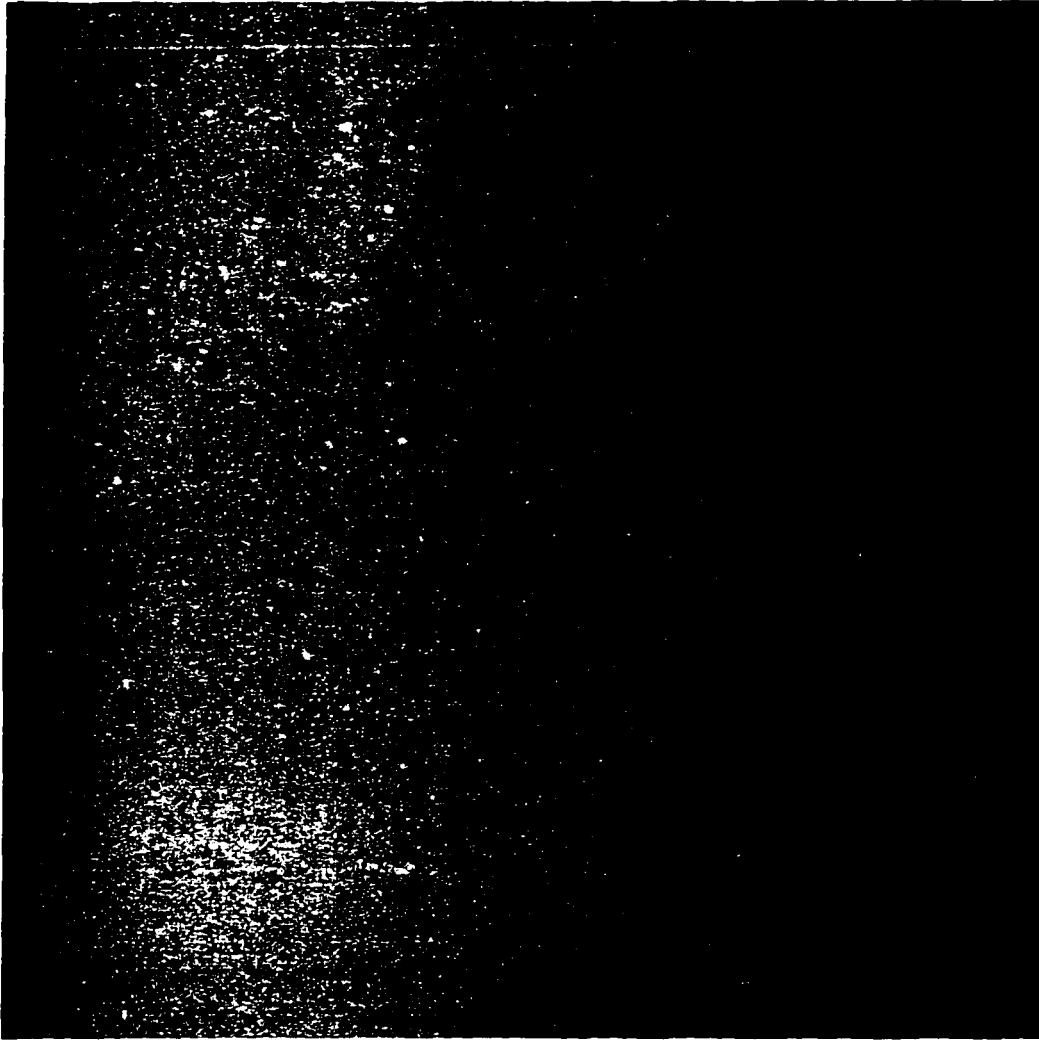
Figure 6.43: Copper electrode with non-uniform oxide film. Image shows areas where the film has adhered to the electrode. The direction of flow of the electrolyte is out from the page.
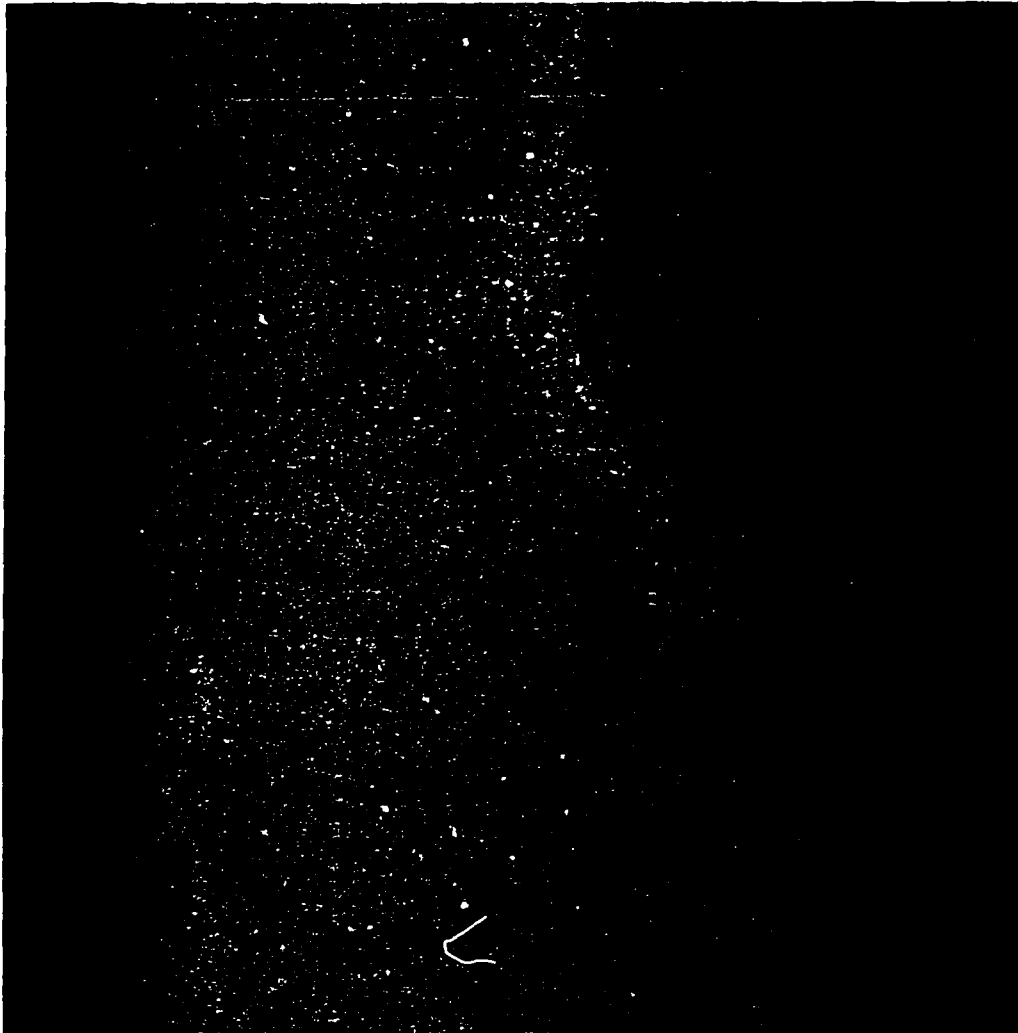
Figure 6.44: Edge of copper electrode normal to electrolyte flow. Transition phase evident at white boundary. Green film visible at left of image which was the trailing edge of the electrode. The direction of flow of the electrolyte is to the left.

Figure 6.45: Copper electrode at the solution air interface. Flow pattern indicated by white band on electrode surface which indicates a velocity reduction near the solution/air interface. The direction of flow of the electrolyte is to the left.

Figure 6.46 : Precipitate collected from bottom of recirculation beaker. Blue-green in color, precipitate was collected in a pipette..
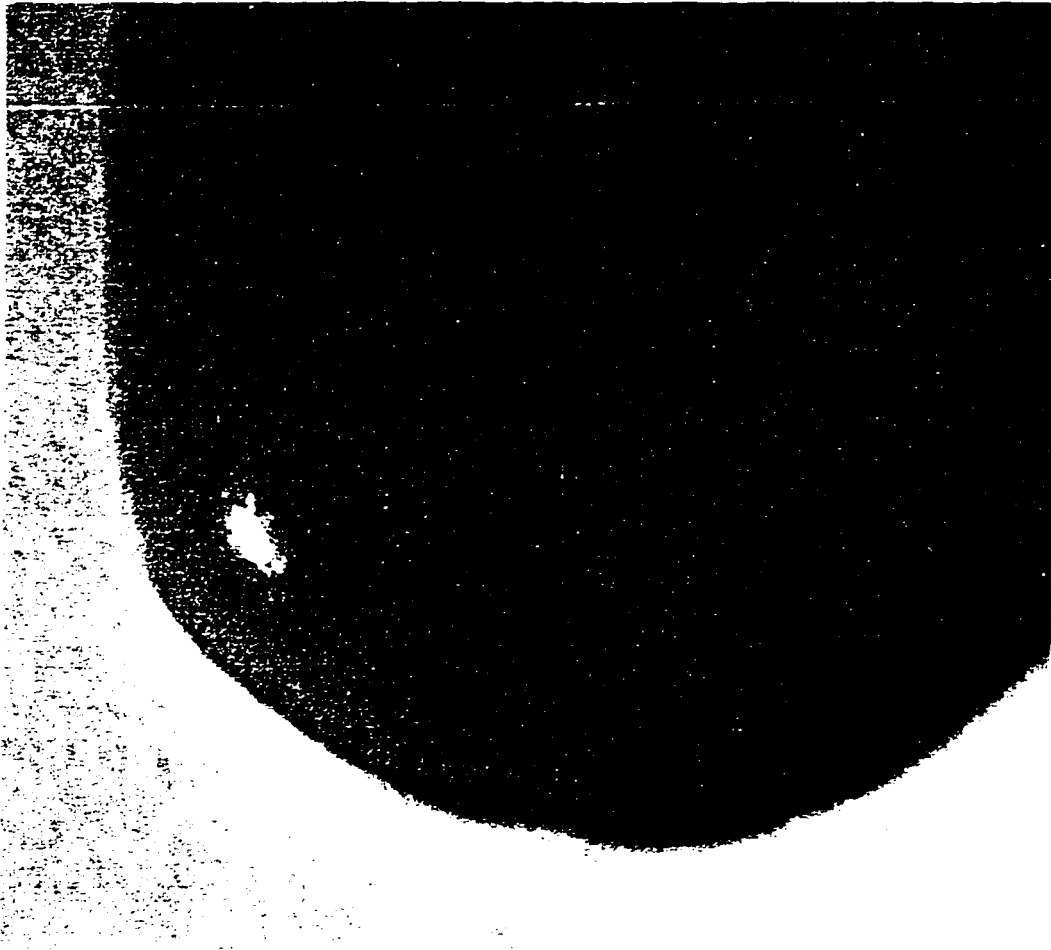
Figure 6.47: Precipitate on sample paper, wet.
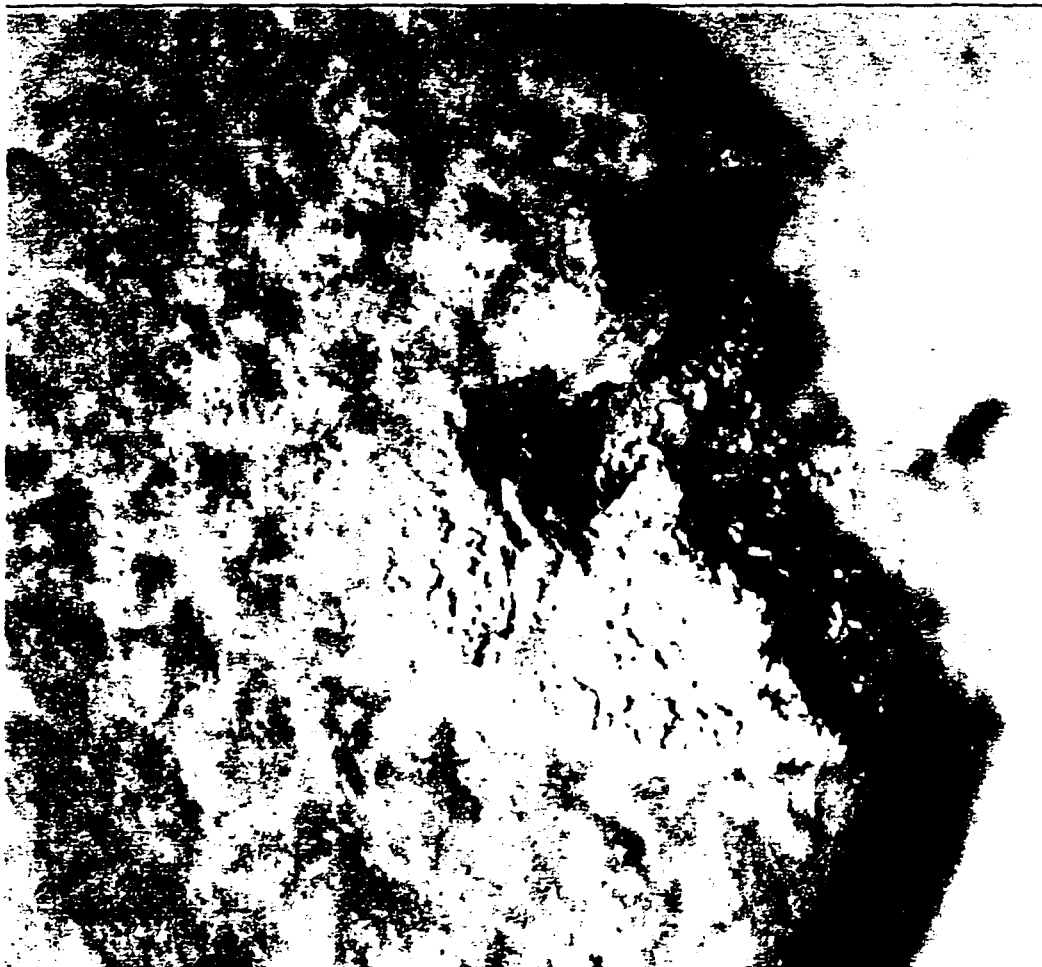
Figure 6.48 : Precipitate on sample paper after air drying.
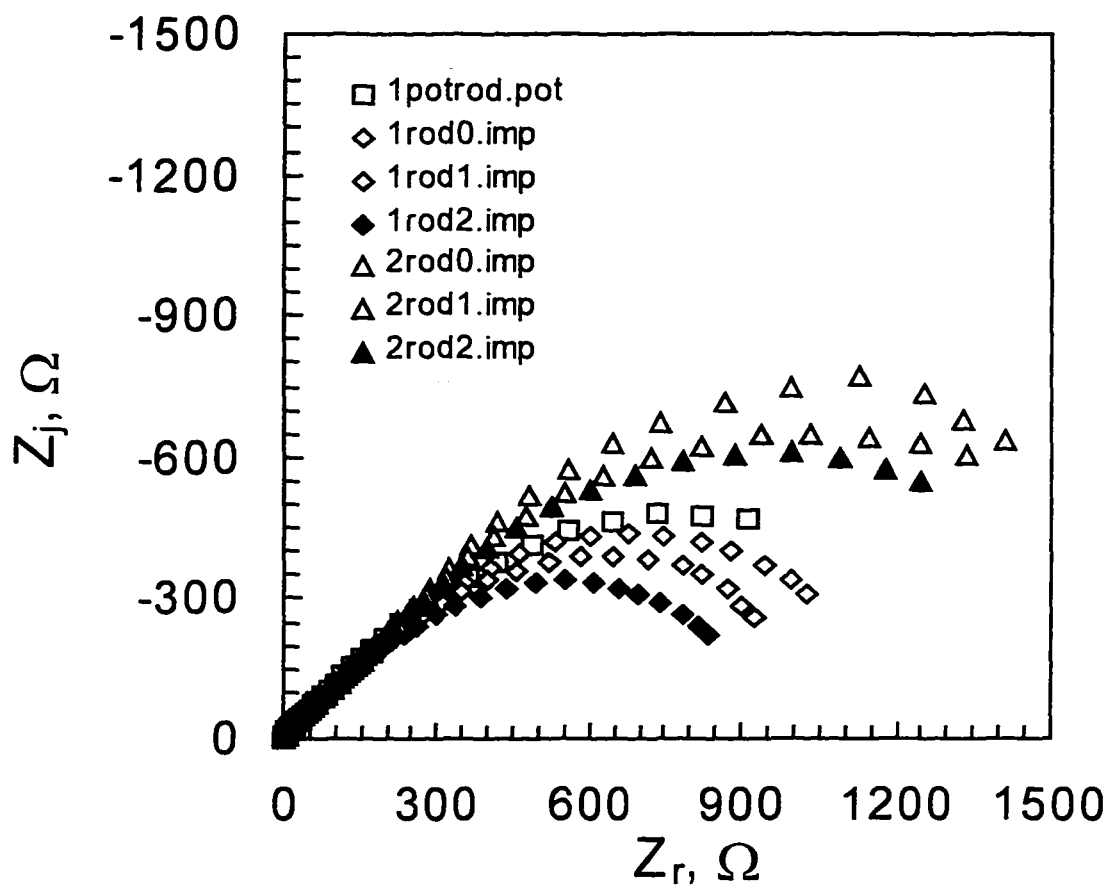
Figure 6.49: VAG impedance scans conducted on each rod. Three consecutive scans were collected on each rod and a general downward trend is seen for both cases. Also plotted is a preliminary potentiostatic scan used in determining experimental parameters.

CHAPTER 7
COMPARISON WITH PAST RESULTS

Efird (1977) stated that there is a critical shear stress for different alloys associated with the mechanical removal of oxide films on the metal surface which leaves the metal unprotected and susceptible to enhanced corrosion. This work suggests a different mechanism for enhanced corrosion. This chapter will describe Efird's experiment, results, and conclusions and compare each to the work conducted for this project.

Commercially available annealed sheets of copper and four copper alloys were investigated in a "full strength sea water" solution. The test apparatus consisted of a sample holder with a rectangular cross section designed so sea water could flow parallel to the surface of the sample. Flow establishment and disengagement regions were located up and downstream respectively form the sample to ensure a well developed flow over the sample and through the exit orifice. The velocity was mathematically calculated using the header pressure and orifice size. Velocities for this work ranged from 1.5 m/s to 15 m/s, although the pure copper was tested at lower velocities due to accelerated corrosion at 1.5 m/s. Temperature and pH control were not implemented; however, the use of fresh rather than recycled sea water reduced the need for control of the electrolyte pH and composition. Alteration in corrosion product film, weight loss, thickness loss and

alteration of metal surface appearance were stated to be used to analyze the samples after testing.

Thirty day exposures of the samples at different velocities were conducted and the sample condition was analyzed. Accelerated corrosion was identified by appearance of the corrosion products and appearance of the metal surface after the corrosion products were removed. The thickness and mass loss measurements proved to be inconclusive in determining a value for the critical shear. Examples of images of the cleaned samples used determine the velocity at which the critical shear was reached are shown in Figure 7.1 (Efird 1977). It should be noted that the onset of enhanced corrosion was consistently located at the leading edge of the coupon. The resulting values for critical velocity and shear are given in Table 7.1.

Shear stress as a function of jet velocity for the experimental work conducted here is presented in Figures 7.2 and 7.3. The curves represent the dimensionless radial position and the horizontal dashed lines represent the critical shear values reported by Efird for pure copper and 70/30 copper nickel. The vertical dotted lines represent the velocities investigated in this work; 1.0, 2.0, 4.0, and 6.2 m/s for copper and 2.0 and 6.0 m/s for 70/30 copper nickel. Other velocities were also investigated. The velocities of interest were those that intersected the dimensionless radial position above and below the reported critical shear for the test material. The velocities that satisfied this criterion for copper were 1.0 and 2.0 m/s, and 6.0 m/s for 70/30 copper/nickel. If in fact a mechanical shear removed the oxide layer on the electrode surface, a distinct difference in the appearance of the electrode surface should be observed past the radial position at which this shear was achieved. A video image of a copper electrode is presented in Figure 7.4.

The copper electrode was immersed in aerated sea water with a velocity of 1.0 m/s for 12 days followed by 2 days at 2.0 m/s. A detailed description of the experimental parameters results is presented in Section 6.5. At a point approximately 1/3 the radius of the electrode from the center, the reported critical shear was reached with the 2.0 m/s jet velocity. An arrow indicates where one would expect the start of erosion-corrosion, which would be marked by visible pitting and non-uniformity on the surface. There was no accelerated corrosion on this surface, and the oxide layer was still intact. Examination of all other electrode surfaces for all runs yielded the same results.

It is apparent from the images in Figure 7.1 that, in Efird's work, an increase in the velocity over a certain value caused enhanced corrosion of the electrode surface. In contrast, the present work included experiments with shear forces on a copper electrode twenty times that of the critical shear value reported by Efird and no erosion corrosion was observed.

Observed in this work was the ability to remove an oxide layer with a small amplitude potential perturbation (i.e. less that 50 mV; see section 6.4). It has also been shown with this work that salt films resulting from an applied potential can be removed by fluid flow (see section 6.2). This removal of salt films on specific parts of the electrode and not on others could further contribute to a potential gradient. Oxygenation cells are another source of potential gradients which could form when using a channel type experimental cell. This leads us to conclude that the enhanced corrosion seen by Efird was not due to a shear removal of an oxide film but to a condition where the film became unstable due to a potential gradient across the electrode surface. The apparatus used by Efird to conduct experiments did not produce a uniform mass transfer to or away

from the electrode surface leading to concentration gradients which could facilitate potential gradients across the surface of the electrode. This could explain the origination of the enhanced corrosion observed at the leading edge of the coupon.

Table 7.1: Critical Velocity and Shear Stress for Copper-Based Alloys in Sea Water (Efird, 1977).

Alloy / main components	Critical Velocity m/s	Temperature C	Critical Shear Stress N/m^2
CA 122 pure copper	1.3	17	9.6
CA 687 copper /zinc	2.2	12	19.2
CA 706 90/10 copper/nickel	4.5	27	43.1
CA 715 70/30 copper/nickel	4.1	12	47.9
CA 722 copper/nickel/chromium	12.0	27	296.9

0.7 m/s　　　1.4 m/s　　　2.1 m/s　　　2.9 m/s
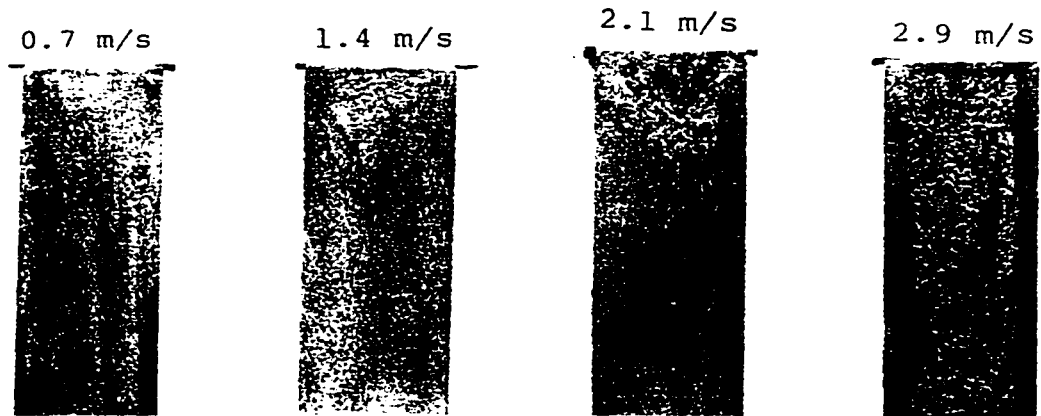
FIGURE 4 — Cleaned samples of CA 122 after 30 days' exposure in 17 C sea water at various velocities. Accelerated corrosion occurred at 1.4 m/s.

1.5 m/s　　　3.0 m/s　　　4.6 m/s　　　6.1 m/s
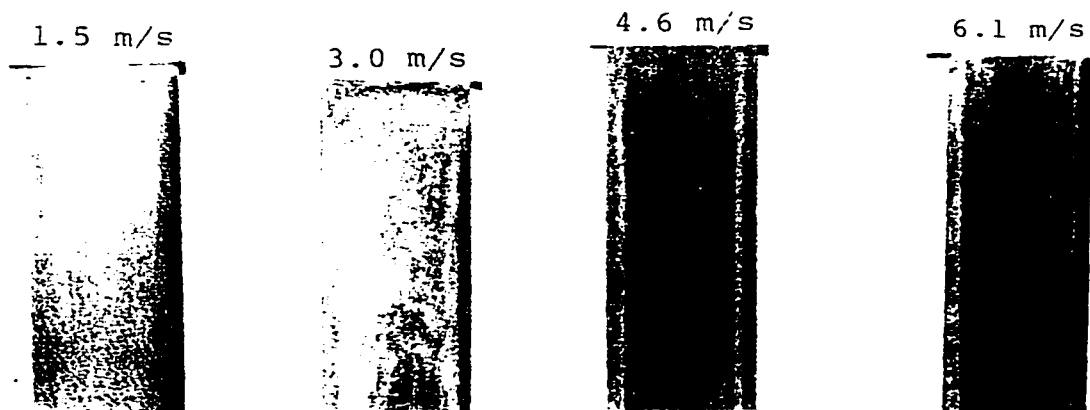
FIGURE 5 — Cleaned samples of CA 687 after 30 days' exposure in 12 C sea water at various velocities. Accelerated corrosion occurred at 3.0 m/s.

1.5 m/s　　　3.0 m/s　　　4.6 m/s　　　6.1 m/s
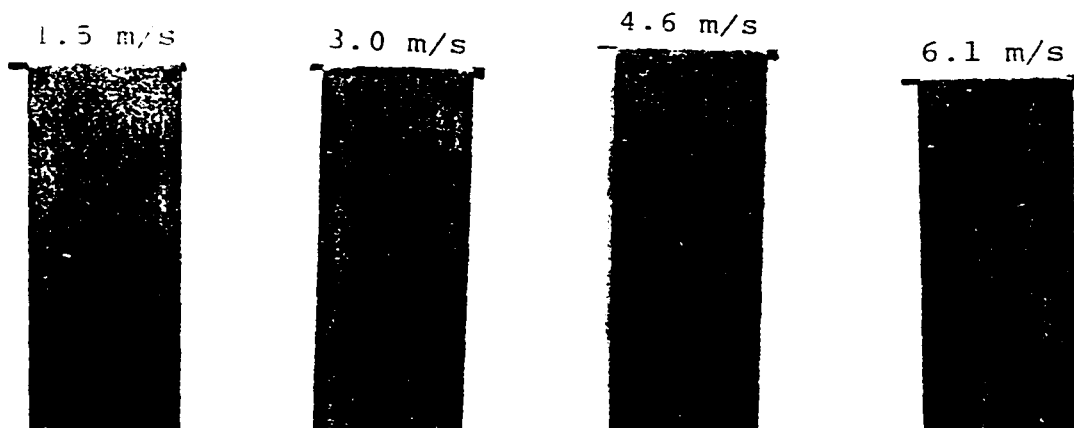
FIGURE 6 — Cleaned samples of CA 706 after 30 days' exposure in 27 C sea water at various velocities. Accelerated corrosion occurred at 4.6 m/s.

Figure 7.1: Cleaned images used to determine critical shear by Efird (1977).
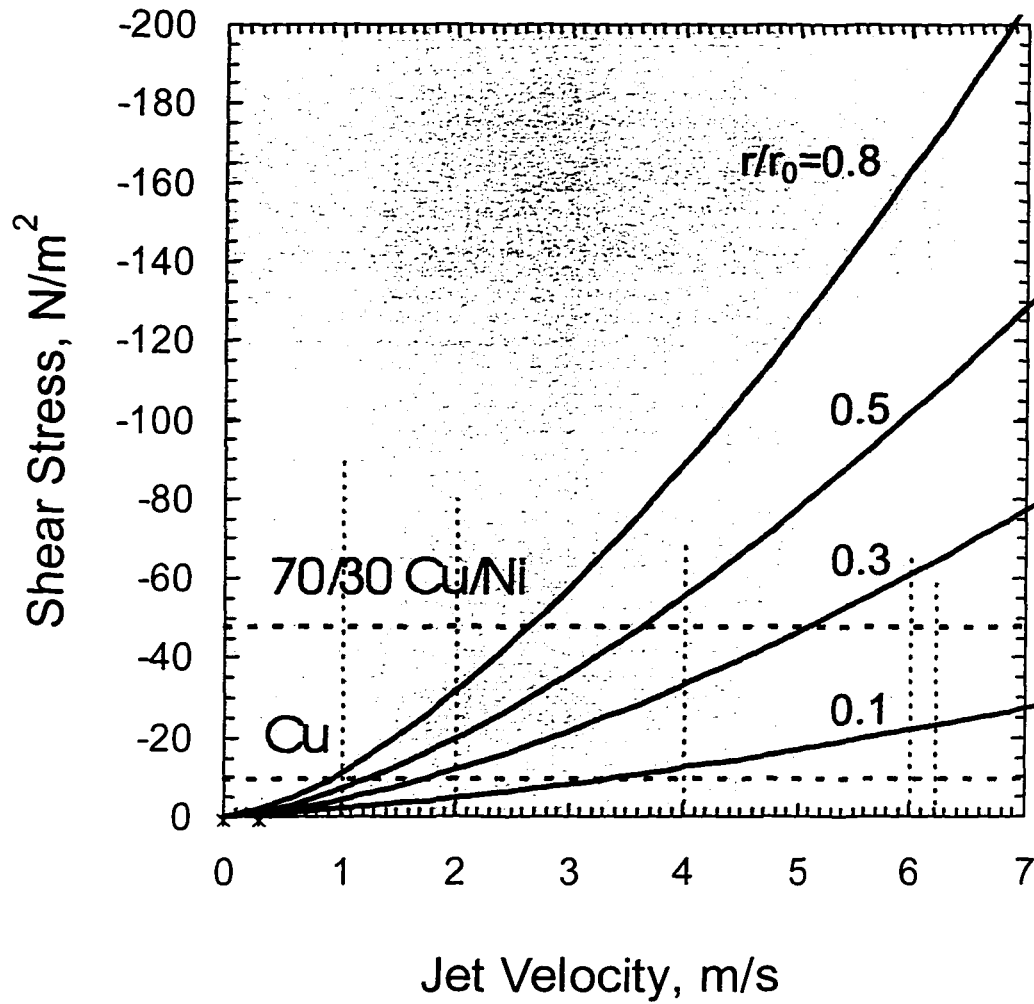
Figure 7.2 Shear stress as a function of jet velocity. Curves indicate dimensionless position on the electrode. Horizontal lines represent reported values for critical shear for copper and 70/30 copper nickel (Efird, 1977).
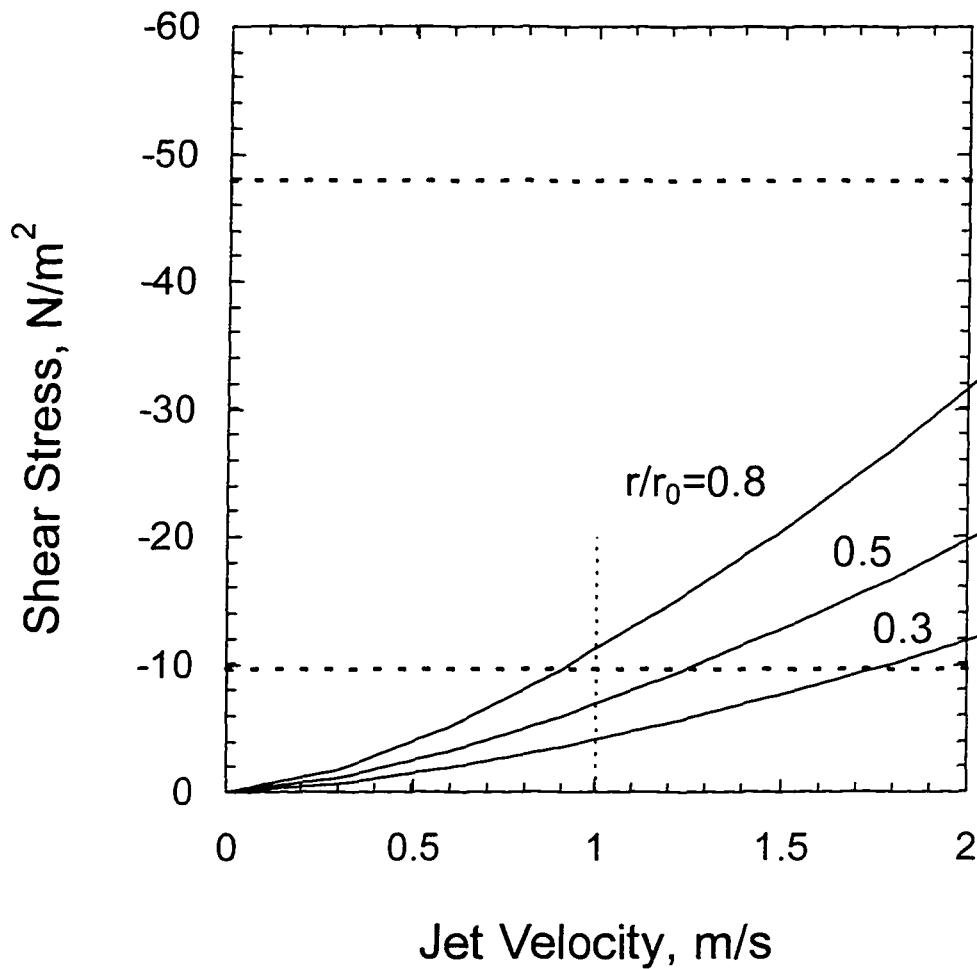
Figure 7.3: Shear stress as a function of jet velocity. Curves indicate dimensionless position on the electrode. Horizontal lines represent reported values for critical shear for copper and 70/30 copper nickel (Efird. 1977).
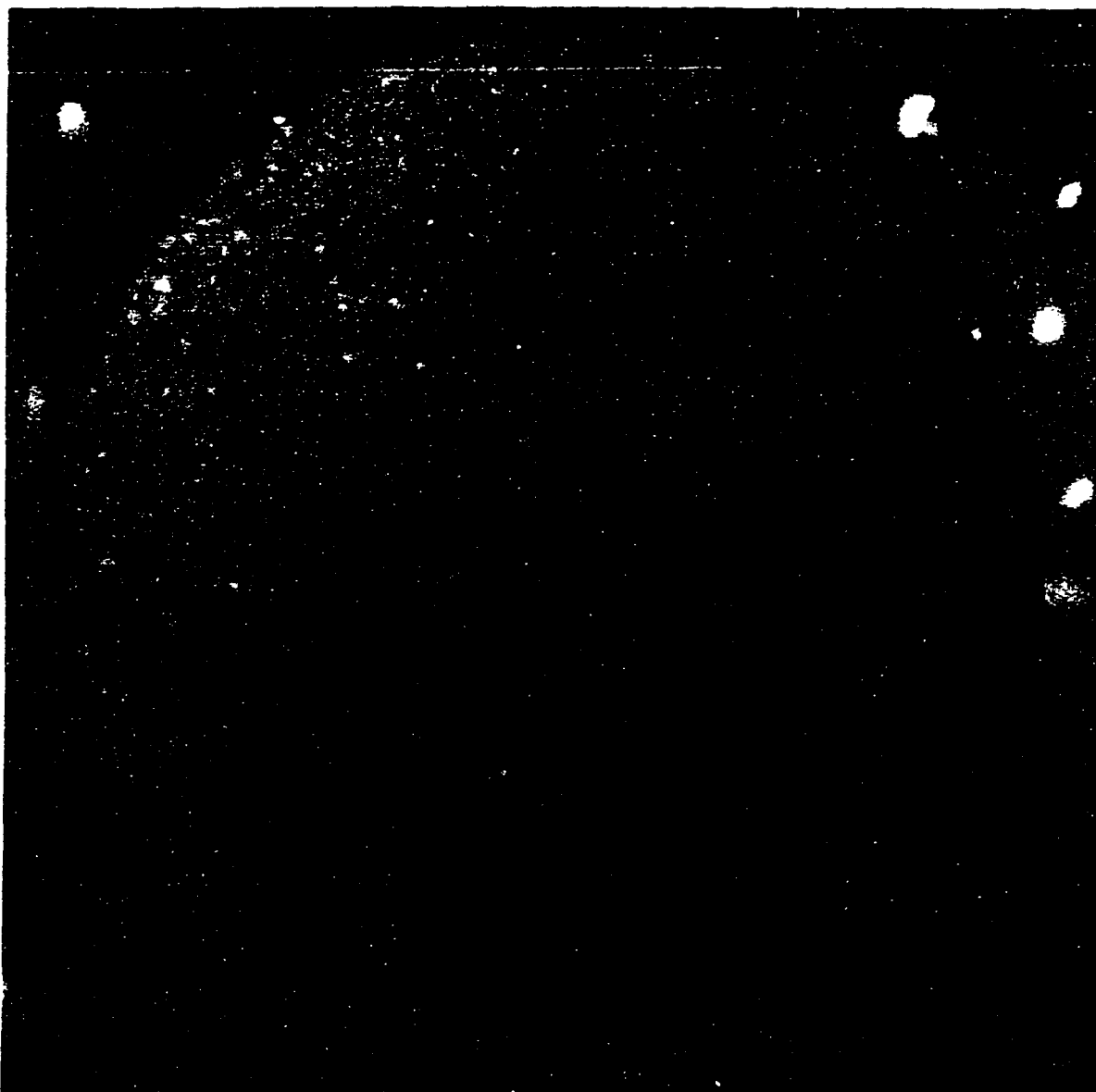
Figure 7.4: Image of pure copper electrode in aerated sea water from experiment discussed in section 6.6. Velocity had been held constant at 2.0 m/s for 44 hours when image was obtained. No indications of enhanced corrosion.

CHAPTER 8
CONCLUSIONS

This work has shown that a protective oxide film on the surface of a copper electrode can be irreversibly modified (on the time frame of several days) by an applied potential perturbation as small as 50 mV. Experiments were conducted which visually showed the formation and shear removal of salt films under an applied anodic potential. The current responses to the applied potential supported the visual events occurring on the electrode surface. The utility of the combination of the impinging jet and video microscope as a powerful tool in assessing shear-induced corrosion was confirmed in this work. Shear stresses twenty times the critical shear reported by Efird did not result in shear removal of oxide films. Concentration gradients driven by localized shear removal of salt films or oxygenation cell could produce potential gradients across a metal surface large enough to destabilize protective films resulting in an enhanced corrosion effect.

The extent of aeration of sea water played a key role in the corrosion behavior of copper. Partially aerated systems were more sensitive to velocity and potential changes than were those with forced aeration (dissolved O_2 = 6.0 and 7.0 ppm respectively). In partially aerated sea water, dissolved CO_2 resulted in a decrease in the local pH near the electrode causing an equilibrium shift which destabilize some of the film components which were seen in sea water aerated with CO_2-free air.

155

The measurement model was shown to be useful in predicting the polarization impedance for copper and copper alloys in sea water. The predicted values correlated well with the experimentally determined values. The measurement model technique was effective in predicting polarization impedances on systems that were difficult to obtain a full impedance spectra.

Impedance spectroscopy has been shown to be a useful tool for the non-invasive evaluation of surface properties of copper and copper based alloys in sea water. However, in order for this technique to be non-invasive, the perturbation must be small and the modulation must not change the steady state characteristics. Galvanostatic regulation is ideally suited for collecting impedance spectra on a corroding metal surface at the corrosion potential. While conventional galvanostatic measurements can result in severe swings in potential, the variable amplitude galvanostatic algorithm described here provides a good means for adjusting the modulation amplitude for current to prevent large perturbations to the system.

Corrosion potential, impedance spectra, and digital images combined to provide insight into the mechanisms of corrosion taking place at the electrode surface. The corrosion potential gave information on the state of the system and the impedance spectra were useful in determining the resistance to corrosion of the electrode material. The digital images provided a record on the evolution of the electrode surface as a function of time. These images indicated whether shear induced preferential corrosion was present. The effects of flow were evident in cases where a uniform mass transfer condition was not maintained and when an applied potential caused the formation of thick salt films, which could be removed by shear forces. Results have proven that even after the

corrosion potential reached a steady state, oxide films continued to form and evolve on the electrode surface resulting in an increase in the magnitude of the impedance over time.

CHAPTER 9
SUGGESTIONS FOR FUTURE WORK

More extensive analytical analysis of corrosion products in the form of surface analysis of the electrode after an experiment or during a phenomena of interest would assist in further understanding this systems reaction kinetics. Evaluation of corrosion products *in situ* could significantly advance this work by supplying empirical data on possible reactions. Sensors are commercially available which have the capability to monitor the concentration of species in a flowing stream. In a re-circulating system such as that of the impinging jet, the implementation of two such sensors, one on the input stream and one on the effluent stream, would supply a concentration difference which could be extrapolated back to give information on reactions and reaction rates.

Development of models to describe potential distributions, concentration gradients, and current distributions of corrosion systems which can be directly applied to a copper/copper alloy system is currently under way within our group. This type of model along with experimental data could lead to predictive techniques for the corrosion rate of copper and copper alloys in a variety of environments. This information could be used as well to predict the performance of other metals. A data base generated from such a model would be valuable in the future selection of materials for a specific corrosive environment.

Quartz microbalance technology could be applied to this work to determine the exact amount of corrosion taking place in-situ. One could immediately see the effects of velocity, light, pH, temperature, and applied potential if the ability to measure mass loss *in situ* was available.

Experimentally determined pH near the electrode surface should be investigated in future work so the stability of corrosion products near the surface could be better understood (Deslouis et al., paper in progress, Moghissi 1993).

Further automation of the experimental process to improve the periodicity of data collection would benefit this project. More frequent collection of digital images of the surface has become possible even since the inception of this project partially because of the vast improvements in mass storage devices for personal computers. Large steps forward have also been taken in the development of faster image acquisition hardware and software. The image grabber board used to collect digital images for this work had a maximum acquisition rate of approximately one frame in 8.0 seconds. Today. image acquisition equipment at comparable prices to that paid for the board used in this work are capable of acquiring images at rates of thirty frames per second.

Control of pH, temperature and other variables, which effect the response of this type system, through the use of a personal computer and a data acquisition interface would improve the data collection process. Multi-plot displays of all parameters of interest would assist in determining direction of a given experiment while the experiment is in progress. The relationship between these parameters could be better analyzed in situ which could result in the guidance of an experiment to collect the desired data in one

experiment where without this interactive adjustment, multiple experiments after post experiment analysis may be necessary.

APPENDIX A
ELECTROCHEMISTRY

Many processes that occur in nature can be studied in the laboratory by supplying the necessary components of the process of interest. For study of a corroding metal, an electrochemical cell can be constructed and a vast range of electrochemical techniques are available to determine corrosion rate, a material's resistance to corrosion, what and how many films form on the electrode surface, and passivation characteristics.

A metal immersed in an electrolyte is an example of an electrochemical system, therefore an understanding of a classical electrochemical cell is essential in the study of copper corrosion. The basic components of a classical electrochemical cell are a cathode, an anode, and an electrolyte. The cathode and anode, which must be electrically connected in order to construct a complete circuit, are often referred to as the counter and working electrodes respectively. For investigative purposes one or multiple reference electrodes can be added to the system to provide a standard from which to measure cell potential.

When a metal comes in contact with an electrolyte, changes on the surface of the metal occur. Metal atoms disassociate with the surface in the form of positive ions, cations, resulting in the production of electrons which are free to move through the metal but are unstable in solution and readily combine with positively charged ions. The

cation can adsorb to the surface of the metal. In a classical electrochemical cell the free electron moves through the electrical connection in the form of an electrical current to the counter electrode where it produces an overall negative charge. Current generated by the disassociation of electrons in a metal in solution is known as Faradaic current. Mass loss of a metal in solution is proportional to the Faradaic current, therefore the corrosion rate can be determined by measuring the Faradaic current.

Measuring current is usually easier in-situ than measuring mass loss. although both are possible. The cation can desorb into solution and will diffuse toward the counter electrode where it will react with available electrons and precipitate or adhere to the electrode surface. The desorption of the cation into solution constitutes the process of corrosion on the surface of the working electrode and with this process comes loss of mass of the working electrode. In order for the corrosion process to readily occur, the anode and cathode must be composed of different metals. The electromotive force, EMF, of the metal dictates which electrode will become the cathode and which will become the anode. The EMF is defined as the difference in potential between two dissimilar metals immersed in the same electrolyte or otherwise ionically connected (Parker 1994) or that which causes a flow of current (Weast 1984). The potential difference between a metal and a reference electrode such as the standard hydrogen electrode, SHE, is known as the standard electrode potential. Some examples of several standard electrode potentials versus a SHE are given in Table 2.1 (Bard & Faulkner 1980).

Another example of an electrochemical system is that of two dissimilar metals in contact with each other and an electrolyte. This situation is known as a galvanic coupling. Consider copper and zinc metals joined and immersed in an electrolyte. In this system the

copper is the more noble metal, therefore the zinc exhibits corrosion while the copper serves as the cathode. The zinc is often used as a sacrificial anode to protect a buried or immersed metallic structure.

When a single homogeneous metal is immersed in as electrolyte with no external electrical connection, an interesting situation typically occurs. Because the free electrons have no path to follow a negative charge builds up in the interior of the electrode, counteracted by positively charged ions on the surface of the electrode. The negative and positive charges balance following the law of conservation of charge, therefore Poisson's equation reduces to Laplace's equation

$$\nabla^2 \Phi = 0 \qquad\qquad (A1)$$

where Φ is the electric potential. As the positive ions build up on the surface of the electrode a net positive charge at the surface develops which is not completely offset by the internal negative charges, therefore negative ions, anions, diffuse toward the positively charged surface and form a layer of predominantly negatively charged ions. The positive charge on the surface is fixed, however, the layer of predominantly negatively charged ions are free to move and relocate. This mobile layer is known as the diffuse double layer. The diffuse double layer acts as an electrolytic capacitor and it can be charged and discharged (Newman 1973). If the double layer behaves as a perfect capacitor the capacitance of the double layer, C_{dl}, can be used to determine the charging current, i_c utilizing the relation

$$C_{dl} = \frac{q}{E}. \qquad\qquad (A2)$$

where q is the charge on the double layer and E is the potential across the double layer. The charging current is then determined using Ohm's law. Under these conditions, no chemical reaction takes place, therefore no corrosion process are present. If corrosion processes are present, the total current i_T, consists of the sum of the charging current and the Faradaic current (Bard & Faulkner 1980).

$$i_T = i_c + i_f .$$ <div align="right">(A3)</div>

Copper immersed at the corrosion potential in a solution with oxidizing agents but no external path for electron flow can still corrode through the establishment of local cathode and anode sites.

APPENDIX B
TIME SUMMARIES

Appendix B contains time summaries for experiments presented in Chapter 6.

Information in this section includes times tables corresponding to impedance spectra,

corrosion potential measurements, and video images. The main purpose is to provide

a reference time scale for future work with the data presented.

Table B1: Summary of experimental events for data presented in Section 6.3.

Exp, Exq, Exr, flo data Time Frame Information

7/16/96 12:12 experiment start time

data sets involved
exp, exq, exr, flo

hour	to	data sets	analysis	
0	4.6	exp	Ecorr, Z	
21	29	exq	Ecorr, Z	
47	158	exr	Ecorr, Z	
557	797	flo	Ecorr, Z	Rpol

	image	hour	figure		7/16/96 17:21	exp3.tif	5.15
7/16/96 10:53	exp1.tif	-1.32	11		7/18/96 14:57	exp5.tif	50.75
7/23/96 13:20	exp6.tif	169.13	12				
8/8/96 10:32	exp7.tif		13				
8/8/96 16:59	exp8.tif		14 b-4 flow				
8/8/96 17:00	exp9.tif		15 after flow				
8/13/96 11:25	exp12.tif	671.22	16				
8/19/96 9:55	exp14.tif	813.72	17				

date/time	time, hrs	event
7/16/96 12:12	0	experiment start time
7/23/96 13:20	169	flow suspended
8/8/96 10:30	550	conduct series of Z scans and image grabs until potential application
8/8/96 16:35	556	applied potential of >-1.3 volts
8/8/96 17:00	557	flow initiated, v = 1m/s
8/8/96 17:25	557	resumed standard collection of Ecorr and Z
8/15/96 10:22	718	pH change from 8.06 to controlled 8.24
8/16/96 10:11	742	velocity change from 0.6 to 3.4 gal/min

Table B1 cont.

experiment start time	data sets involved
7/16/96 12:12	exp, exq, exr, flo

hour	to	data sets	analysis
0	4.6	exp	Ecorr, Z
21	29	exq	Ecorr, Z
47	158	exr	Ecorr, Z
557	797	flo	Ecorr, Z Rpol

	image	hour			
			5	-240	0.21454861
			5	-360	0.21454861
7/16/96 10:53	exp1.tif	-1.32	51	-240	2.11454861
7/16/96 17:21	exp3.tif	5.15 *	51	-360	2.11454861
7/18/96 14:57	exp5.tif	50.75	169	-240	7.0471875
7/23/96 13:20	exp6.tif	169.13 *	169	-360	7.0471875
8/13/96 11:25	exp12.tif	671.22 *	671	-240	27.9673264
8/19/96 9:55	exp14.tif	813.72 *	671	-360	27.9673264
			814	-240	33.9048264
			814	-360	33.9048264

169	-200
169	-300
169	-360
557	-200
557	-300
557	-360
718	-200
718	-300
718	-360
742	-200
742	-300
742	-360

Table B2: Summary of experimental events for data presented in Section 6.4.

RC data Time Frame Information

experiment start time			6/10/94 10:43 AM		
velocity change 1.99 to 5.96 m/s time to velocity change			6/14/94 10:28 AM		
			95.75 hours		
			3.99 days		

		g:\ptw\data sets\a 6-94\OCDATA\			
Data files	Ecorr	rc1.oc			
		rc2.oc			
		rc3.oc			
		rc4.oc			from start	from velocity change

		g:\ptw\data sets\a 6-94\		hours	
	Impedance	rc2.imp	6/10/94 14:48	4.09	-91.66
		rc3.imp	6/10/94 16:50	6.12	-89.63
		rc4.imp	6/13/94 10:38	71.93	-23.82
		rc5.imp	6/13/94 15:11	76.47	-19.28
		rc6.imp	6/14/94 9:38	94.92	-0.83
		rc7.imp	6/14/94 14:14	99.52	3.77
		rm1.imp	6/14/94 21:52	107.15	11.40
		rc8e1.imp	6/15/94 12:09	121.44	25.69
		rc9a1.imp	6/16/94 10:44	144.02	48.27

		g:\ptw\data sets\a 6-94\OLDIMAGES\			
	Images	rc6m.tif	6/13/94 15:29	76.77	-18.98
		rc7m.tif	6/14/94 10:07	95.40	-0.35
		rc8m.tif	6/15/94 11:46	121.05	25.30

Table B3: Summary of experimental events for data presented in Section 6.5.

70/30 Cu/Ni data Time Frame Information

				from start hours	
experiment start time			12/6/95 14:22		
temperature change 25C to 28C			12/14/95 14:30	192.13	
velocity change 1.99 to 5.96 m/s			12/17/95 18:40	268.29	
NI experiment lock up			12/14/95 21:34		
Ecorr last point			9/16/96 2:57		
		g:\ptw\data sets\o 12-95 nickel\			
Data files	Ecorr	ni.oc	12/6/95 14:22		
		nk.oc	12/17/95 19:28		

				from start hours	from velocity change
		g:\ptw\data sets\o 12-95 nickel\			
	Impedance	ni0a.imp	12/6/95 15:40	1.29	-267.00
		ni13c.imp	12/7/95 14:14	23.86	-244.43
		ni19a.imp	12/8/95 18:03	51.68	-216.62
		ni22c.imp	12/9/95 16:12	73.83	-194.47
		ni25b.imp	12/10/95 16:10	97.79	-170.50
		ni28b.imp	12/11/95 19:50	125.46	-142.83
		ni30b.imp	12/12/95 14:20	143.96	-124.33
		ni33a.imp	12/13/95 16:53	170.51	-97.78
		ni35a.imp	12/14/95 17:22	194.99	-73.30
		ni36a.imp	12/14/95 20:00	197.63	-70.67
		ni36b.imp	12/14/95 20:44	198.36	-69.93
		ni36c.imp	12/14/95 21:34	199.19	-69.10
		nk0a.imp	12/17/95 20:46	270.39	2.10
		nk0b.imp	12/17/95 21:04	270.69	2.40
		nk0c.imp	12/17/95 21:38	271.26	2.97
		nk1a.imp	12/17/95 23:46	273.39	5.10
		nk1b.imp	12/18/95 0:05	273.71	5.42
		nk1c.imp	12/18/95 0:39	274.28	5.98
		nk4a.imp	12/18/95 8:40	282.29	14.00
		g:\ptw\data sets\a 6-94\OLDIMAGES\			
	Images	wet.tif	12/6/95 13:36	-0.77	-269.07
		nc9.tif	12/10/95 0:30	82.13	-186.17
		nc14.tif	12/14/95 23:50	201.46	-66.83

Table B4: Summary of experimental events for data presented in Section 6.6.

Copper (x**.imp) Time Frame Information

			hours from start	
experiment start time		6/21/95 10:13		
velocity changes	gal/min			
	0.5 to 1	7/3/95 12:10	289.95	
	1 to 2	7/5/95 14:10	339.95	
	2 to 3.2	7/6/95 13:55	363.70	
		g:\ptw\data sets\m 7-95 hope\8IMPDATA\raw data\		
Data files	Ecorr	hope.oc	6/21/95 10:13	0.00
		suz.oc	6/23/95 10:10	47.96
		x.oc	6/30/95 13:33	219.33

				from velocity change
		g:\ptw\data sets\m 7-95 hope\8IMPDATA\		
Impedance	x013A.imp	7/2/95 10:02	263.82	289.95
	x039A.imp	7/5/95 0:12	325.99	339.95
	x056A.imp	7/6/95 13:39	363.44	363.70
	x057A.imp	7/6/95 15:29	365.28	
	x078A.imp	7/11/95 6:30	476.29	
		g:\ptw\data sets\m 7-95 hope\8IMPDATA\		
Images	h24.tif	7/3/95 11:17	289.07	
	h25.tif	7/3/95 0:30	278.28	
	h26.tif	7/5/95 9:20	335.12	
	h27.tif	7/5/95 15:50	341.62	
	h28.tif	7/6/95 0:58	350.75	
	h29.tif	7/7/95 10:35	384.37	
	h30.tif	7/10/95 9:45	455.53	

REFERENCES

Agarwal. P., *Application of Measurement Models to Impedance Spectroscopy*, Ph.D. Dissertation. University of Florida, Gainesville, Florida, 1994.

Agarwal, P., Crisalle O. D., Orazem M. E., and García-Rubio L. H., "Application of measurement models to impedance spectroscopy. II. Determination of the stochastic contribution to the error structure," *Journal of the Electrochemical Society*, **142** (1995a). 4149-4158.

Agarwal, P., Moghissi, O. C., Orazem, M. E., García-Rubio, L. H., "Application of Measurement Models for Analysis of Impedance Spectra," *Corrosion*, **49** (1993a), 278-289.

Agarwal, P., Orazem M. E., García-Rubio L. H., "Measurement Models for Electrochemical Impedance Spectroscopy I. Demonstration of Applicability," *Journal of the Electrochemical Society*, **139** (1992), 1917-1927.

Agarwal, P., Orazem, M.E., Garcia-Rubio, L.H., "Application of the Kramers-Kronig Relations in Electrochemical Impedance Spectroscopy," Electrochemical Impedance: Analysis and Interpretation, ASTM STP 1188, Philadelphia (1993b), 115-139.

Agarwal P., Orazem M. E., García-Rubio L. H., "Application of Measurement Models to Impedance Spectroscopy. III. Evaluation of Consistency with the Kramers-Kronig Relations," *Journal of the Electrochemical Society*, **142** (1995b). 4159-4168.

Alkire, R.C., "Special Review: Transport Processes in Electrochemical Systems," *Chemical Engineering Communications*, **38** (1985), 401-413.

Alkire, R., Cangellari, A., "Formation of Salt Films During Anodic Metal Dissolution in the Presence of Flow," *Journal of the Electrochemical Society*, **130** #6 (1983). 1252-1259.

Alkire, R.C., Perusich, S., "The Effect of Focused Ultrasound on the Electrochemical Passivity of Iron in Sulfuric Acid," *Corrosion Science*, **23** (1983), 1121.

Bacarella, A.L., Griess, J.C. "The Anodic Dissolution of Copper in Flowing Sodium Chloride Solutions Between 25° and 175 C°" *Journal of the Electrochemical Society*, **120** (1973), 459.

Barcia, O.E., Mattos, O.R., Pebere, N, Tribollet, B. "Mass-Transport Study of the Electrodissolution of Copper in 1*M* Hydrochloric Acid Solution by Impedance," *Journal of the Electrochemical Society*, **140** #10 (1993), 2825.

Bard, A.J., Faulkner, L. R., *Electrochemical Methods Fundamentals and Applications*, John Wiley and Sons, Inc. New York (1980).

Bianchi, G., Longhi P. "Copper in Sea-Water, Potential-pH Diagrams," *Corrosion Science* **13** (1973), 853-864.

Bird R. B., Stewart W. E., Lightfoot E. N., *Transport Phenomena*, John Wiley and Sons, Inc., New York, (1960).

Bjorndahl, W.D., Nobe, K. "Copper Corrosion in Chloride Media. Effect of Oxygen," *Corrosion* **40** #2 (1984), 82-87.

Butler, J.A.V. *Transactions of the Faraday Society*, **19**, (1924) 729-734.

Chang, Y.C., Prentice, G., "Calculation of pH Near the Surface of an Electrode Covered with a Porous Film," *Electrochimica Acta*, **31** #5 (1986), 579.

Charrière, E., "Image Analysis of Growing Copper Films in Seawater," *Diploma Project 1996-1997*, Swiss Federal Institute of Technology, LMCH, Electrochemical Group, University of Florida, Gainesville, Florida (1997).

Chin, D-T., Tsang, C-H. "Mass Transfer to an Impinging Jet Electrode," *Journal of the Electrochemical Society*, **125** (1978), 1461.

Cogger, N.D. "An Introduction to Electrochemical Impedance Measurements," Technical Report # 006/83, Solartron Instruments, Hampshire, England (1983).

Cogger, N.D. "The Measurement of Signals from Electrochemical Phenomena," Technical Report # 014/84, Solartron Instruments, Hampshire, England (1984).

Copson, H.R. "Effects of Velocity on Corrosion," *Corrosion*, **16** #2 (1960), 86t.

Dawson, J.L., Shih, C.C., Miller, R.G., Palmer, J.W., "Inhibitor Evaluations Under Controlled Hydrodynamic Shear," *Materials Performance*, **30** (1991), 43.

D'Elia, D, Barcia, O.E., Mattos, O.R., Pebere, N, Tribollet, B. "High-Rate Copper Dissolution in Hydrochloric Acid Solution," *Journal of the Electrochemical Society*, **143** #3 (1996), 961.

Dhar, H.P., White, R.E., Darby, R., Cornwell, L.R., Griffin, R.B., Burnell, G., "Corrosion of Cu and Cu-Ni Alloys in 0.5M NaCl and in Synthetic Seawater," *Corrosion*, **41** (1985), 317.

De Sanchez, S.R., Schiffrin, D.J. "The Use of High Speed Rotating Disc Electrodes for the Study of Erosion-Corrosion of Copper Base Alloys in Sea Water," *Corrosion Science*, **28** #2 (1988), 141

Deslouis, C., Frateur, O., Maurin, G., Tribollet, B., "Interfacial pH Measurement During the Reduction of Dissolved Oxygen in a Submerged Impinging Jet Cell," paper in progress.

Deslouis, C., Tribollet, B., Mengoli, G., Musiani, M. "Electrochemical Behavior of Copper in Neutral Aerated Chloride Solution. I. Steady-State Investigation," *Journal of Applied Chemistry*, **18** (1988a), 374.

Deslouis, C., Tribollet, B., Mengoli, G., Musiani, M. "Electrochemical Behavior of Copper in Neutral Aerated Chloride Solution. II. Impedance Investigation," *Journal of Applied Chemistry*, **18** (1988b), 384.

Diem, C.D., "The Influence of Velocity on the Corrosion of Copper in Alkaline Chloride Solutions," Ph.D. Thesis, University of Virginia, Charlottesville (1990).

Diem, C.B., Orazem, M.E., "Influence of Velocity on Corrosion of Copper in Alkaline Chloride Solutions," *Corrosion*, **50** #4 (1994), 290.

Efird, K.D. "Potential-pH Diagrams for 90-10 and 70-30 Cu-Ni in Sea Water," *Corrosion*, **31** #3 (1975) 77.

Efird, K.D. "Effects of Fluid Dynamics on the Corrosion of Copper-Based Alloys in Sea Water," *Corrosion*, **33** (1977), 3-8.

EG&G Princeton Applied Research, "Model 273 Potentiostat/Galvanostat," Operation Manual (1985).

EG&G Princeton Applied Research, "Electrochemical Impedance Measurements: Instrumentation and Techniques," Application Note AC-3, NJ (1989).

Esteban, J.M., Hickey, G.S., Orazem, M.E., "The Impinging Jet Electrode: Measurement of the Hydrodynamic Constant and Its Use for Evaluating Film Persistency," *Corrosion*, **46** #11 (1990), 896-901.

Faita, G., Fiori, G., Salvadore, D. "Copper Behavior in Acid and Alkaline Brines-I. Kinetics of Anodic Dissoulution in 0.5 M NaCl and Free-Corrosion Rates in the Presence of Oxygen," *Corrosion Science*, **25** (1975), 383.

Fiori, G., Casola, S., Faita, G. "Copper Behavior in Acid and Alkaline Brines. II. Formation of a Protective Layer in Slightly Alkaline 0.5 M NaCl Solutions," *Materials Chemistry*, **2** (1977), 5.

Fontana, M. G., *Corrosion Engineering*, McGraw-Hill Book Co., New York. (1986).

Gabrielli, C., "Identification of Electrochemical Processes by Frequency Response Analysis," Technical Report #004/83, Solartron Instruments, Hampshire, England (1980).

Gabrielli, C., "Use and Application of Impedance Techniques," Technical Report, Schlumberger Technologies, Hampshire, England (1990).

Gabrielli, C., Huet, F., Keddam, M., "Investigation of Electrochemical Processes by an Electrochemical Noise Analysis. Theoretical and Experimental Aspects in Potentiostatic Regime," *Electrochimica Acta*, 31 #8 (1985), 1025.

Gan, E.C., Orazem, M.E. "A Mathematical Model for the Corrosion of Iron in Sulfuric Acid," *Journal of the Electrochemical Society*, 134 (1986), 1357.

Gehring, G.A. Jr. "Seawater Corrosion," *Materials Performance*, (September, 1987), 9.

Gilbert, P.T., "A Review of Recent Work on Corrosion Behavior of Copper Alloys in Sea Water," *Materials Performance*, 21 (1982), 47.

Gilbert, P.T., LaQue, F.L. "Jet Impingement Tests," *Journal of the Electrochemical Society*, 101 #9 (1954), 448.

Giralt F., Trass O. "Mass Transfer From Crystalline Surfaces in a Turbulent Impinging Jet Part I. Transfer by Erosion," *Canadian Journal of Chemical Engineering*. 53 (1975), 505.

Goodman, P.D., "Effect of Chlorination on Materials for Sea Water Cooling Systems: A Review of Chemical Reactions," *British Corrosion Journal*, 22 #1 (1987), 56.

Hack, H.P., Gudas J. P., "Inhibition of Sulfide-Induced Corrosion by Clean Seawater Pre-exposure," Report DTNSRDC/SME-79-85, David Taylor Naval Ship Research and Development Center, Annapolis, MD (1979).

Hack H.P., Pickering H.W., "AC Impedance Study of Cu and Cu-Ni Alloys in Aerated Salt Water," *Journal of the Electrochemical Society*, 138 (1991), 690.

Hack H.P., Scully J. R. "Galvanic Corrosion Prediction using Long- and Short-term Polarization Curves," *Corrosion*, 45 #2 (1986), 79.

Hartt, W.H., Culberson, C.H., Smith, S.W. "Calcareous Deposits on Metal Surfaces in Seawater: A Critical Review," *Corrosion* , 40 #11 (1984), 609

Heitz, E., "Chemo-Mechanical Effects of Flow on Corrosion," *Corrosion*. 47 (1991), 135.

Ives, D.H., Rawson, A.E. "Copper Corrosion III. Electrochemical Theory of General Corrosion," Journal of the Electrochemical Society, **109** (1962) 458.

Kauffman, A.M., "Understanding Electrochemical Cells," Technical Report # 017/85, Solartron Instruments, Hampshire, England (1985).

Kendig, M. W., Allen, A. I. , Mansfeld F., "Optimized Collection of AC Impedance Data," *Journal of the Electrochemical Society.* **131** (1984), 935.

Lal, H., Thirsk. H.R. "The Anodic Behavior of Copper in Neutral and Alkaline Chloride Solution," *Journal of the Chemical Society*, **3** (1953), 2638.

LaQue F. L., "Theoretical Studies and Laboratory Techniques in Sea Water Corrosion Testing Evaluation," *Corrosion.* **13** (1957), 303t.

LaQue, F., *Marine Corrosion: Causes and Prevention.* John Wiley and Sons, New York (1975).

Law C.G. Jr., Newman J., "Corrosion of a Rotating Disk in Laminar, Transition, and Fully Developed Turbulent Flow," *Journal of the Electrochemical Society*, **133** (1986), 37.

Lee, H.P., Nobe, K. "Kinetics and Mechanisms of Cu Electrodissolution in Chloride Media," *Journal of the Electrochemical Society*, **133** (1986), 2035.

Macdonald, J.R., *Impedance Spectroscopy*, John Wiley and Sons, New York (1987)

Major Analytical Instrumentation Center (MAIC), Analytical Techniques Handbook. University of Florida, Gainesville (1997).

Mansfield, F., Little, B. "Microbiologically Influenced Corrosion of Copper-Based Materials Exposed to Natural Seawater," *Electrochimica Acta*, **37** #12 (1992), 2291

Moghissi, O.C., *The Electrochemical Behavior of Copper in Chloride Solutions*, PhD dissertation, University of Florida, Gainesville, (1993).

Newman, J.S., *Electrochemical Systems*, Prentice Hall, Inc., Englewood Cliffs, NJ (1973).

Orazem, M.E., Agarwal, P., Jansen, A.N., Wojcik, P.T., and Garcia-Rubio, L.H., "Development of Physico-Chemical Models for Electrochemical Impedance Spectroscopy," *Electrochimica Acta*, **38** (1993), 1903-1911.

Orazem, M.E., Esteban, J.M., Moghissi, O.C., "Practical Applications of the Kramers-Kronig Relations," *Corrosion*, **47** (1991),3.

Parker, S., ed., *McGraw-Hill Dictionary of Scientific and Technical Terms*, 5th ed. McGraw Hill Book Company, New York (1994).

Perry, J.H., *Chemical Engineers' Handbook*, McGraw Hill Book Company, New York. (1963)

Phipps, J. B., Gyory, J. R., "Transdermal Ion Migration," *Advanced Drug Delivery Reviews*, 9 (1992) 137-176.

Pourbaix, M., *Atlas of Electrochemical Equilibria in Aqueous Solutions*, NACE, Houston, Texas (1974).

Pyun, C.H., Park, S.M., "In Situ Spectro-electrochemical Studies on Anodic Oxidation of Copper in Alkaline Solution," *Journal of the Electrochemical Society*, 133 #10 (1986), 2024-2030.

Scholtz T., Trass O. "Mass Transfer in a Non-uniform Impinging Jet Part I. Stagnation Flow-Velocity and Pressure Distribution," *AIChE Journal*, 16 #1 (1970), 82.

Scholtz T., Trass O. "Mass Transfer in a Non-uniform Impinging Jet Part II. Boundary Layer Flow-Mass Transfer," *AIChE Journal*, 16 #1 (1970b), 90.

Schlumberger Technologies, "1260 Impedance/Gain-Phase Analyzer," Operation Manual, Hampshire, England (1993).

Scully J.R., Hack H. P., Tipton D. G., "Effect of Exposure Time on the Polarization Behavior of Marine Alloys Under Flowing and Quiescent Conditions," *Corrosion*, 42 (1986), 462.

Sethi, V.K., Wright, I.G., *Proceedings of the First International Conference on Heat-Resistant Materials*, 439, Sept. (1991), Fortana, Wisconsin.

Silverman, D.C. "Rotating Cylinder Electrode for Velocity Sensitivity Testing," *Corrosion*, 40 (1984), 220-226.

Somerscales E.F.C., Sanatgar H., "Hydrodynamic Removal of Corrosion Products from a Surface," *British Corrosion Journal*, 27 (1991), 36.

Steele L.R., Geankoplis C. J., "Mass Transfer from a Solid Sphere to Water in Highly Turbulent Flow," *AIChE Journal*, 5 (1959), 178.

Stumm, W., Morgan, J.J., *Aquatic Chemistry: An Introduction Emphasizing Chemical Equilibria in Natural Waters*, 2nd ed., John Wiley and Sons, Inc. New York (1981).

Syrett, B.C. "Erosion Corrosion of Copper-Nickel Alloys in Sea Water and Other Aqueous Environments: A Literature Review," *Corrosion*, 32 #6 (1976) 242.

Syrett, B.C., MacDonald, D.D. "The Validity of Electrochemical Methods for Measuring Corrosion Rates of Copper-Nickel Alloys in Sea Water," *Corrosion*, **35** #11 (1979), 505.

Taylor, A.H. "The Corrosion Behavior of Cu and Naval Brass in 0.5M NaCl Solutions at Ambient Temperature," *Journal of the Electrochemical Society*, **118** #6 (1971), 854.

Tuthill, A.H. "Guidelines for the Use of Copper Alloys in Seawater," *Materials Performance*, (1987), 12.

Vahdat N., Newman J., "Corrosion of an Iron Rotating Disk," *Journal of the Electrochemical Society*, **120** (1973), 1682.

Wang, Y.Z., Beccaria, A.M., Poggi, G., " The Effect of Temperature on the Corrosion Behavior of a 70/30 Cu-Ni Commercial Alloy in Seawater," *Corrosion Science* **38** #8. (1994), 1277-1288.

Weast, R.C., ed., *CRC Handbook of Chemistry and Physics*, 65th ed., The Chemical Rubber Company Press Inc., Boca Raton, Florida (1984).

White, F.M., *Heat Transfer*, Addison-Wesley Publishing Company, Reading. Massachusetts (1984).

Wojcik, P.T., *Thermally Stimulated Impedance Spectroscopy*, Master's Thesis. University of Florida, Gainesville (1992).

Wojcik, P.T., Agarwal, P., Orazem, M.E., "A Method for Maintaining a Constant Potential Variation During Galvanostatic Regulation of Electrochemical Impedance Measurements," *Electrochimica Acta*, **41** (1996), 977-983.

Wojcik, P.T., Orazem, M.E., "Variable-Amplitude Galvanostatically-Modulated Impedance Spectroscopy as a Tool for Assessing Reactivity at the Corrosion Potential without Distorting the Temporal Evolution of the System." *Corrosion*, in press(1997a).

Wojcik, P.T., Orazem, M.E., "Experimental Study of the Erosion-Corrosion of Copper and Copper-Nickel Alloys Using a Submerged Impinging Jet," CORROSION/97. paper 97435 (1997b).

Wojcik, P.T., Orazem, M.E., "Variable Amplitude Galvanostatic (VAG) Modulated Impedance Spectroscopy as a Non-Invasive Tool for Assessing Reactivity at the Corrosion Potential," CORROSION/97, paper 97282 (1997c).

Wood, R.J.K, Fry, S.A., "Corrosion of Pure Copper in Flowing Seawater Under Cavitating and Noncavitating Flow Conditions," *Journal of Fluids Engineering*, **112** (1990), 218-224.

Wood, R.J.K., Hutton, S.P., Schiffrin, D.J., "Mass Transfer Effects of Non-Coavitating Seawater on the Corrosion of Cu and 70Cu-30Ni," *Corrosion Science,* **30** (1990), 1177.

BIOGRAPHICAL SKETCH

The author received the Bachelor of Science in Chemical Engineering degree from the Mississippi State University in August, 1986. He accepted employment with Milliken and Company as a production supervisor. Seeking a more technical position, he secured employment with Michelin Tire Corporation in May, 1988, as a process engineer until returning to graduate school at the University of Florida in August, 1989. The author received his Master of Science degree majoring in chemical engineering with an emphasis on solid state physics in May, 1992, and immediately began work on his Ph.D. He will receive his Ph.D. degree in Chemical Engineering from the University of Florida in August, 1997, and has secured employment as a senior engineer of technology with Merck and Company, Inc.
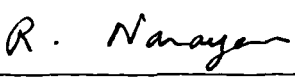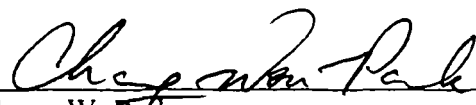
I certify that I have read this study and that in my opinion it conforms to acceptable standards of scholarly presentation and is fully adequate, in scope and quality, as a dissertation for the degree of Doctor of Philosophy.

Mark E. Orazem, Chair
Professor of Chemical Engineering

I certify that I have read this study and that in my opinion it conforms to acceptable standards of scholarly presentation and is fully adequate, in scope and quality, as a dissertation for the degree of Doctor of Philosophy.

Oscar D. Crisalle
Associate Professor of Chemical
Engineering

I certify that I have read this study and that in my opinion it conforms to acceptable standards of scholarly presentation and is fully adequate, in scope and quality, as a dissertation for the degree of Doctor of Philosophy.
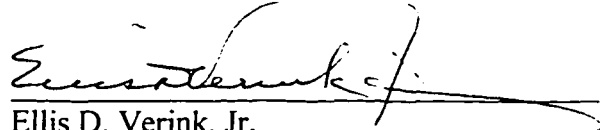
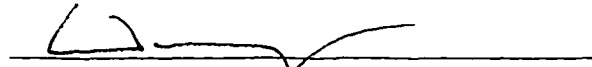Ranganatha Narayanan
Professor of Chemical Engineering

I certify that I have read this study and that in my opinion it conforms to acceptable standards of scholarly presentation and is fully adequate, in scope and quality, as a dissertation for the degree of Doctor of Philosophy.

Chang W. Park
Associate Professor of Chemical
Engineering

I certify that I have read this study and that in my opinion it conforms to acceptable standards of scholarly presentation and is fully adequate, in scope and quality, as a dissertation for the degree of Doctor of Philosophy.

Ellis D. Verink, Jr.
Distinguished Service Professor of Material
Science and Engineering

This dissertation was submitted to the Graduate Faculty of the College of Engineering and to the Graduate School and was accepted as partial fulfillment of the requirements for the degree of Doctor of Philosophy.

August, 1997

Winfred M. Phillips
Dean, College of Engineering

Karen A. Holbrook
Dean, Graduate School